UNIVERSITY OF OKLAHOMA

GRADUATE COLLEGE

DEVELOPMENT AND CHARACTERIZATION OF A HIGH-ENERGY IN-LINE PHASE CONTRAST TOMOSYNTHESIS PROTOTYPE

A DISSERTATION

SUBMITTED TO THE GRADUATE FACULTY

in partial fulfillment of the requirements for the

Degree of

DOCTOR OF PHILOSOPHY

By

DI WU
Norman, Oklahoma
2016

DEVELOPMENT AND CHARACTERIZATION OF A HIGH-ENERGY
IN-LINE PHASE CONTRAST TOMOSYNTHESIS PROTOTYPE

A DISSERTATION APPROVED FOR THE
SCHOOL OF ELECTRICAL AND COMPUTER ENGINEERING

BY

_____
Dr. Hong Liu, Chair

_____
Dr. Qi Cheng

_____
Dr. Bin Zheng

_____
Dr. Nathan Goodman

_____
Dr. Kai Yang

This dissertation is dedicated to my parents and grandparents. Words cannot express my gratitude for being blessed with their never-ending love, encouragement, and support.

Acknowledgements

Words cannot express my gratitude to Dr. Hong Liu providing me with an innovative and knowledge-rich environment and tremendous opportunities. My work would have been unachievable without his guidance and support.

Secondly, I would like to express my gratitude to the other members of my committee, Dr. Qi Cheng, Dr. Bin Zheng, Dr. Nathan Goodman and Dr. Kai Yang, for their great help, advices and encouragement.

I would also like to gratefully acknowledge Dr. Xizeng Wu and Dr. Aimin Yan in the University of Alabama at Birmingham for their collaborations, Dr. Yuhua Li providing me with valuable suggestions toward my research, Dr. Molly D. Wong for her endlessly helps on my research projects and English writings, Dr. Liangzhong Xiang for his valuable suggestions toward one of my research projects, and Jimmy Cannon in Engineering Practice Facility of the College of Engineering providing me a platform to demonstrate my hand-on designs of imaging phantoms and trained me how to manipulate the machines in the shop.

In addition, I am deeply grateful to the members of our research team, Zheng Li, Muhammad U. Ghani and Farid H. Omoumi, and our previous group member and visiting scholars, Dr. Hui Miao, Der-you Kao, Dr. Yuchen Qiu, Dr. Liqiang Ren, Dr. Xiaodong Chen, Dr. Jie Song, and Dr. Zhongxing Zhou, for their help and smooth teamwork.

Thanks for everything.

Table of Contents

List of Tables

List of Figures

Abstract

Phase sensitive 3D imaging techniques have been an emerging field in x-ray imaging for two decades. Among them, in-line phase contrast tomosynthesis has been investigated with great potential for translation into clinical applications in the near future, due to combining the advantages of configuration simplicity, structural noise elimination and potentially low radiation dose delivery. The high-energy in-line phase contrast tomosynthesis technique developed and presented in this dissertation initiates this translational procedure by optimizing the imaging conditions, performing phase retrieval, offering opportunities to further reduce radiation dose delivery, improving detectability and specificity with the employment of auxiliary phase contrast agents, and potentially performing quantitative imaging.

First, the high-energy in-line phase contrast tomosynthesis prototype was developed and characterized in this dissertation as the first of its kind following a number of engineering trade-off considerations. The quantitative results as well as the imaging results of tissue-simulating phantoms and biology-related phantoms demonstrate the extensive capability of this imaging prototype in improving tumor detectability. In addition, the optimization of the x-ray prime beam toward the PAD phase retrieval method proved the potential of high-energy imaging and predicated the solution toward imaging time reduction by employing photon counting based imaging techniques.

In the past several years, applications of microbubbles as a phase contrast agent have shown the capability for image quality improvement in quantitative imaging. In this

dissertation, a preliminary study of quantitative imaging of microbubbles using the in-line phase contrast projection mode imaging prototype, which is a system without tomosynthesis capability, provided a discussion on how the materials of the bubble shells and gas infills could impact the imaging capabilities and resulting image detectability. In addition, the results of the study provided a guideline for microbubble selections for in-line phase contrast mode imaging modalities. Based on this criterion discussed in the study, the albumin-shell microbubbles were selected as the phase contrast agent for the imaging prototype presented in this dissertation. The imaging results showed the feasibility of performing quantitative imaging by employing microbubbles as the auxiliary phase contrast agent. Clinical conditions were simulated by distributing microbubbles on the interface between two tissue-like phantom structures. The quantitative imaging results provided clinical motivation for translating phantom studies into more biology-related investigations providing radiation dose reductions in the future.

Chapter 1. Introduction

1.1 Significance

Breast cancer is one of the five most common cancers diagnosed in adults. In 2016, the estimated number of new breast cancer cases was 249,260, while the estimated number of deaths from breast cancer was 40,890. [1] Research has proved that early diagnosis and treatment of breast cancer are essential for improving the survival rate of patients.

Diagnostic mammography is a widely-used and standard method of performing early stage breast cancer detection and clinical screening using x-rays, but it can only acquire two-dimensional (2D) projections of 3D objects. [2-6] Therefore, mammography is not able to combat the challenge presented by overlapping structures from dense tissue superimposition. This inability potentially leads to missed cancers, as well as false-positive recalls and/or biopsies.

However, the development of a 3D x-ray breast imaging technique known as digital breast tomosynthesis in the past two decades has demonstrated the capability to image the human breast in three dimensions. Several clinical studies have indicated that utilizing breast tomosynthesis along with mammography improves the diagnostic sensitivity and therefore has the potential to reduce the recall rate. [5-7] Technically, digital breast tomosynthesis is an imaging method performing limited-angle 3D tomography using x-ray exposures, and can be considered a limited-angle CT scan. A limited number of conventional x-ray projections acquired from a narrow angular range are combined to reconstruct a 3D image by employing a reconstruction algorithm.

A clinical digital breast tomosynthesis system is designed to perform mammography-dose-level 3D imaging through the limited-angle scan. Thus, acquisition parameters including the coverage of the angle range, the number of angular projections and the dose distributions on each projection are regulated and constrained by the limits on the total exposure for all angular projections. This is due to the fact that increasing the number of projections may lower the exposure per projection and, thus, potentially make quantum noise more dominant, and enlarging the range of the scanning angle may result in the degradation of the spatial resolution by the high obliquity of the x-ray incidence angle. Several investigations on optimization tasks have indicated the following: 1) a small angular range results in better in-plane spatial resolution but worse resolution in the z-axis direction, and vice versa; 2) the detectability of large objects is primarily affected by the angular scan range, while the detectability of small objects such as micro calcifications, is limited not only by the quantum noise, but also the number of projections; 3) an increase in the number of projections should be accompanied with an increase in the angular range in order to minimize off-plane artifacts of high-contrast objects. [8-9] However, investigations for optimizing and improving digital breast tomosynthesis have not been completed, to the best of my knowledge.

To date, there have been two commercial digital breast tomosynthesis system approved by the U.S. Food and Drug Administration (FDA): Hologic Selenia Dimensions and GE SenoClaire. The Selenia Dimensions acquires angular projections by continuous gantry sweeping and utilizes a high-quantum-efficiency detector to obtain trade-offs between

shortening scan durations and imaging quality. In addition, it employs the FBP reconstruction algorithm, image binning technique and graphic processing unit (GPU) to perform high-speed 3D reconstruction. The GE SenoClaire implements step-by-step gantry motion and a specially-designed antiscattering grid to avoid focal spot blur and minimize scatter induced by tissues, and uses a custom-developed iterative algorithm to minimize the off-plane blur occurring in reconstructed images. These two commercial digital breast tomosynthesis machines denote the progress that has been made to date in clinical digital breast tomosynthesis systems. However, concerns still remain that digital breast tomosynthesis may result in a higher radiation dose delivered to patients as compared to mammography, and that it has limited capability in the detection of small micro calcifications. [8-9]

Since the angular projections acquired in a digital breast tomosynthesis are the same x-ray projections employed in conventional mammography, the imaging contrast of this type of imaging modality relies solely on the small attenuation differences between normal tissues and tumors. However, x-rays passing through an object also undergo phase shifts during their propagation. Several studies investigating x-ray phase contrast imaging techniques have demonstrated that combining the attenuation and phase shift significantly improves the imaging quality. [10-13] Among several types of phase contrast modalities, the in-line phase contrast technique utilizes a similar system configuration as conventional mammography, with an added distance between the object and the detector to acquire x-ray phase gradients generated by the variation of fraction indices within the object, as well as a micro-focus x-ray source to guarantee relatively high spatial

correlation. [13-15] Combining the in-line phase contrast mechanism with the tomosynthesis technique, the angular projection presents not only attenuation, but also phase shift information. Based on this concept, 3D tomosynthesis with in-line phase contrast imaging method has shown high potential for clinical translation, not only through demonstrating a potential improvement in imaging quality by additional edge enhancement, but also due to the simple transformation of a conventional tomosynthesis system into an in-line phase contrast tomosynthesis system. [16]

However, the long distance between the object and the detector required by the in-line phase contrast technique results in fewer x-ray photons received by the detector, as compared to the contact mode detection used in conventional tomosynthesis, under the same conditions of exposure parameters, radiation dose delivery and the capability of detectors. Thus, an in-line phase contrast tomosynthesis system can hardly provide similar imaging ability as a conventional digital breast tomosynthesis system, due to the massive loss of attenuation contrast. In aiming to solve this problem, high-energy x-ray, which is already employed in chest radiography, can be employed to compensate for the loss of x-ray photons during a long-distance propagation, thus preserving most of the attenuation contrast. Due to the high penetrability and low absorption of high-energy x-ray photons, the radiation dose received by patients can also be potentially reduced. In addition, since the phase contrast effect decreases much more slowly than attenuation contrast as the x-ray energy increases, the phase retrieval method, which reveals how the phase shifts are encoded in the image intensity variations, can be employed for high-energy in-line phase contrast imaging to preserve the bulk of the phase contrast.

Within the past decade, in order to further improve the imaging quality and maximize the advantage of the phase contrast mechanism, either by itself or combined with 3D imaging techniques, concepts of tissue engineering have been proposed to introduce the application of microbubbles into phase-related imaging techniques. Widely used as an ultrasonic contrast agent, microbubbles have been demonstrated to adhere and accrete to the wall of blood vessels and membranes to construct a structure with high spatial frequencies around tissue and/or along the interfaces among tissues. Microbubbles can be considered as a population of x-ray lens scattering photons providing a sequence of multi refractions. Thus, microbubbles can be employed to provide additional phase shift information around tissues and/or along the interfaces between tissues, as the x-ray phase shift will be enhanced where the microbubbles congregate. Preliminary investigations indicating that microbubbles can be used as x-ray phase contrast agent have been performed using analyzer-based [22] and propagation-based [23] synchrotron x-ray phase contrast, as well as the synchrotron free-space propagation phase contrast method, [24-25] and the Talbot-Lau interferometry phase contrast method. [26-27] A recent study done by Millard, *et al*. indicated that microbubble contrast agents have high potential to perform dynamic imaging with analyzer-based synchrotron x-ray phase contrast. [28] 3D computed tomography imaging of microbubbles has also been demonstrated recently through a differential phase contrast system utilizing object rotation. [29] In these studies, microbubbles were injected or contained in tissues, phantoms or vials for demonstrations, and the results showed that employing microbubbles enhanced the image contrast in the phase shift images of the areas in a tissue or phantom with tiny structures. However, to

the best of my knowledge, the radiation dose used for imaging microbubble distributions by phase contrast related 2D/3D methods has not been investigated, and the imaging quality has not been compared with conventional 2D/3D methods. Thus, the significance and the advantage of employing microbubbles in x-ray phase related imaging method has yet to be investigated.

1.2 Objectives

The goal of this dissertation is to present a comprehensive investigation of a digital tomosynthesis imaging system combined with the high-energy in-line phase contrast technique. The prototype of the high-energy in-line phase contrast tomosynthesis system detailed in this dissertation has been developed to demonstrate its clinical potential not only to improve the imaging quality in cancer detection, but also to reduce the radiation dose delivered to patients. In addition to the characterization work for the prototype itself, the advantages of its applications in imaging microbubble distribution in objects will be discussed in detail in this dissertation research, and the radiation dose will be regulated.

1.3 Organization of Dissertation

The organization of this dissertation is as follows. Chapter 2 details the research background, including the principles of the tomosynthesis and in-line phase contrast techniques. Chapter 3 presents the prototype of the high-energy in-line phase contrast tomosynthesis developed in the dissertation study, and Chapter 4 characterizes the newly developed high-energy in-line phase contrast tomosynthesis prototype. Chapter 5 provides an optimization approach toward solving one imperfection discussed in Chapter

4. Chapter 6 elucidates the feasibility of employing microbubbles as an x-ray phase contrast agent with a projection mode imaging system and provides a criterion in microbubble shell material selection. Chapter 7 preliminarily demonstrates the capability of quantitative imaging by using microbubbles as x-ray phase contrast agent for high-energy in-line phase contrast tomosynthesis. Chapter 8 preliminarily demonstrates the edge enhancement provided by distributing microbubbles on the interface between two tissue-simulating structures when imaged by high-energy in-line phase contrast tomosynthesis under a unified radiation dose delivery. Finally, a research summary and a discussion of future research direction are presented in Chapter 9.

Chapter 2. Research Background

2.1 Digital Tomosynthesis

Since the first tomosynthesis image of the breast was acquired by Niklason in 1997, [30] it has become an important 3D breast imaging method to overcome tissue superposition issues, which cannot be avoided in conventional 2D mammography. In this section, the digital breast tomosynthesis system will be discussed in detail, from the different system configurations and image acquisition techniques to the image reconstruction methods.

2.1.1. System Configurations

General Configuration

Currently, a general digital breast tomosynthesis system is similar to a digital mammography system: the center of the x-ray source, object and detector are precisely aligned, and the object is exposed on a support stage near the detector. A simple device that can transform a mammography system into a tomosynthesis system involves a rotation mechanism. In a commercial digital breast tomosynthesis system, this rotation mechanism is always an arm that can rotate the x-ray tube around a pivot point close to the detector plane. However, in laboratory prototypes and the research field, the rotation mechanism is sometimes substituted with a rotating stage moving the object, in an effort to simplify phantom and/or tissue studies. Based on different optimization strategies in image acquisition, researchers and commercial system manufacturers may implement modifications in digital breast tomosynthesis configurations as compared to digital mammography systems.

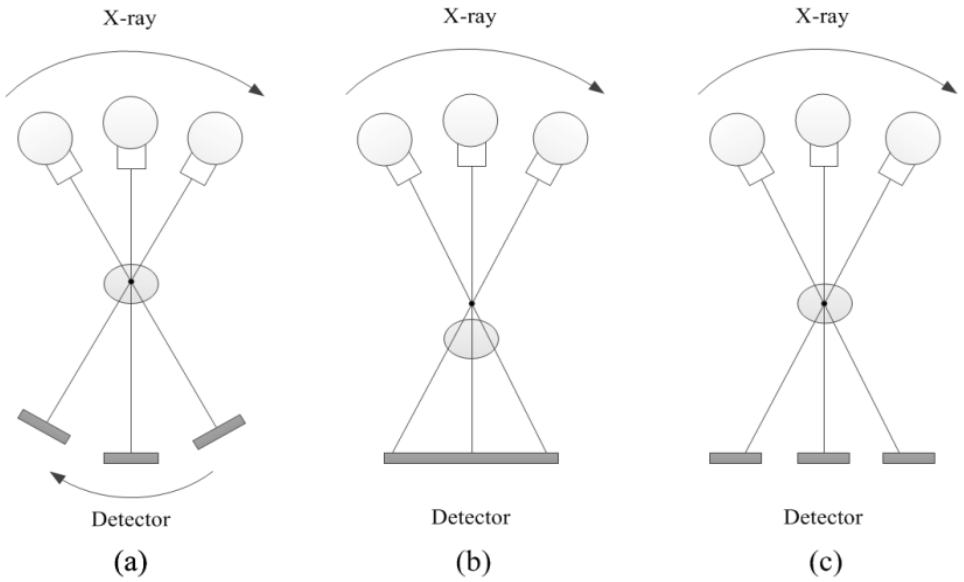

Figure 1: Basic tomosynthesis geometries: (a) isocentric mode, in which both x-ray source and detector rotate around a fixed pivot point synchronously; (b) partial isocentric mode, where the x-ray source rotates around a pivot point near or on the center of the object under detection and the detector is stationary; and (c) parallel path mode, in which the detector moves in one plane and the x-ray source rotates about a pivotal point.

There are three widely-used basic system geometries of the digital breast tomosynthesis image acquisitions, all of which are shown in Figure 1: (a) isocentric mode, in which both x-ray source and detector rotate around a fixed pivot point synchronously; (b) partial isocentric mode, where the x-ray source rotates around a pivot point near or on the center of the object under detection, and the detector is stationary; and (c) parallel path mode, in which the detector moves in one plane and the x-ray source rotates about a pivotal point. In both partial isocentric mode and parallel path mode gantry motion, the incident angle of the x-ray exposures onto the detector vary during the arc motion of the x-ray tube. The oblique incidence of the x-ray exposure induces a negative impact on the point spread function of the imaging system and, thus, degrades the modulation transfer function. Also, the oblique incidence of the x-ray may potentially result in decreases in the detective quantitative efficiency and the small signal detectability of the system. [8-9]

The detector is an important part of an imaging system. Contrary to how it is used in a mammography system, a detector employed in a tomosynthesis system must perform the data read-out more quickly, produce minimized ghosting, which may result in artifacts in the reconstructed images, and provide minimal detective quantum efficiency reduction at relatively low exposure levels, all of which preserve the imaging quality under mammography radiation dose delivery. [8] Several studies employing amorphous selenium (a-Se) based direct detectors determined that this type of detector meets the requirements of minimal reduction in the detective quantum efficiency at low exposures, as it is able to minimize the domination of electronic noise. Furthermore, a modified thin-film-transistor (TFT)-type a-Se based direct detector is used in the Hologic Selenia Dimensions system, and was reported to reduce the data read-out time to sub-second level and achieve a total acquisition time of several seconds. [31-32] However, the expense in obtaining such a short image acquisition period is the loss of system spatial resolution, which results from the application of the continuous gantry motion and the pixel binning in the detection process. The most recently FDA-approved GE SenoClaire tomosynthesis system employs step-and-shoot tube motion mode without binning, which facilitates the detection of microcalcifications, and implements an anti-scattering process to reduce scattered radiation while preserving dose and imaging performance. [33]

Instead of a-Se based direct detectors, CCD-based and CMOS-based indirect flat-panel detectors have been widely used in laboratory digital breast tomosynthesis prototypes for system characterizations and imaging studies using small animals, tissues and phantoms.

[34-35] Indirect flat-panel detectors employ a scintillator layer to convert x-ray energy to optical photons that can be captured by the CCD or CMOS sensor array. The thickness of the scintillator may cause additional scattering and, therefore, decrease the imaging spatial resolution, but CCD-based and CMOS-based flat-panel detectors are both able to produce relatively low electronic noise. Also, when the application of CCD-based and CMOS-based flat-panel detectors in a digital tomosynthesis system was first investigated, the major disadvantage of both types of detector was the relatively small dimensions, which prevented employing full field digital mammography on a large area. Fortunately, with recent advancements in large-scale integrated circuit technology, tiled wafer-scale CMOS detectors with dimensions up to 29 cm × 23 cm were developed in 2012, and applying this achievement to CMOS-based flat-panel detectors allows them to extend their applications into the detection of larger areas than previously possible. [34-35]

Along with detection capabilities, the image acquisition parameters and the acquisition method of the angular projections are also crucial in affecting the imaging qualities of the system. As a digital breast tomosynthesis system was proposed to perform mammography-dose-level 3D imaging through limited-angle scanning, the acquisition parameters including the coverage of the angle range, the number of angular projections and the dose distributions on each projection are regulated and constrained by the limits on the total exposure for all angular projections. This is because increasing the number of projections may lower the exposure per projection and, thus, potentially make quantum noise more dominant, and enlarging the range of the scanning angle degrades the spatial resolution due to the high obliquity of the x-ray incidence angle. Several investigations

on optimization tasks have indicated the following: a small angular range resulted in better in-plane spatial resolution but worse resolution in the z-axis direction, and vice versa; the detectability of large objects was primarily affected by the scan angle range, while the detectability of small objects such as microcalcifications was limited by not only the quantum noise, but also the number of projections; an increase in the number of projections should be accompanied with an increase in the angular range in order to minimize off-plane artifacts of high-contrast objects. [8-9] A study presented by Van de Sompel et al. in 2011 found that, under a constant dose delivery and a certain number of projection views, imaging quality can be improved by widening the angular range until a maximum is reached. Unfortunately, the investigation for the optimization of angular range as well as the number of angular projections has not been concluded. [8-9]

In addition to the most widely-used basic system designs detailed in this section, there are a number of additional tomosynthesis configurations developed in an attempt to solve or optimize current issues existing in conventional configurations, or to extend the scope of this technique, such as stationary tomosynthesis systems, photon-counting detection tomosynthesis, complicated scanning strategies, etc.

Stationary-Source Based Tomosynthesis System

In a stationary tomosynthesis system, the conventional x-ray tube and the rotating gantry can be replaced by a distributed field emission x-ray tube array, such as a carbon nanotube (CNT) array, which is known as a stationary x-ray source. [36-38] This type of x-ray source arrangement is designed to avoid focal spot blur resulting from the x-ray tube

movement and potentially reduce the time of projection acquisitions. A number of recent studies presented the stationary imaging acquisition gantry as a replacement for the rotation gantry with a conventional x-ray tube. [8, 39]

The study in Ref. [39] demonstrated this substitution through the replacement on a commercial digital tomosynthesis machine (Selenia Dimensions, Hologic, Inc., MA) with an x-ray array consisting of 31 carbon nanotubes having a length of 370 mm, which was able to cover a 30° scanning range equivalently. This study demonstrated an improvement in the modulation transfer function of the system and an increase in microcalcification sharpness as compared to the rotation-gantry system when imaging the 0.54, 0.40 and 0.32 mm speck groups of an ACR mammography phantom under 28 kVp and a total exposure of 100 mAs (6.67 mAs per projection). However, several issues for the optimization of this system still need to be addressed, including the image read-out time of the detector and the tube current. [39] As an agreement of this research, Andrew et al developed a stationary digital breast tomosynthesis (s-DBT) system using a CNT-based X-ray source array, and compared the imaging visibility of microcalcifications in human tissue with the Hologic Selenia Dimensions digital breast tomosynthesis system. Through comparing estimations of the artifact spread function (ASF) for the reconstructed images, the results indicated that the visibility and sharpness of the microcalcifications were both improved by the s-DBT system. [40] The results of an additional study presented by Andrew et al in 2013 using the same s-DBT system indicated that the number of views has little impact on imaging quality, and that employing less views for the same angular

coverage, a large angular span and uniform mAs distribution over all projections may be optimal for the imaging configuration. [41]

In a recent feasibility study of a stationary tomosynthesis imaging system developed by Shan at el. in 2015, 75 linearly distributed carbon nanotubes were employed to construct an x-ray source array providing an output of 50 to 150 kVp. In addition, a flat panel detector was used for image acquisition, and a translation mechanism extends the angular span coverage up to 34°. The scanning strategy used in this study was 85 projections with 0.4° angular interval between projections, thus making it comparable to a commercial tomosynthesis system. Although the system was developed for chest imaging, it was designed for use in lung vessel and nodule screening, which are soft tissues. The system therefore inspired the development of stationary digital breast tomosynthesis systems. In the system characterization, the modulation transfer function in both the vertical and horizontal directions remained the same for various angular coverages, and the vertical direction exhibited improved modulation transfer function performance due to the anisotropic dimensions of spot size in corresponding directions. Artifact spread functions were also investigated, and indicated that improvements occurred when the angular coverage was increased. In the anthropomorphic phantom study, 62.3 μGy incident air kerma per projection at 0.6 mAs and 80 kVp was measured at the patient entrance plane, which was 95 cm far from the x-ray source. Assuming that the patient entrance plane is extended to 155 cm, the incident air kerma will be reduced to 18.6 μGy, which is still considered slightly higher than the mean air kerma per projection in tomosynthesis techniques. [42] In conclusion, their study demonstrated the feasibility of a stationary

digital chest tomosynthesis system with optimization needed in several aspects, such as the shape and size of focal spots, imaging acquisitions, dose delivery to the patients, etc., and it also provided a solution to enlarge the covering area for digital tomosynthesis.

Photon-counting Based Tomosynthesis System

Another non-traditional tomosynthesis machine was manufactured by modifying the Sectra MicroDose Mammography system (now Philips Healthcare). A multi-slit photon counting detector, consisting of 21 linear photon-counting sensors, and a collimated x-ray fan beam scanned an 11° angular range across the object with an isocenter below the detector, which is one of the differences compared to the traditional digital breast tomosynthesis. [43] The advantages of using a photon-counting detector are as follows: low scattering signals, potentially no electronic noise based on proper configuration of photon-counting thresholds, potentially high quantum efficiency, and the ability of photon energy discrimination performing the acquisition of both a high-energy image and a low-energy image simultaneously, thus obtaining a dual-energy subtraction image which improves the imaging specificity. [43, 44]

In 2012, European researchers conducted a comparison observer study between digital breast tomosynthesis imaging and full-field digital mammography. The tomosynthesis imaging system employed was the same photon-counting tomosynthesis system described above, while the full field mammography was performed with a MicroDose D40 system (now Philips Healthcare) and Senograph DS or Senograph Essential system (GE Medical Syetem). The radiation dose delivered to patients by the photon-counting

tomosynthesis imaging ranged from 0.28 to 1.42 mGy, while it was 0.2 to 2.4 in the 2D mammography cases, which denoted a potentially lower radiation dose to patients can be achieved by photon-counting tomosynthesis. The reader study results concluded that two-view tomosynthesis using the photon-counting prototype performed better than 2D mammography. [45]

As photon-counting detection attracts more and more attention in the digital tomosynthesis technique, photon-counting detectors were characterized to optimize application conditions and facilitate their feasible use for tomosynthesis in the future. Siewerdsen et al in 2014 conducted a study to provide understanding on complicated dependencies and optimizations in photon-counting detector performance, and the potential pros and cons in comparison with widely used flat panel detectors and other energy integrated detectors. [46]

Other Tomosynthesis Systems

Compared to the conventional x-ray tube motion of the previously-discussed tomosynthesis systems, researchers proposed that the motion of x-ray source can be operated not only along a one-plane arc trail, but also can be performed in a three-dimension range. Stevens et al suggested a circular tomosynthesis by operating the motions of both x-ray tube and detector in two circles parallel to each other. Xia et al. and Zhang *et al* proposed moving the x-ray tube along two arc trails perpendicular to each other on a spherical surface. And Zhang *et al* also developed a zigzag arc trail of x-ray tube movement on a spherical surface above the object and the detector. These

complicated designs of tomosynthesis modalities have been tested and demonstrated by both computer simulations and digital phantom studies, and the results were encouraging, but the dose delivery was of less concern in their studies. In addition, their complicated geometries render it difficult to predict clinical use and operations in order to propose this type of system in the near future. [8]

2.1.2 Reconstruction Algorithms

In digital tomosynthesis techniques, the resultant images are obtained from a set of angular projections by reconstruction. There are two widely-used reconstruction algorithm families serving the functions in this technique, the filtered backprojection algorithm (FBP) and the iterative algorithm.

Filtered Backprojection

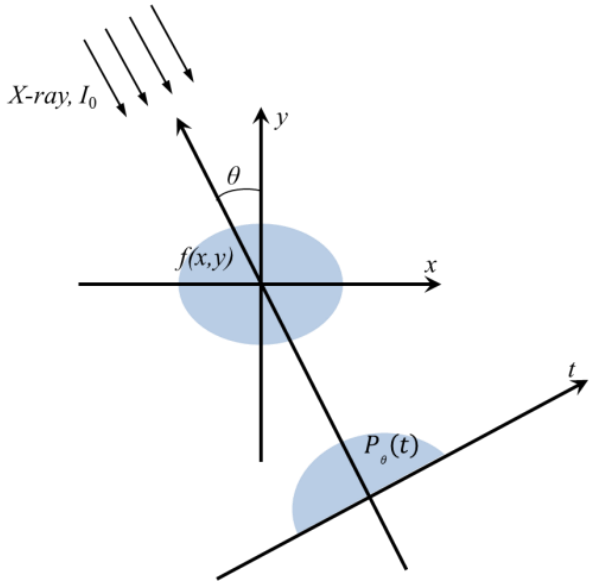

Figure 2: The object distribution f(x, y) is mapped to the set of line integrals.

The filtered backprojection (FBP) algorithm has been an image reconstruction method widely used in digital tomosynthesis techniques. FBP arises from Fourier-transform-based backprojection techniques for conventional computed tomography (CT) imaging, in which Radon transform maps 2D objects, $f(x, y)$, into a set of linear integrals denoted by (θ, t), where t is defined by $t = \mathbf{r}\cdot\boldsymbol{\theta}$, $\mathbf{r} = (x, y) \in \mathbf{R}^2$ and $\boldsymbol{\theta} = (\sin\theta, \cos\theta) \in \mathbf{R}^2$. The relationship between $f(x, y)$ and the linear integral defined as Radon transform $P_\theta(t)$ would therefore be as follows:

$$P_\theta(t) = \int_{(\theta,t)} f(x, y)\, dx\, dy. \tag{1}$$

Using the delta function, Eq. (1) can be rewritten as:

$$P_\theta(t) = \iint_{-\infty}^{+\infty} f(x, y)\delta(x\cos\theta + y\sin\theta - t)\, dx\, dy. \tag{2}$$

Then the Fourier transform of a projection at an angle, $P_\theta(t)$, can be written as follows:

$$S_\theta(\omega) = \iint_{-\infty}^{+\infty} P_\theta(t)\, e^{-j2\pi\omega t} dt, \tag{3}$$

while the 2D Fourier transform of the object $f(x, y)$ is:

$$F(u, v) = \iint_{-\infty}^{+\infty} f(x, y)\, e^{-j2\pi(ux+vy)} dx dy. \tag{4}$$

Based on the Fourier slice or Central slice theorem, a 1D Fourier transform of a projection at angle θ equals a section of the 2D Fourier transform of the object $f(x, y)$, and if we take the 1D Fourier transform of projections from 0° to 180° continuously, then the set of those 1D Fourier transforms will be exactly the 2D Fourier transform of the object. By constructing a rotated version of the (x, y) coordinate system expressed by:

$$\begin{bmatrix} t \\ s \end{bmatrix} = \begin{bmatrix} \cos\theta & \sin\theta \\ -\sin\theta & \cos\theta \end{bmatrix} \begin{bmatrix} x \\ y \end{bmatrix}, \tag{5}$$

a projection along lines of constant, t, is written as:

$$P_\theta(t) = \int_{-\infty}^{+\infty} f(t, s)\, ds. \tag{6}$$

Then we have:

$$S_\theta(\omega) = \iint_{-\infty}^{+\infty} [f(t,s)\, ds]\, e^{-j2\pi\omega t} dt. \tag{7}$$

Transferring (7) back into the (x,y) coordinate system by employing relationship (5) again, we have:

$$S_\theta(\omega) = \iint_{-\infty}^{+\infty} f(x,y)\, e^{-j2\pi\omega(x\cos\theta + y\sin\theta)} dxdy. \tag{8}$$

By defining $u_\theta = \omega\cos\theta$ and $v_\theta = \omega\sin\theta$,

$$S_\theta(\omega) = F(\omega,\theta) = F(u_\theta, v_\theta). \tag{9}$$

This means that the value of $F(u,v)$ for radial orientations can be determined by taking angular line projections from θ_1, θ_2,…, θ_k, and performing the Fourier transform. Therefore, the original object $f(x, y)$ can be recovered by inverse Fourier transform:

$$f(x,y) = \mathcal{F}^{-1}[F(u,v)]. \tag{10}$$

However, tomosynthesis is limited-angle tomography, where the data are acquired only from a limited angular span with respect to the object. In this case, the x-ray tube moves along a circular arc or on a linear trajectory, as detailed in previous sections. Because of the limited angle range from which the angular projections are acquired, the exact reconstruction of the object can hardly be performed by Equation (10), and the data are missing with the impact of the object this incompletely sampled. Artifacts, as a consequence, will be unavoidable.

The artifacts, the impact of incomplete sampling on imaging qualities, can be seen from the point spread function or the response function of one point in the space. Considering

the most general image acquisition scheme shown in Figure 3, the point spread function of the backprojection is given by: [47]

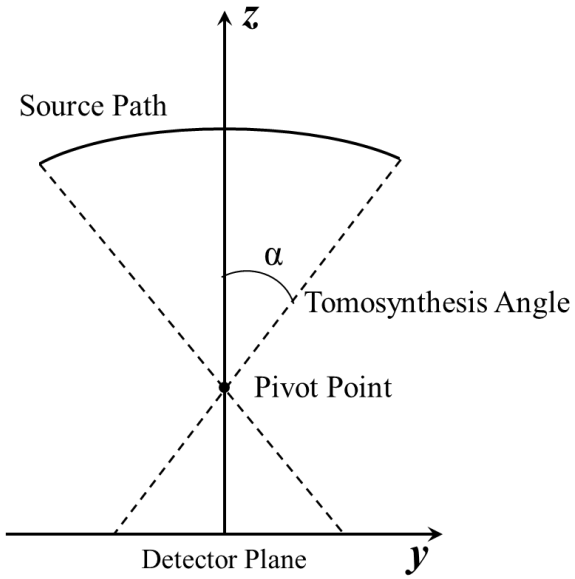

Figure 3: Scan geometry of partial isocentric mode tomosynthesis.

$$h_{\mathrm{p}}(\boldsymbol{r}) = \text{const.} \int_C \int_{-\infty}^{+\infty} \delta(\boldsymbol{r} - s\boldsymbol{e}_t)\mathrm{d}s\mathrm{d}t \ , \tag{11}$$

where the integral over *s* represents one projection in the direction of the unit vector $\boldsymbol{e}_t$, and *C* denotes the source path as a function of parameter *t* ($t \in R$). Therefore, the integral over the source path, *C*, is the backprojection of all projection rays passing through the point, $\boldsymbol{r}$. When operating the acquisition sampling with equiangular interval, Equation (11) can be rewritten in cylindrical coordinates (x, r, φ) as:

$$h_{\mathrm{P}}(\boldsymbol{r}) = \frac{1}{2\alpha} \int_C \int_{-\infty}^{+\infty} \delta\big(\boldsymbol{r} - s\boldsymbol{e}_\varphi\big)\mathrm{d}s\mathrm{d}\varphi \tag{12}$$

and, then, further rewritten in Cartesian coordinates (x, y, z) yielding $r^2 = y^2 + z^2$ as:

$$h_{\mathrm{P}}(x, y, z) = \begin{cases} \frac{1}{2\alpha\sqrt{y^2+z^2}}\delta(x) & for\ \frac{y}{z} < \tan\alpha \\ 0 & otherwise. \end{cases} \tag{13}$$

Thus, the point spread function illustrates that the imaging data information is distributed across all slices, and the image of a point becomes linear in neighboring slices with decreasing intensity for increasing distance. Therefore, a backprojected point on a certain slice has the potential to impact points located on other slices.

In addition, when observing the Fourier transform of the backprojection point spread function:

$$H_{\mathrm{P}}(\boldsymbol{\omega}) = \frac{1}{2\alpha\sqrt{\omega_y^2+\omega_z^2}} \tag{14}$$

and considering an approximation of $\omega_y \ll \omega_z$, there is a low pass filter along the scanning direction leading to the blurring of the simple backprojection reconstruction.

Then, starting from the system equation of a reconstruction procedure as follows:

$$G(\omega) = H(\omega) \cdot F(\omega), \tag{15}$$

where $F(\omega)$ denotes the Fourier transform of the object and $H(\omega)$ is the system modulation transfer function. Therefore, $G(\omega)$ is the Fourier transform of the reconstructed image, and we assume the modulation transfer function can be split into a filtering function and a backprojection transfer function $H_{\mathrm{P}}(\omega)$:

$$H(\omega) = H_{\mathrm{FILTER}}(\omega) \cdot H_{\mathrm{P}}(\omega). \tag{16}$$

The filtering function inverts the backprojection transfer function, but the inversion cannot be solved exactly. Thus, designs of filter functions provide the flexibility to tune characteristics of the reconstructed images and to minimize artifacts. [48]

In the past decade, many studies have sought to optimize the FBP algorithm for tomosynthesis imaging, as well as minimize the impacts resulting from incomplete sampling. Mertelmeier et al. in 2006 presented a general theory of the FBP algorithm

using in digital tomosynthesis under the arc tube motion by applying ramp filters, apodization filters, and/or slice thickness filters to decrease the impact of the insufficient angular range used in tomosynthesis to control the out-of-plane artifacts, and consequently improve the imaging quality and detective quantum efficiency. [8, 49]

In the following years, Zhou et al. in 2007 modified the standard ramp filter for FBP algorithm and compared the simulation results with the iterative algotithm, which will be introduced later; Orman et al. 2008 employed an additional filter to avoid the zeroing effects of the ramp filter for low frequencies, but unfortunately also introduced undesired flatness to images; and Wang et al. 2010 presented a small improvement of mass detectability on the in-plane slice. However, these attempts to decrease artifacts and improve tomosynthesis imaging quality through modifying filters applied in the FBP algorithms suffered many drawbacks and defects. Therefore, tomosynthesis imaging still faces the challenge of technical trade-offs in medical imaging engineering. [8, 49]

Iterative Reconstruction Methods

Due to the simplicity and speed of the backprojection algorithm, digital tomosynthesis is almost universally practiced through its techniques. However, there is a family of iterative reconstruction techniques performing the reconstruction of a 3D object from 2D projections.

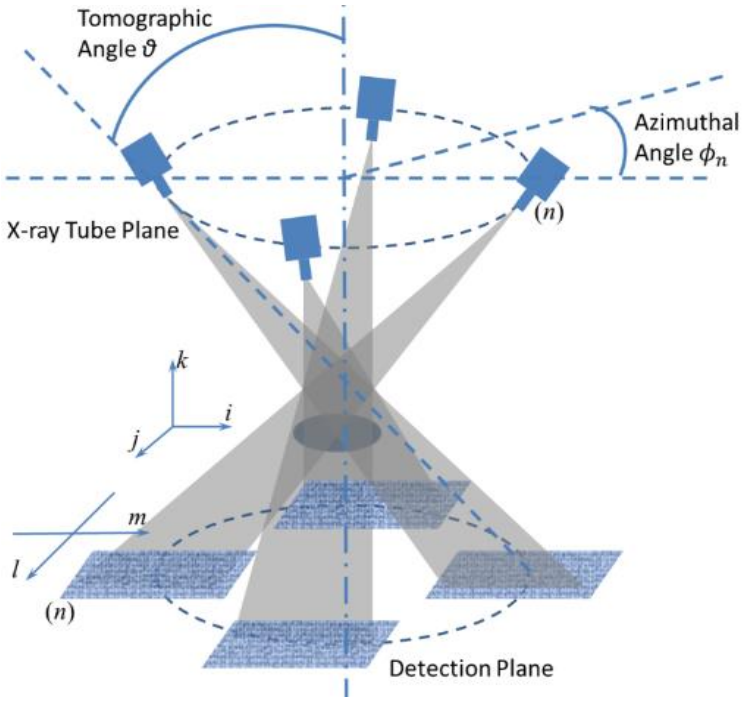

Figure 4: Double-circle motion prototype of tomosynthesis to illustrate the principle of the iterative reconstruction method.

The basic concept of the iterative algorithm was based on the approximation in an attempt to solve the series of simultaneous equations linking each voxel element to projected pixel values in a limited number of projections. When considering the standard monochromatic approximate model for transmitted x-ray intensity, neglecting x-ray scatter, the general relationship between the 3D object and the 2D projections can be described as

$$P(l,m,n) = \sum_i \sum_j \sum_k W(i,j,k,l,m,n) D(i,j,k), \quad (17)$$

where *P* represents the projection line integral through all voxels in the object along a given x-ray path, *D* denotes the density of structures, or attenuation coefficient, in the 3D object, and *W* is a weighing factor corresponding to the volume of intersection of a given exposure and voxel. The acquisition of 2D angular projections is shown in Figure 4. As *W* is difficult to be exactly computed, an approximation is made as follows:

$$W(i,j,k,l,m,n) = \delta(l, i - k\tan\theta\cos\phi_n)\delta(m, j - k\tan\theta\sin\phi_n). \quad (18)$$

Then we have

$$P(l,m,n) = \sum_{k=-K}^{K} D(l + k\tan\theta\cos\phi_n\,, m + k\tan\theta\sin\phi_n\,, k), \qquad (19)$$

where θ represents the tomographic angle, φ_n is the azimuthal angle of the n^{th} projection, and the number of projections is 2K + 1. It is important to note that this model depicted an x-ray tube scanning motion in 3D. In current applications for tomosynthesis reconstructions, modifications are needed on (19). For projections corresponding to linear tomography, the azimuthal angle φ_n=0, and the tomographic angles θ are equally spaced between θ_{min} and θ_{max}.

Because the value of $D(i,j,k)$ is unknown without a priori, we assume the $D(i,j,k)$ exists such that the raysum along the x-ray path can be calculated as:

$$R^{q,n}(l,m,n) = \sum_{k=-K}^{K} D(l + k\tan\theta\cos\phi_n\,, m + k\tan\theta\sin\phi_n\,, k), \qquad (20)$$

where q and n refer to the qth iteration and the nth projection, respectively. The error in each iteration can be estimated and given by:

$$E^{q,n}(l,m,n) = P(l,m,n) - R^{q,n}(l,m,n). \qquad (21)$$

The successively iterated voxel density, $D^{q,n}(i,j,k) \longrightarrow D^{q+1,n}(i,j,k)$, can be described as follows:

$$D^{q+1,n}(i,j,k) = D^{q,n}(i,j,k) + \frac{1}{2K+1} E^{q,n}\begin{pmatrix} i - k\tan\theta\cos\phi_n\,, \\ j - k\tan\theta\sin\phi_n\,, n \end{pmatrix}. \qquad (22)$$

This equation demonstrates that, after an initial estimation of $D^{q,n}(i,j,k)$ is made, the errors in Equation (21) are calculated and backprojected along each x-ray path to $D^{q,n}(i,j,k)$. Then the same process will be performed onto the next projection until all the projections are included and their corresponding errors are backprojected. Multiple

such iterations of the iterative processing may be performed in one reconstruction task until the error terms drop below a specified threshold.

Based on this simple concept, several types of iterative algorithms were developed by modifying and optimizing the strategies in implements of error criteria, such as simultaneous iterative reconstruction technique (SIRT), gradient descent (GD) on the Euclidean data-error distance, the maximum-likelihood expectation-maximization (MLEM) for a Poisson noise model, and the algebraic reconstruction technique (ART).

Ruttimann et al. in 1984 suggested constrained iterative restoration. First, this method estimated tomographic blur resulting from the convolution of the weighted fraction of conventional reconstructed slices with their blurring functions. Next, the method subtracted the blur from the original reconstructions. The advantage of this technique is no low-frequency noise amplification, which is inherent in the solution of direct inversion. But a relatively long computation period or a super computer is required in processing this reconstruction. [8, 49]

In 2005, Chen et al. proposed another algebraic reconstruction method for digital tomosynthesis: matrix inversion tomosynthesis (MITS). The results indicated this method successfully removed out-of-plane artifacts and handled high frequency information, but performed poorly with mass details. In the same study, Chen et al. applied a hybrid reconstruction algorithm incorporating acceptable low frequency response of filtered backprojection as well as high frequency response of MITS. The reconstruction results

showed that the image of overall breast tissue was enhanced, the imaging quality of high-spatial-frequency structure was improved and the loss of mass area details was suppressed. [8, 49]

In 2006, Zhang et al. demonstrated the simultaneous algebraic reconstruction technique (SART) method for digital tomosynthesys imaging and performed a phantom comparison to the standard backprojection algorithm. The results showed that the standard backprojection algorithm performed the same or better than SART in one of the homogeneous phantoms, but resultant images of the phantoms with tissue-equivalent structures reconstructed with the SART algorithm were better. In 2012, Lu et al. demonstrated the improvement of microcalcification visibility without affecting mass details through wavelet decomposition for multiscale regularization of noise in the SART algorithm. [8, 49]

Ludwig et al. in 2008 proposed the combination of an iterative reconstruction method, the simultaneous iterative reconstruction technique (SIRT), with filtered backprojection. The authors estimated the impulse response of SIRT reconstruction in digital tomosynthesis and applied it in filtering the frequency domain. This method could be combined with the other preprocess filters to the acquired projections before reconstruction. The advantage of this method is its lower dependence on the number of angular projections acquired. Compared with the method using filtered backprojection reconstruction only, the application of the SIRT reduces the sharpness of the images. [8, 49]

In the recently FDA approved digital breast tomosynthesis system, GE SenoClaire, iterative algorithm was implemented to perform reconstruction. As indicated in the product brochure, a calcification artifact correction iterative reconstruction algorithm, $ASiR^{DBT}$ (adaptive statistical iterative reconstruction), is able to deliver off-plane imaging improvements in terms of both in-plane and out-of-plane artifacts versus the traditional FBP algorithm. [8] Unfortunately, based on my scope of knowledge, this commercial tomosynthesis system along with its reconstruction algorithm has not been characterized.

Other Reconstruction Strategies

There were two conceptually different reconstruction algorithms proposed in 2010. In contrast with the traditional cubic voxels in most reconstruction algorithms, Wu et al. proposed an algorithm producing spherically symmetric voxels, blob voxels. This blob-voxel reconstruction resulted in a less noisy but more blurry image compared to the cubic voxels. Meanwhile, Chung et al. suggested a spectral reconstruction algorithm. This method utilizes the polyenergetic nature of x-ray beams entering the object. They developed a mathematical framework based on a polyenergetic model and statistically based iterative methods for digital breast tomosynthesis reconstruction. The simulated results illustrated the success in suppressing beam hardening artifacts and improving the overall quality of the reconstruction. [8, 49]

2.2 In-line Phase Contrast Imaging

Phase contrast imaging and x-ray imaging using phase shift information are not new concepts or techniques. Within the current technologies of phase contrast imaging, which include x-ray interferometry, diffraction-enhanced imaging (DEI) and in-line phase contrast imaging, the phase shift information has been successfully employed. However, both x-ray interferometry and DEI require highly monochromatic x-rays, a number of special optical devices and complicated system configurations. [50-52] On the other hand, the in-line phase contrast technique utilizes a similar system configuration as conventional radiography, with the addition of a specific object-to-detector distance. This distance introduces an air gap between the object and the detector so that phase gradients can be produced during x-ray propagation by the variation of fraction indices in the object. [53-55] Therefore, combined with the effects of conventional attenuation imaging, the resultant image comprises both attenuation and phase shift information. [55-56]

Mathematically, the refraction index of biological tissues is a complex parameter that can be represented by the following equation:

$$n = 1 - \delta + \mathrm{i}\beta, \tag{23}$$

where δ is the real part which represents the refraction index decrement result from the phase shifts and β is the imaginary part of the index which accounts for the x-ray attenuation. δ and β are given by: [53]

$$\delta = \left(\frac{r_e \lambda^2}{2\pi}\right) \sum_l N_l \left(Z_l + f_l^r\right) \tag{24}$$

and

$$\beta = \left(\frac{r_e \lambda^2}{2\pi}\right) \sum_l \left(N_l f_l^i\right). \tag{25}$$

λ – the wavelength of x-ray,

r_e – the classic electron radius,

Z_l – the atomic number of element *l* in the object,

N_l – the density of atoms,

f_l^r – the real part of the anomalous scattering factor,

f_l^i – the imaginary part of the anomalous scattering factor.

The linear attenuation coefficient, $\mu(x, y)$, and z-projections of the corresponding phase shift, $\phi(x, y)$, during the propagation of the x-ray are given by the complex x-ray transmittance: [57, 58]

$$T(x, y) = \mathrm{e}^{-i\phi(x,y) - \int \frac{\mu(x,y,z)}{2} dz} \tag{26}$$

where:

$$\mu(x, y) = \frac{4\pi}{\lambda} \int \beta(x, y, z) \mathrm{d}z \tag{27}$$

and

$$\phi(x, y) = \frac{-2\pi}{\lambda} \int \delta(x, y, z) \mathrm{d}z, \tag{28}$$

where plane wave propagation along the orientation of the incident x-ray is assumed. Given the parameters involved in Equations (24) to (26) above, the relative values of μ and ϕ can be determined. Through theoretical calculations, numerous studies indicated

that the difference in x-ray phases can be up to 1000 times greater than that in attenuation coefficients. [53, 55, 57, 58] Therefore, in-line phase contrast can significantly improve the image quality, especially in distinguishing the boundaries between normal and malignant tissues, as those two types of tissues are different in refraction indices. Theoretical evaluation of the edge enhancement has derived a formula to elucidate the relationship between the contrast and the phase through the description of resultant imaging intensity, from which the contrast can be determined. This relationship is as follows: [53]

$$I(x,y) \approx \frac{I_0}{M^2} \cdot \left[1 - \frac{\lambda R_2}{2\pi M} \nabla^2 \phi\left(\frac{x}{M}, \frac{y}{M}\right)\right]. \tag{29}$$

In this formula, I is the intensity, M represents the geometric magnification of the in-line phase contrast system and R_2 refers to the object-to-imaging distance (OID). The equation indicates that the contrast is proportional to the Laplacian of object's projected phase shifts, ϕ. Therefore, higher contrast on the resultant image will be obtained through larger phase shifts occurring during the propagation of the x-rays. As indicated in previous sections, the phase shifts will be increased on the physical boundaries between tissues with different compositions, thus the imaging qualities due to the contrast can be improved.

Phase retrieval is a method that is able to locate and extract phase shifts among tissues with different physical natures from phase contrast projections. In order to improve the imaging capability for a tomosynthesis imaging technique, phase retrieval is employed as image preprocessing onto the angular projections before reconstructions.

In general, phase retrieval is based on the x-ray propagation equation, which reveals how the phase shifts are encoded in the image intensity variations. Common phase retrieval methods in the literature require multiple projections (at least two projections) acquired with varying object-detector distances for retrieval of the phase-shift map of a subject. [13-15] However, this requirement of multiple image acquisitions for phase retrieval is cumbersome in implementation, and multiple exposures multiply the radiation dose. In searching for a better phase retrieval method, it has been noted that when a subject made of elements with $Z<10$, such as soft tissues or acrylic, etc., is imaged with high energy x-rays (60 keV or higher), the x-ray-matter interactions are dominated by the x-ray Compton scattering from atomic electrons, due to the fact that the x-ray photoelectric absorption and coherent scattering are diminished. In this case, which is known as the phase-attenuation duality (PAD), [13] both the tissue attenuation and phase shift are determined by subject electron density distributions. When the conditions of the phase-attenuation duality hold, the x-ray propagation equation becomes simplified and the phase map can be retrieved from just a single phase-sensitive projection. The clinical feasibility of high-energy phase contrast mammography based on the in-line principle has been reported and the potential has been demonstrated to improve the signal-to-noise ratio (SNR) at a reduced radiation dose in phantom experiments. [17-21] However, to the best of my knowledge, digital tomosynthesis combined with the high-energy in-line phase contrast technique has not been reported previously.

Chapter 3. Development of a High-energy In-line Phase Contrast Tomosynthesis Prototype

3.1 In-line Phase Contrast Tomosynthesis

As detailed in the previous sections, tomosynthesis images are acquired through the use of a complicated reconstruction process. Angular projections used for tomosynthesis reconstructions are conventionally obtained through digital radiography. The angular projections contain no phase information and x-rays experience no phase shifts during the propagation, thus the resultant reconstructed images demonstrate only attenuation contributions. On the other hand, in-line phase contrast imaging includes the contributions of phase effects, and has been proven efficient in providing edge enhancement at the boundaries between soft tissues with different refraction indices, thus increasing the image quality. However, phase imaging faces the challenge of overlapping, which results from superimposed soft tissue structures, and previous research has not been able to completely eliminate this issue. In order to solve this problem, an emerging method known as in-line phase contrast tomosynthesis, which combines the methodologies and prototypes of phase contrast and digital tomosynthesis, has been demonstrated useful and powerful in removing structure noise, as well as increasing the image quality. [41, 59-60]

In the design and implementation of an in-line phase contrast tomosynthesis prototype, considerations basically stem from the conceptual aspects of the in-line phase contrast system. As source-to-object distance (SOD, R_1) and object-to-imaging distance (OID, R_2) can significantly influence the amount of phase contrast effect and thus the image quality,

these two parameters are critical in designing the prototype and must be selected with careful consideration.

As detailed in Section 2.2, an adequate amount of phase shifts generated through acquiring angular projections must be ensured in order to demonstrate high image contrast on the boundary of tissues with different properties. To achieve this goal, a microfocus x-ray tube with an extremely small focal spot is used to attain high spatial coherence, which is critical in phase contrast imaging. The spatial coherence is also increased in the design of the prototype through introducing an air gap between the object and the detector, which ensures that the diffracted x-ray photons can travel a sufficient lateral distance to produce the phase shift effects on the output image. [50] Previous studies investigating the selection of the geometric values showed that a magnification factor of around 2.5 is the optimal value for constructing a phase contrast prototype. [50, 56] The details of the overall description of the in-line phase contrast tomosynthesis prototype will be presented in the following sections.

3.2 Selection of High-energy Operation

The long distance between the object and the detector utilized in the in-line phase contrast technique will result in fewer x-ray photons received by the detector as compared to the contact mode detection used in conventional DBT, under the same conditions of exposure parameters, radiation dose delivery and detector ability. Thus, an in-line phase contrast tomosynthesis system can hardly deliver similar imaging ability to a conventional tomosynthesis system, due to the low attenuation contrast. In an effort to solve this

problem, high-energy x-ray imaging, which has already been employed in chest radiography, can compensate for the loss of x-ray photons during a long-distance propagation, based on a relationship among the number of photons (N), the tube voltage, kV, and the tube current multiplied by exposure time (mAs) as follows: $N \propto kV^2 \cdot mAs$, [4] which will allow for most of the attenuation contrast to be preserved. In addition, due to the high penetrability and low absorption of high-energy x-ray photons, the radiation dose received by patients can also be potentially reduced. Finally, since phase contrast decreases much slower than attenuation with increasing x-ray energy, the phase retrieval method as presented here can be employed for high-energy in-line phase contrast imaging to preserve the bulk of the phase contrast.

3.3 System Design

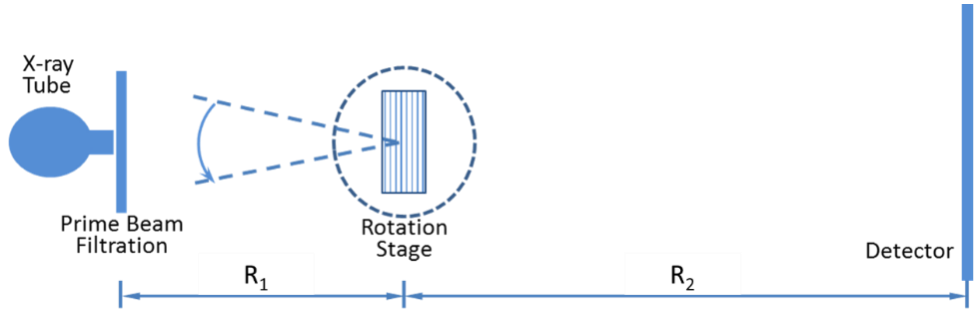

Figure 5: Schematic of an in-line phase contrast tomosynthesis system prototype.

In this dissertation research of a high-energy in-line phase contrast tomosynthesis prototype, the x-ray source, the rotation stage and the detector are aligned along a calibrated optical rail. The center of the rotation stage is treated as the central location of objects. The source-to-object distance (SOD, R_1) and object-to-image distance (OID, R_2) will be selected to deliver optimal phase shift effects according to the principles of in-line phase contrast imaging, as well as to reduce the loss of x-ray photons during propagation

through the air gap. [53, 57, 61] The objects to be tested will be mounted on the center of the rotation stage. The configuration of the experimental in-line phase contrast tomosynthesis system prototype is depicted in Figure 5.

3.4 Devices Specification

3.4.1 X-ray Source

Figure 6: X-ray Source (Model L8121-01, Hamamatsu Photonics).

A micro focus x-ray source will be employed for the angular image acquisition. A picture of the x-ray source is presented in Figure 6. The target of this x-ray source is made of Tungsten, and the Beryllium output window has a thickness of 200 μm. The distance from the focal spot to the output window is 17 mm. The x-ray tube generates x-ray photons ranging from 40 to 150 kV with an adjustable tube current. The nominal focal spot sizes of 7, 20, and 50 μm can be selected and/or determined by the desired output power of 10, 30, or 75 W, respectively.

3.4.2 Detecting Systems

CMOS Flat Panel Detector

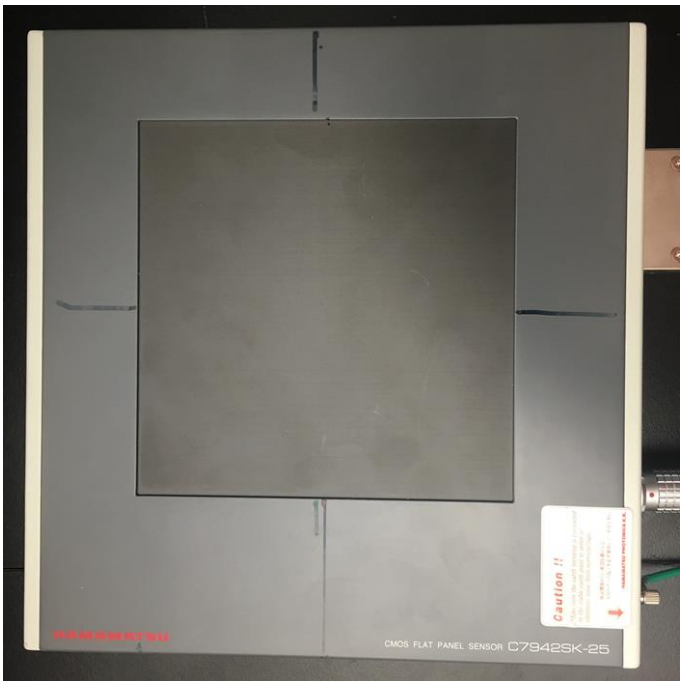

Figure 7: CMOS flat panel detector (C7942SK-25, Hamamatsu Photonics).

The CMOS flat panel detector employed in the phantom studies incorporates a GOS (Gadolinium oxysulfide) scintillator deposited onto a fiber optical plate (FOP), which is mounted on high sensitivity CMOS sensors. A picture of this detector is presented in Figure 7. This detector provides 50 μm of sampling pixel pitch on a 120 mm×120 mm active photodiode area. The electronic noise of this detector is 1100 electrons.

CCD Detector

Figure 8: CCD flat panel detector (Imagestar 9000, Photonic Science).

Another image grabber used in this dissertation research was a CCD detector, which is coupled with a CsI:Tl scintillator to convert x-ray photonic signals into light that can be sensed by a CCD detector. This detector provides 66 mm×66 mm active sensing area and 21.6 μm of sampling pixel pitch. The efficient spatial resolution for non-binning detecting mode is approximately 21 lp/mm. A picture of this detector is presented in Figure 8.

3.4.3 Rotation Stage

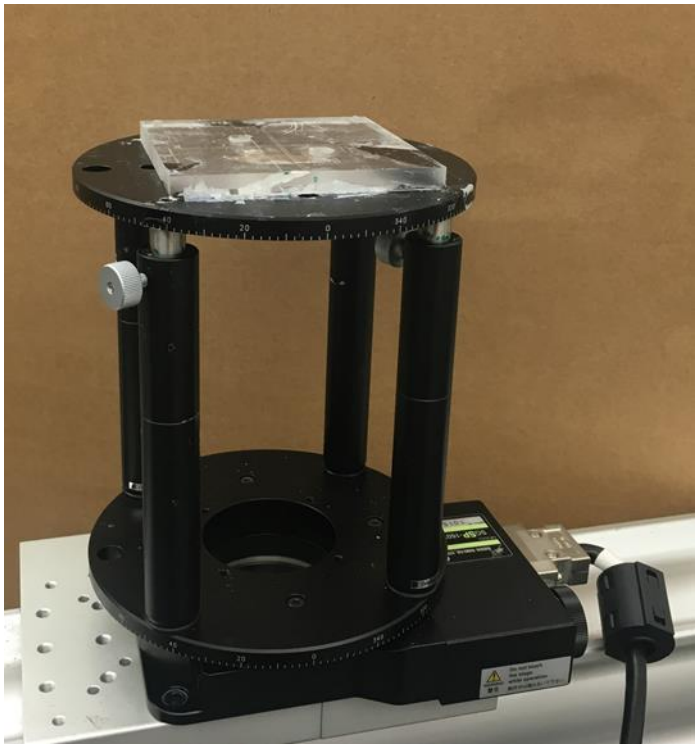

Figure 9: Motorized rotation stage (Model SGSP-160YAW, OptoSigma).

The rotation device utilized to provide the tomosynthesis mechanism was a motorized rotation stage (Model SGSP-160YAW, OptoSigma), which is shown in Figure 9. This rotation stage provides 0.0025°/pulse angular resolution.

3.5 Reconstruction

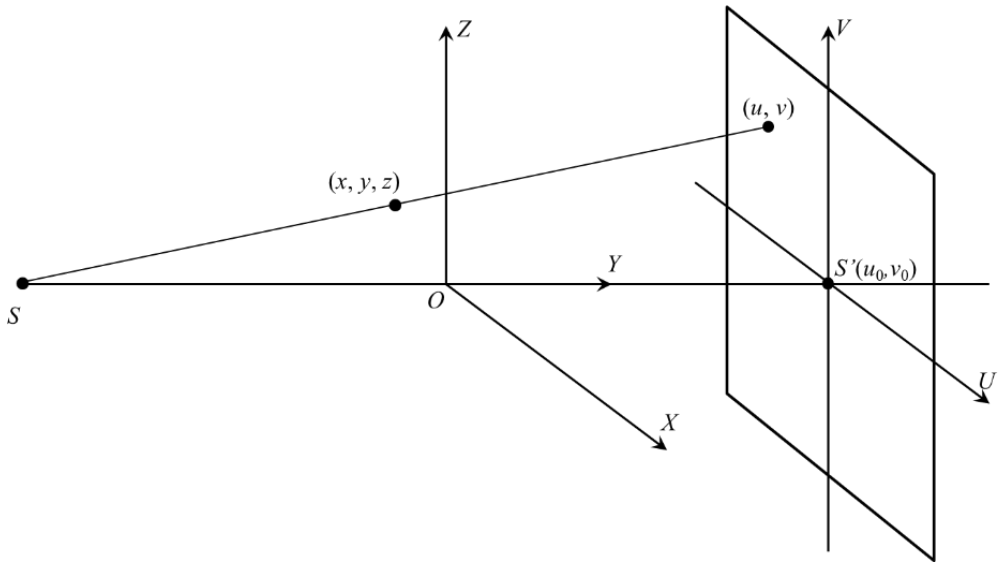

Figure 10: Schematic diagram illustrating the geometry of the object space and the detector plane. S, S′ and O represent the x-ray focal spot, the x-ray focal spot mapped on the detector plane and the isocenter of the system, respectively.

The reconstruction algorithm employed in this dissertation research is a modified Feldkamp–Davis–Kress (FDK) backprojection algorithm. [62-65] It is a versatile and powerful reconstruction method for digital tomosynthetic imaging tasks. Several studies have employed a modified FDK reconstruction algorithm for laboratory tomosynthesis prototype characterizations, and have demonstrated that this algorithm is able to provide a reconstructed image with high spatial resolution and contrast, as well as minimal artifacts resulting from the incomplete sampling characteristics due to the nature of tomosynthesis.

As illustrated by the tomosynthesis geometry in Figure 10, the following formula expresses the algorithm reconstructing a certain slice at depth, y_0, from a set of 2D angular projections, $P(u, v, \theta)$.

$$f(x, y_0, z) = \int_{\min\theta}^{\max\theta} \frac{C(x,y_0,z)\cdot D^2}{(D-s)^2} \int_{-\infty}^{\infty} \frac{D}{\sqrt{D^2+u^2+v^2}} \times P(u, v, \theta) \cdot H(\frac{D\cdot t}{D-s} - u) du d\theta, \quad (30)$$

where $f(x, y_0, z)$ represents the reconstructed image at the given slice with y_0, D is the source-to-isocenter distance or source-to-object distance (SOD, R_1) in the experiments, $H(\cdot)$ represents the one-dimensional Ramp filter along the tube-swept orientation on the detection plane aiming to invert the blurring caused by the sampling and the backprojection, $P(u, v, \theta)$ is the projection value of the projection coordinate (u, v) from a projection view θ, and $\mathrm{C}(x, y_0, z)$ is the compensation weighted factor which is experimentally and optimally determined by the following: [66]

$$\mathrm{C}(x, y_0, z) = 1/\cos[1.3z/(D - \sqrt{x^2 + {y_0}^2 + z^2}). \quad (31)$$

3.6 Phase Retrieval

In the in-line phase contrast tomosynthesis method presented in this dissertation, PAD phase retrieval methods will be employed as a preprocessing step to the angular projections. For a given task of tomosynthesis acquisitions, the phase map can be retrieved from each single angular phase-sensitive projection as follows: [13, 58]

$$\phi(\vec{r}) = \frac{\lambda r_e}{\sigma_{KN}} \cdot \ln\left\{\left[1 - \left(\frac{\lambda R_2}{2\pi M} \cdot \frac{\lambda r_e}{\sigma_{KN}} \cdot \nabla^2\right)\right]^{-1} \left(\frac{M^2}{I_{in}} \cdot I(\overrightarrow{r_D})\right)\right\}, \quad (32)$$

where $\phi(\vec{r})$ represents the phase map of the object, λ is the average wavelength of x-ray, σ_{KN} is the Klein-Nishina total cross-section of Compton scattering, and $r_e = 2.818 \times 10^{-15}$m denotes the classical electron radius. In addition, $I(\overrightarrow{r_D})$ represents the acquired phase-sensitive intensity of the object at $\overrightarrow{r_D}$ on the detector; and the image contrast is a mixed attenuation contrast and phase contrast prior to phase retrieval. I_{in} is the entrance x-ray intensity, and R_2 and M are the object-to-detector distance and the

magnification of the system, respectively. Also in Eq. (32). ∇^2 denotes the two-dimensional transverse Laplacian differential operator derived from the x-ray propagation equations.

Chapter 4. Characterization of a High-energy In-line Phase Contrast Tomosynthesis Prototype

The high-energy in-line phase contrast tomosynthesis prototype presented and the characterization works in this chapter had been published in the Journal of Medical Physics with Dr. Hong Liu as the first-of-kind results in May, 2015.

4.1 Introduction

In this study, a prototype of an in-line phase contrast tomosynthesis system operating under high-energy x-ray output was demonstrated with specific system parameters and settings. As detailed in this chapter, a comprehensive investigation was performed employing both quantitative objective measurements and subjective observation.

First, the modulation transfer function (MTF) and noise power spectrum (NPS) were measured to quantitatively measure the spatial resolution capabilities and noise features of the imaging system. In addition to the objective characterizations, the edge enhancement-to-noise ratio (EE/N) was calculated using an acrylic edge as a supplementary measurement to demonstrate that a high-energy in-line phase contrast tomosynthesis system can provide imaging abilities similar to and/or comparable with a conventional digital tomosynthesis system under a comparable dose level. In the phantom studies, the images of a bubble wrap phantom, a fishbone-wax phantom and a chicken breast phantom provided both qualitative and observable comparisons of the images. By applying PAD phase retrieval to the in-line phase contrast projections as a preprocessing step before reconstruction, the image quality improvement was depicted as the increase in contrast-to-noise ratio (CNR). For comparison purposes, the results were compared with digital tomosynthesis operated at conventional mode.

4.2 Experimental Settings

The prototype of the high-energy in-line phase contrast tomosynthesis system was presented in Chapter 3, but the experimental parameters and system settings for the studies presented in this chapter will now be specified.

In this study, the in-line phase contrast angular images were acquired with 120 kVp tube voltage, 500 μA tube current and 50 μm spot size. An aluminum (Al) filter with 2.5 mm thickness was utilized to harden the beam and remove x-ray photons with energies less than 30 keV. The resultant percentage of removed photons, 64.4%, was experimentally calculated with the following formula: $\frac{N_0(30)-N_{\text{filter}}(30)}{N_0(30)}$, where $N_{\text{filter}}(30)$ represents the cumulative number of photons under 30 keV with Al filter and $N_0(30)$ represents the cumulative number of photons under 30 keV without Al filter. A comparison of the x-ray output spectra illustrating the percentage of x-ray photons as a function of x-ray energy for different filtration levels is shown in Figure 11. The image grabber used to acquire the angular projections was the Hamamatsu CMOS flat panel detector detailed in Section 3.4.2. The rotation device utilized to provide the tomosynthesis mechanism was the OptoSigma motorized rotation stage, Model SGSP-160YAW, detailed in Section 3.4.3.

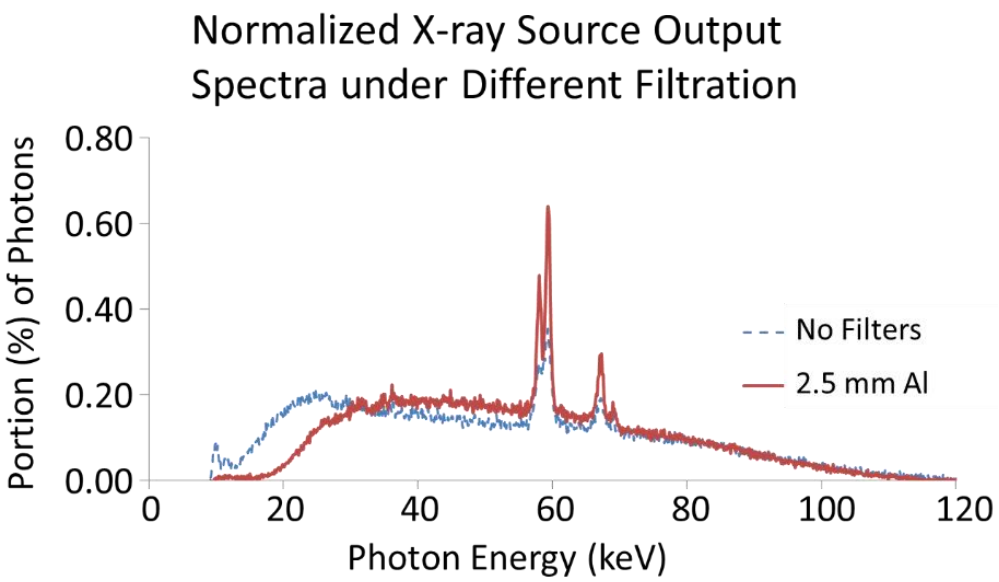

Figure 11: Normalized x-ray source output spectrum obtained under 120 kVp with the different filtration modes of no filter and a 2.5-mm Al filter.

Shown in Figure 12, the tested objects were placed at the center of the rotation stage. The objects were rotated with respect to the rotation center from -30° to +30° in 2° increments. This experimental setting provides 31 angular scans. The source-to-object distance (SOD, R_1) and the source-to-image distance (SID, R_1+R_2) values were 76.2 cm and 190.5 cm, respectively. For comparison purposes, the conventional digital tomosynthesis experiments were conducted with experimental settings of 40 kVp, 500 µA, 50 µm spot size, SOD = 76.2 cm and SID = 86.4 cm, the configuration of which is shown in Figure 13.

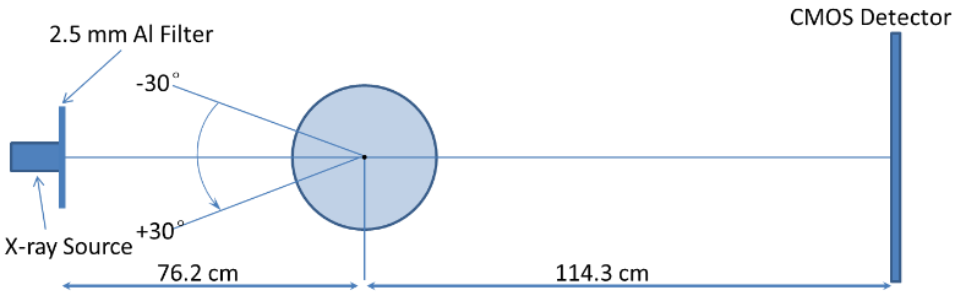

Figure 12: The configuration of the high-energy in-line phase contrast tomosynthesis system used in this research.

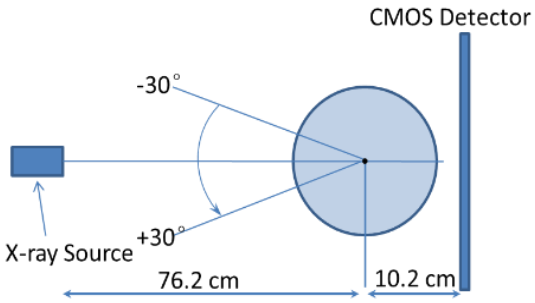

Figure 13: The configuration of the conventional digital tomosynthesis prototype for comparison experiments.

After angular projections of the test objects were acquired by the system, the series of projections were processed by the modified Feldkamp–Davis–Kress (FDK) backprojection algorithm detailed in Section 3.5. In order to demonstrate the ability of PAD phase retrieval, the angular projections were processed by the PAD phase retrieval algorithm detailed in Section 3.6 before tomosynthesis reconstruction.

4.3 Objective Characterizations

4.3.1 MTF Measurements

Experimental determination of the Modulation Transfer Function (MTF) for this high-energy in-line phase contrast tomosynthesis prototype was performed by the presampled MTF method with a slanted sharp edge for tomosynthesis mode and a slit camera for projection mode for comparison. [67-69]

For the in-plane reconstructed MTF calculation, the sharp edge was a steel blade with an edge thickness of 0.2 mm, which is comparable with the tomosynthesis reconstructed slice thickness. As shown in Figure 14 (a), the edge phantom was mounted at the center of the rotation stage. As detailed in Section 4.2, it was also rotated from -30° to +30° with 2° increments to acquire the angular projections. The angular projections of the edge phantom were acquired under a total exposure of 93 mAs (500 μA × 6 s × 31 projections), tube voltage of 120 kVp and 50 μm spot size. The reconstructed in-plane edge image illustrated in Figure 14 (b) was used to calculate the in-plane MTF through

$$\mathrm{MTF}(f) = \frac{|\mathcal{F}\{\mathrm{LSF}(x)\}|}{\mathcal{F}\{\mathrm{LSF}(x)\}_{\max}}, \tag{33}$$

where x is the pixel size, $\mathcal{F}\{\cdot\}$ denotes the Fourier transform, $|\cdot|$ denotes the modulus operator, and

$$\mathrm{LSF}(x) = \frac{\mathrm{dESF}(x)}{\mathrm{d}x}, \tag{34}$$

where the 1D edge spread function (ESF) was calculated through averaging the horizontal profile intensities along the maximum-value line. The ESF acquired in this research is shown in Figure 14 (c).

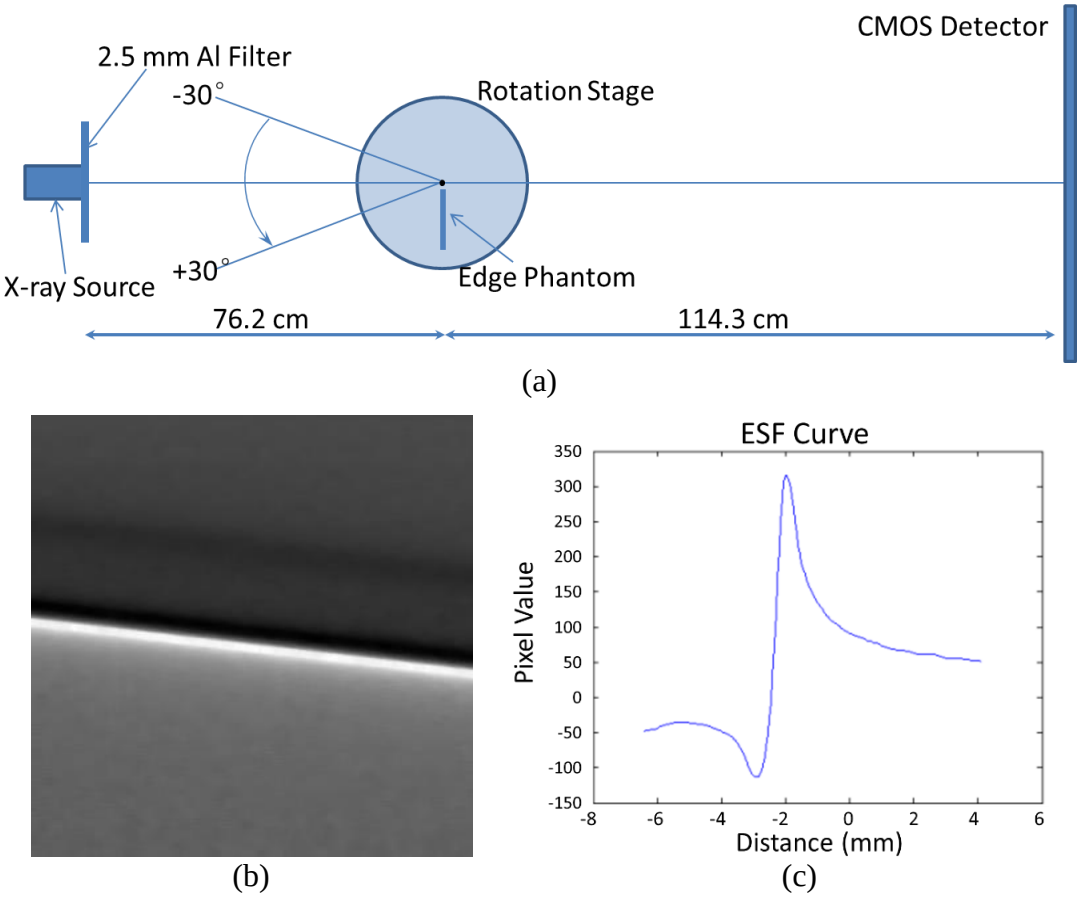

Figure 14: (a) Schematic of the experimental setup for measuring the in-plane MTF of the in-line phase contrast tomosynthesis system prototype. (b) Reconstructed in-plane image of the sharp edge phantom. (c) Edge spread function curve calculated from the in-plane image.

As a comparison, the in-line phase contrast projection MTF measurement was conducted using the same system configuration without rotation of the object. A 10 μm wide slit camera (iie GmbH, Aachen, Germany) was employed instead of the sharp edge to perform the presamped MTF measurement directly through the line spread function (LSF) method given in Equation (33). The projection of the slit camera was acquired under a total exposure of 3 mAs (500 μA × 6s), tube voltage of 120 kVp and 50 μm spot size.

4.3.2 NPS Measurements

The noise power spectrum (NPS) is a well-established method used to quantify the characteristics of fluctuations in the image. [2] The NPS calculation utilizes the Fourier transform of noise images to determine the variance of noise power as a function of spatial frequencies.

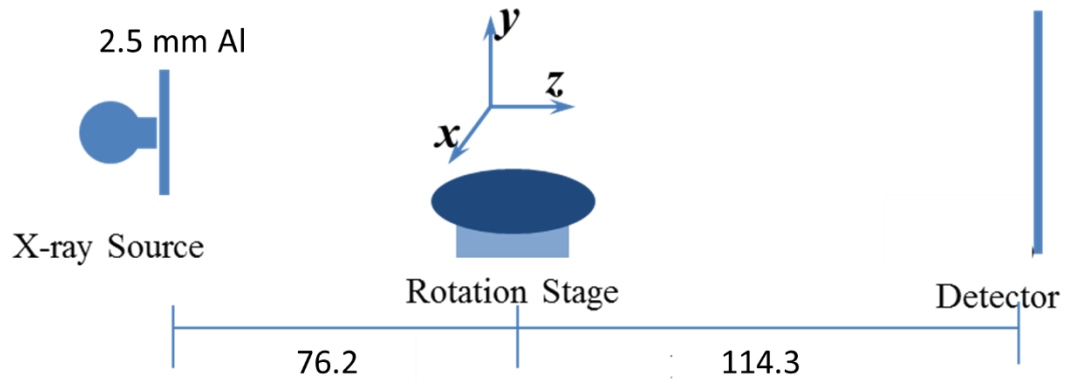

Figure 15: Schematic of the experimental setup for measuring the in-plane NPS of the in-line phase contrast tomosynthesis system prototype. The x-direction is the source-sweeping direction. (Unit: cm)

For the in-plane NPS calculation of the high-energy in-line phase contrast tomosynthesis prototype shown in Figure 15, the angular images were acquired under the no-object condition with a total exposure of 62 mAs (500 μA × 4s × 31 projections), a tube voltage of 120 kVp, and a focal spot size of 50 μm. Then the 31 angular projections were used to reconstruct a three-dimensional volume according to Equations (30) and (31). As there were no objects placed between the x-ray source and the detector, the volume represented the 3D intensity volume of the air with dimensions of 128×128×128 voxels. In experiments, 11 such volumes were acquired and reconstructed. The difference between two volumes was considered to represent the noise-only 3D volume image,

$$\text{Noise Volume}_n = I_n - I_{n+1} \quad (n = 1, 2, \dots \dots 11). \tag{35}$$

Then, the 3D NPS was determined by [70-72]

$$\mathrm{NPS}(f_x, f_y, f_z) = \frac{\Delta x \cdot \Delta y \cdot \Delta z}{N_x \cdot N_y \cdot N_z} \langle |\mathrm{FT}\{Noise\ Volume_n\}|_m^2 \rangle \quad (m = 1,2, \ldots 10), \quad (36)$$

where x, y, and z denote the directions indicated in Figure 15, Δx, Δy, and Δz are the pixel dimensions in corresponding dimensions, and $N_x \times N_y \times N_z$ is the number of voxels. The in-plane NPS, NPS(f_x, f_y), can be calculated by the integral of NPS(f_x, f_y, f_z) alone z-direction. [70]

As a comparison, in determining the projection NPS of this prototype system, the uniform noise images were acquired without any objects in the path of the x-ray beam. Due to the stochastic nature of noise in x-ray images, and considering the fact that the number of x-ray photons incident on each pixel of the detection plane can be represented as Poisson distributed variables, the 1024×1024 2D noise-only image was separated into 64 smaller regions of sub-images, each with a size of 128×128. The average noise image was calculated by averaging the sub-images. Next, the 2D Fourier transform was applied to the fluctuation image, which was obtained by subtracting the DC term from the noise-only images. [72-73]

4.3.3 Results of Objective Quantitative Measurements

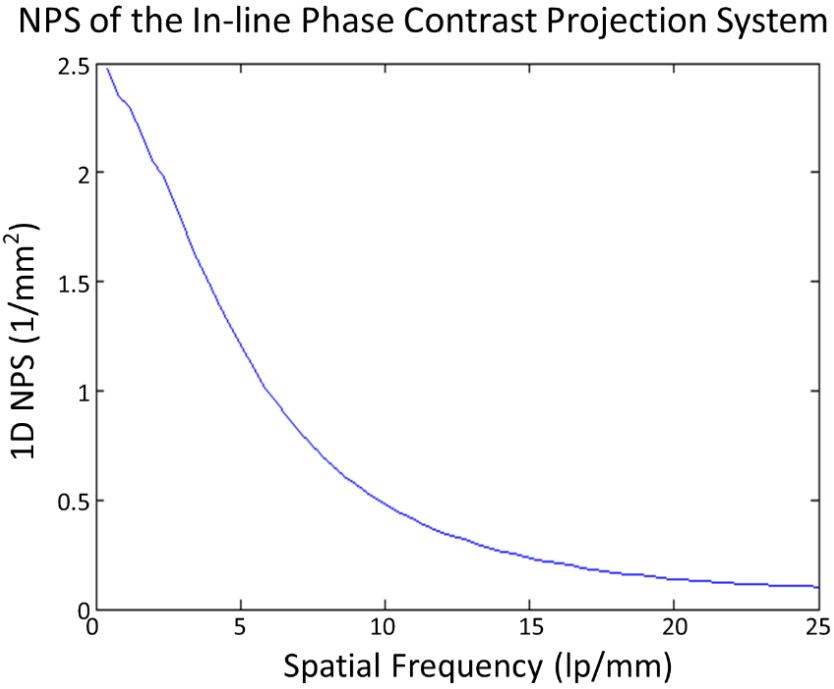

Figure 16: High-energy in-line phase contrast projection mode NPS curve.

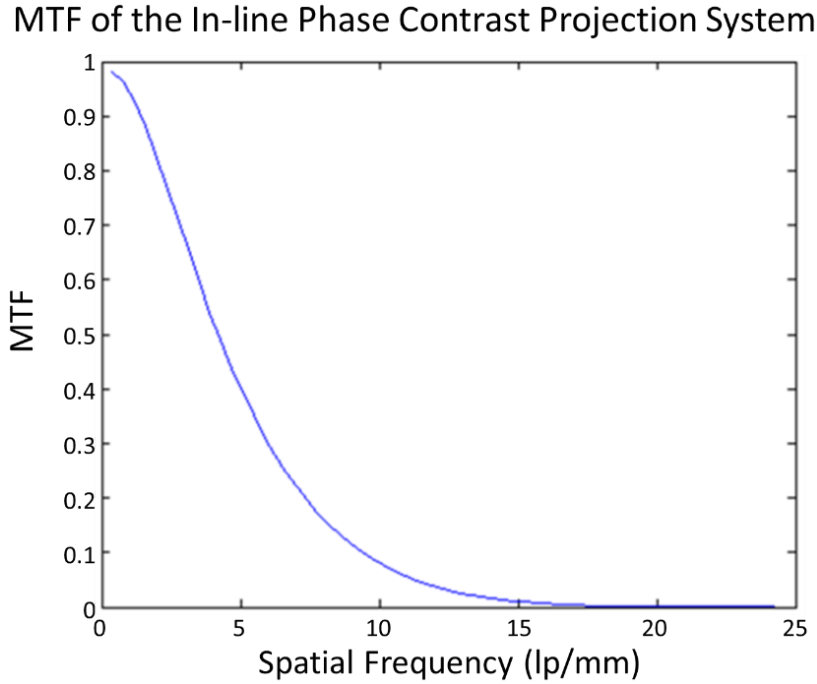

Figure 17: High-energy in-line phase contrast projection mode MTF curve.

Figures 16 and 17 present the NPS and MTF curves, respectively, which were measured and calculated based on the in-line phase contrast projection method using the slit camera. The results show the fundamental characteristics of noise and spatial resolution for the in-line phase contrast tomosynthesis prototype without introducing the reconstruction algorithm.

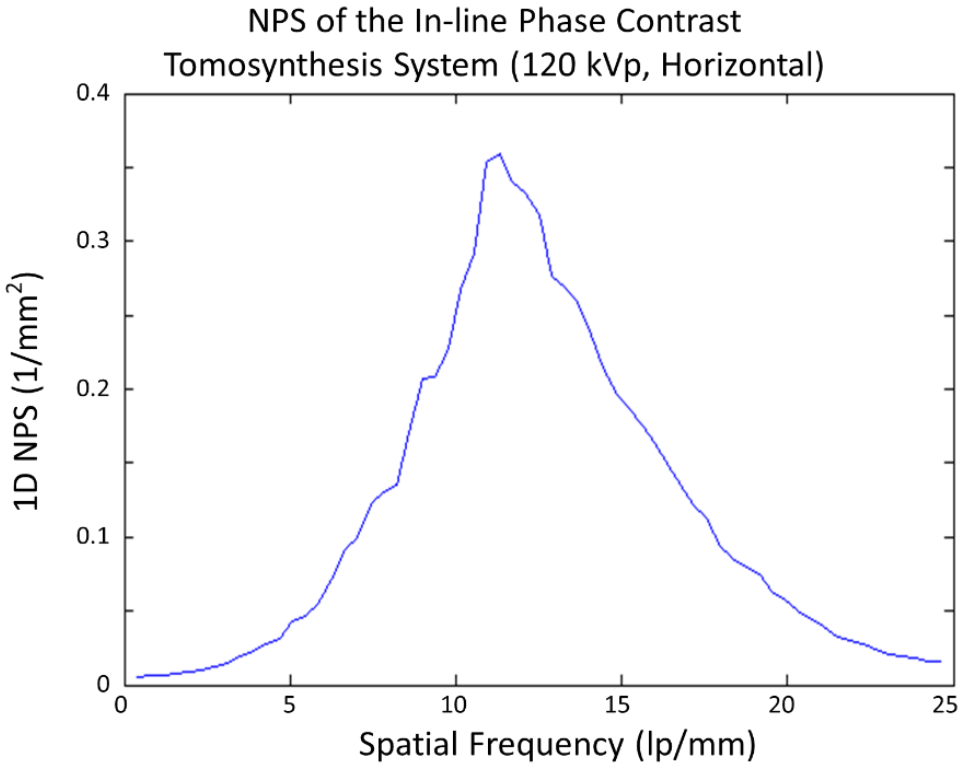

Figure 18: High-energy in-line phase contrast tomosynthesis prototype in-plane NPS curve.

Figure 18 shows the in-plane NPS curve of the high-energy in-line phase contrast tomosynthesis prototype. These quantitative results were calculated after tomosynthesis reconstruction, and therefore took the effects of the reconstruction algorithm into account.

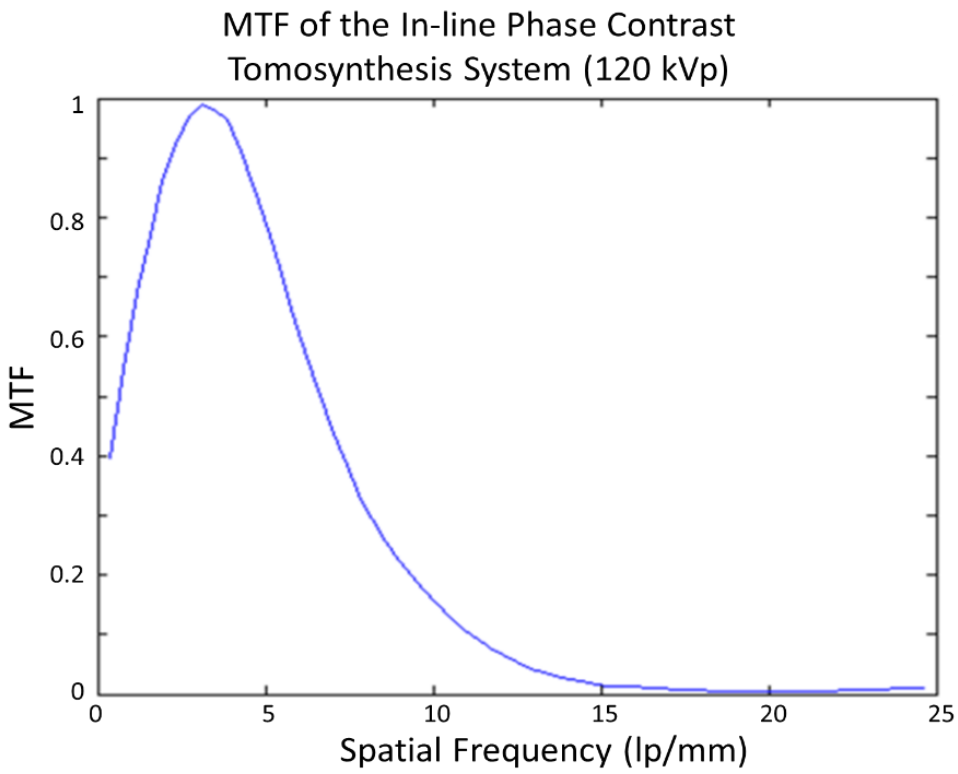

Figure 19: High-energy in-line phase contrast tomosynthesis prototype in-plane MTF curve.

Figure 19 shows the in-plane MTF curve of the high-energy in-line phase contrast tomosynthesis prototype. These quantitative results were calculated after tomosynthesis reconstruction, and therefore took the effects of the reconstruction algorithm into account.

Comparing the NPS curves measured with the high-energy in-line phase contrast projection mode in Figure 16 and the high-energy in-line phase contrast tomosynthesis mode in Figure 18, the noise within the images is at the same level and shares the same trend for spatial frequencies higher than 11.5 lp/mm. The obvious contrary behaviors occurring for lower spatial frequencies represent the effect of tomosynthesis, in which the reconstruction algorithm, especially the ramp filter used in backprojection, suppresses the image signals with relatively low spatial frequencies along the tube sweeping

direction, although the insufficiency of angular projections may also induce this defect on a quantitative curve. [67-70, 74-78] This phenomenon can also be observed in the high-energy in-line phase contrast tomosynthesis in-plane MTF curve in Figure 19 when comparing with the high-energy in-line phase contrast projection mode MTF shown in Figure 17.

4.4 Edge-enhancement-to-noise Ratio

The reconstructed tomosynthesis in-plane images of the edge phantom used in the MTF measurements acquired by conventional tomosynthesis and the high-energy in-line phase contrast imaging systems can be compared using the concept of edge enhancement-to-noise ratio (EE/N), which is defined as follows: [55]

$$\frac{EE}{N} = \frac{\text{Max}-\text{Min}}{\sqrt{\frac{\sigma_{\text{L}}^2+\sigma_{\text{H}}^2}{2}}} \tag{37}$$

where Max, Min, σ_{L} and σ_{H} denote the maximum intensity value of the edge, the minimum intensity value of the edge, the standard deviation of the lower-side background, and the standard deviation of the higher-side background, respectively. In the study presented in this chapter, the backgrounds of the edge were defined as regions of 12 pixels adjacent to the left and right of the edge. The averaged horizontal profile intensities along the maximum-value lines were plotted for calculating $\frac{EE}{N}$. The plotted 1D edge profiles of the two imaging methods are presented in Figure 20. The conventional tomosynthesis in-plane image of the edge phantom was taken at 40 kVp and 93 mAs, with an SOD of 76.2 cm and an SID of 86.4 cm. These plots were calculated after tomosynthesis reconstruction and took the effects of the reconstruction algorithm

into account. Since the tomosynthesis reconstruction is a limited angle tomography, the samples are not accurately reconstructed such that the residual effects of the ramp-filter used in the reconstruction remain. Hence all conventional tomosynthesis images exhibit some edge-enhancement in the tube-sweeping direction.

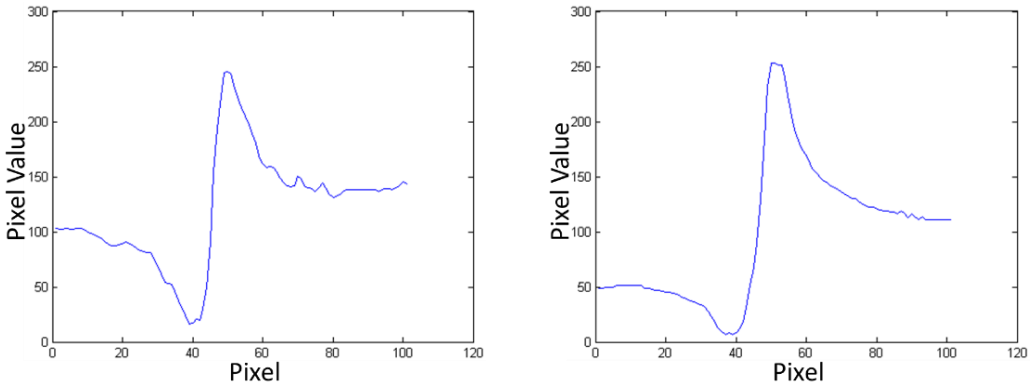

(a) (b)

Figure 20: Plotted edge profiles of the edge phantom imaged by using (a) conventional tomosynthesis and (b) high-energy in-line phase contrast tomosynthesis system.

Table 1. Comparison of Edge Enhancement-to-Noise Ratios

Method	Max	Min	σ_L	σ_H	EE/N	Uncertainty of EE/N
Conventional Tomosynthesis	245	16	8.18	4.39	24.68	5.77
High-energy In-line Phase Contrast Tomosynthesis	253	7	4.33	5.38	35.64	11.80

As the attenuation contrast decreases with increasing x-ray energies, a higher transmission of the 120 kVp beam would result in a lower absorption dose than that of 40 kVp beam, and the attenuation contrast of a 40 kVp beam image was supposed to be better than that of 120 kVp beam. Thus the relatively low entrance dose for the 120 kVp imaging with longer objective-to-imaging distance was expected to result in relatively low differences among maximum intensity value, minimum intensity value and back

ground. The calculated results of EE/N shown in Table 1 illustrated that the EE/N of the high-energy in-line phase contrast tomosynthesis modality was 1.44 times higher than that of conventional tomosynthesis. This phenomenon demonstrated that a high-energy in-line phase contrast tomosynthesis system can provide imaging abilities similar to and/or comparable with a conventional digital tomosynthesis system.

4.5 Phantom Studies

4.5.1 Phantom Design

Three laboratory designed phantoms were employed in this research: a five-layer bubble wrap phantom, a fishbone phantom and a chicken breast phantom. The fishbone simulates the tiny structures inside the soft tissues, and the bubble wrap phantom simulates lung structures/tissues as the mass attenuation coefficients among plastic and lung tissues are similar. [79] For the chicken breast phantom, fibrils and mass structures with different dimensions and shapes extracted from an ACR mammographic accreditation phantom were embedded into the chicken layers to simulate tumors inside the breast.

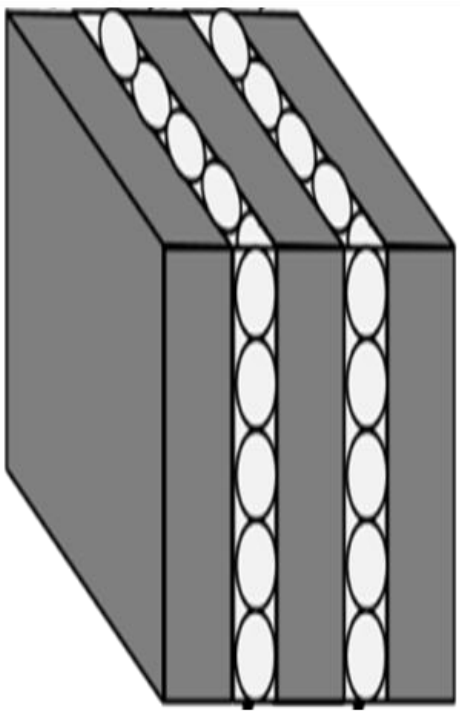

Figure 21: Schematic of the custom designed five-layer bubble wrap phantom.

The bubble wrap phantom, shown in Figure 21, was assembled with two pieces of bubble wrap sandwiched into three acrylic boards. The bubble wrap was constructed of low-density polyethylene $(C_2H_4)_n$ film, and acrylic has a molecular formula of $(C_5H_8O_2)_n$. The dimensions of each acrylic board are 114.3 mm high, 114.3 mm wide and 9 mm thick. The bubble wrap layers were each 2 mm in thickness.

Figure 22: The image of the fishbone phantom (left) and the bones inside the beeswax cube (right).

The fishbone phantom, shown in Figure 22, was constructed from a portion of the skeleton of a Crevalle Jack fish, which was purchased in the Asian food supermarket. The phantom included a portion of the vertebral column with attached neurapophysis-neural spine and ribs, which was sealed into beeswax ($C_{15}H_{31}COOC_{30}H_{61}$). The fishbone is made up of hydroxyapatite ($Ca_{10}(PO_4)_6(OH)_2$), calcium carbonate ($CaCO_3$), collagen and lipid. Although the fishbone contains elements with atomic numbers greater than 10, the effective atomic number of the bone is about 13, and the mass attenuation coefficient of bone is very close to beeswax when exposed by x-rays in the range of tens to hundreds of keV. [4, 80, 81] The dimensions of the fishbone phantom are 110.0 mm high, 70 mm wide and 110.0 mm thick along the axis of x-ray propagation.

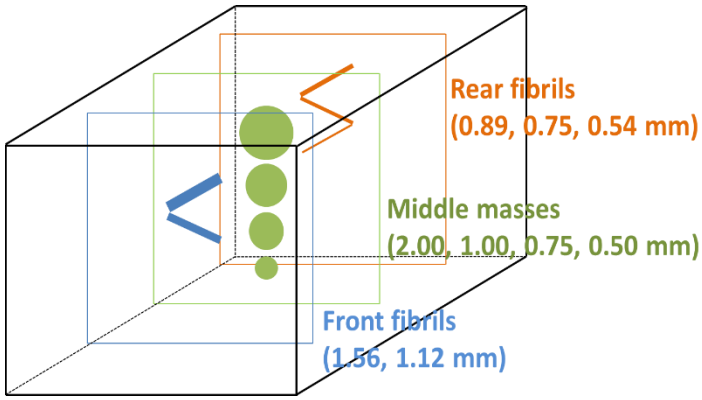

Figure 23: Schematic of the chicken breast phantom; the fibrils and masses were embedded at three different layers with a distance of approximately 10 mm between each layer.

The chicken breast phantom was made of a portion of chicken breast with a thickness of 60 mm, which was purchased in a supermarket. Three layers of test objects were embedded in the chicken breast with a distance of approximately 10 mm between each layer. The test objects included nylon fibrils with diameters of 1.56, 1.12, 0.89, 0.75 and 0.54 mm and tumor-like masses with thicknesses of 2.00, 1.00, 0.75 and 0.50 mm, which were extracted from an ACR mammographic accreditation phantom. A schematic of the phantom's internal structure is provided in Figure 23.

The bubble wrap phantom study was conducted with a total exposure of 124.0 mAs (500 µA × 8 s × 31 projections), 120 kVp, and 50 µm spot size, while the angular projections of the fishbone phantom were obtained under a total exposure of 155.0 mAs (500 µA × 10 s × 31 projections), 120 kVp, and 50 µm spot size. In the experiments with the chicken breast phantom, the angular projections were acquired under a total exposure of 258.4 mAs (500 µA × 16.67 s × 31 projections), 120 kVp, and 50 µm spot size. The experimental system configurations utilized in this study to acquire images of the phantoms are detailed in Figure 24 (a), (b) and (c), respectively.

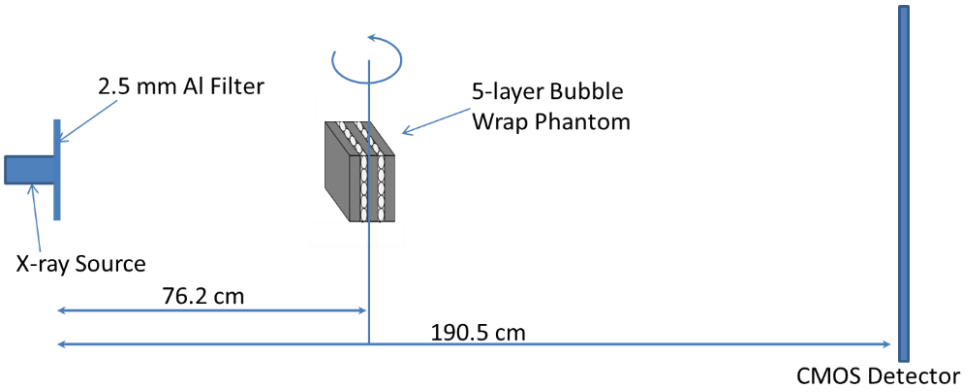

(a)

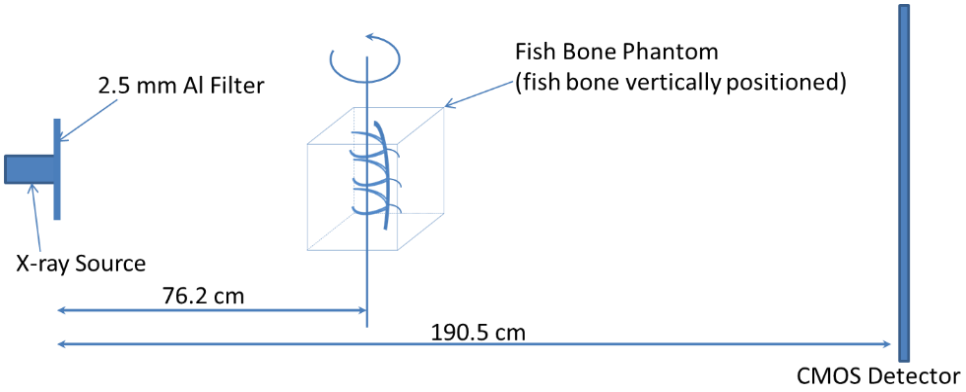

(b)

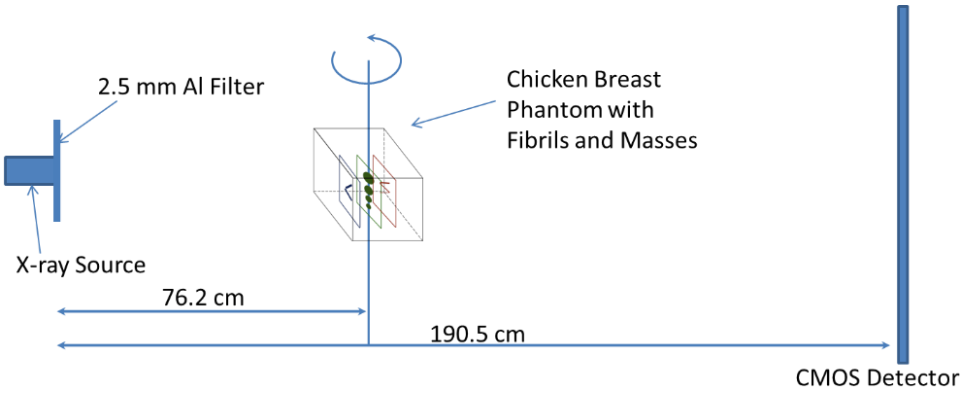

(c)

Figure 24: The experimental systems for measuring (a) the five-layer bubble wrap phantom, (b) the fishbone phantom, and (c) the chicken breast phantom with three layers of embedded fibrils and mass structures.

4.5.2 Observation Results of Phantom Study

Bubble Wrap Phantom

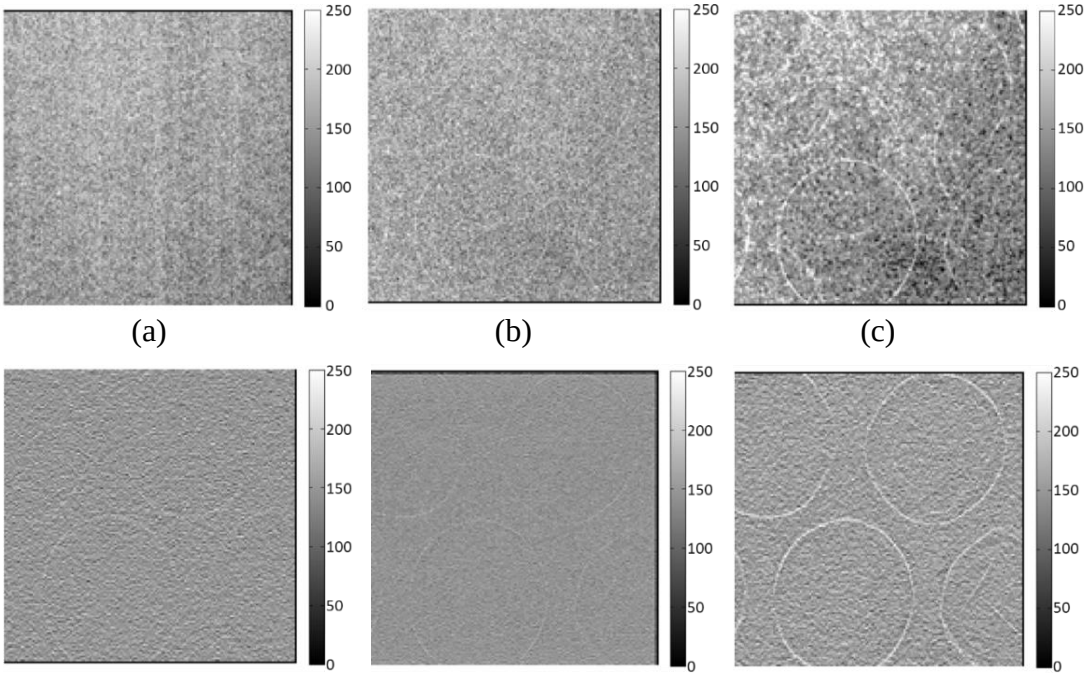

Figure 25: Bubble wrap phantom images acquired with the following methods: (a) conventional contact mode projection at 40 kVp, (b) high-energy in-line phase contrast projection at 120 kVp/2.5 mm Al filter, (c) phase-retrieved high-energy in-line phase contrast projection at 120 kVp/2.5 mm Al filter, (d) conventional tomosynthesis in-plane image at 40 kVp, (e) high-energy in-line phase contrast tomosynthesis in-plane image at 120 kVp/2.5 mm Al filter, and (f) high-energy in-line phase contrast tomosynthesis with phase retrieval method.

In the bubble wrap phantom study, the two pieces of bubble wrap were separated by a piece of acrylic board with a thickness of 9 mm. Considering the 2 mm thickness of each bubble wrap piece, the middle slices of the two bubble wrap layers were located at -5.5 mm and +5.5 mm with respect to the center of the entire phantom. The projection images (0° angular projection) and the reconstructed slices at -5.5 mm taken by the methods involved in comparison are shown in Figure 25 for comparison purposes. For the projection images shown in the first row, the superimposed structures render it difficult to distinguish the locations of the two bubble layers. On the contrary, the tomosynthesis reconstructed slices shown in the second row indicate the elimination of the overlapping; and the high-energy in-line phase contrast tomosynthesis image holds the same level of quality as the conventional mode tomosynthesis image through observation. Additionally, the image quality of the in-plane slices was increased by employing both the in-line phase contrast mechanism and the PAD phase retrieval method.

Fishbone Phantom

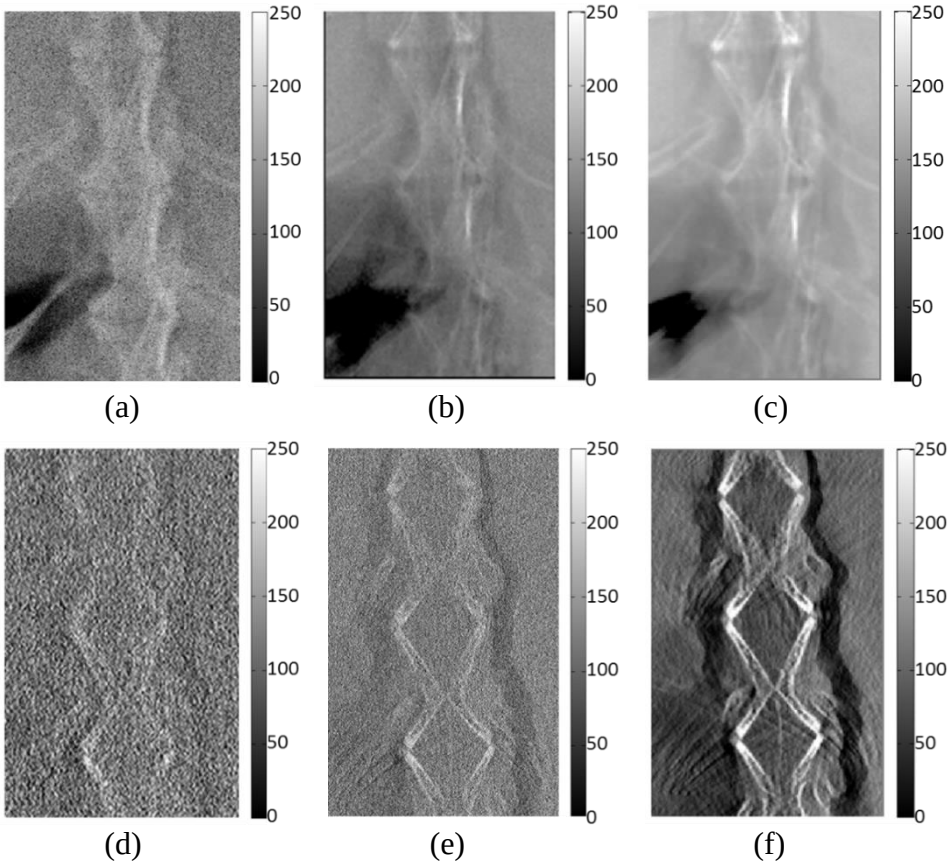

Figure 26: Fish bone phantom images acquired with the following methods: (a) conventional contact mode projection at 40 kVp, (b) high-energy in-line phase contrast projection at 120 kVp/2.5 mm Al filter, (c) phase-retrieved high-energy in-line phase contrast projection at 120 kVp/2.5 mm Al filter, (d) conventional tomosynthesis in-plane image at 40 kVp, (e) high-energy in-line phase contrast tomosynthesis in-plane image at 120 kVp/2.5 mm Al filter, and (f)) high-energy in-line phase contrast tomosynthesis with phase retrieval method.

In the fishbone phantom study, the projection images (0° angular projection) and the reconstructed slices at -7.5 mm taken by the comparison methods are shown in Figure 26. Exhibiting the phenomenon similar to the images presented in the previous section, the overlapping issue causes observers to be unable to distinguish the locations of the bones in the projections shown in the first row of Figure 26. However, the tomosynthesis reconstructed slices shown in the second row indicate that the superimposed structure was eliminated so that observers can clearly distinguish the bone structure at the plane. Additionally, the image quality of the in-plane slices was increased by employing in-line phase contrast mechanism and PAD phase retrieval method.

Chicken Breast Phantom

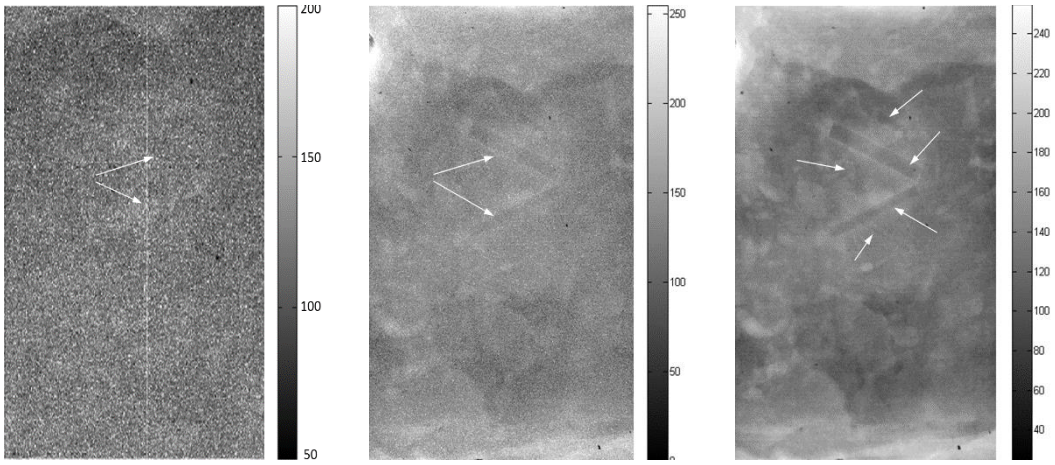

(a) (b) (c)

Figure 27: Chicken breast phantom images acquired with the following projection modes: (a) conventional contact mode projection at 40 kVp, (b) high-energy in-line phase contrast projection at 120 kVp/2.5 mm Al filter, (c) phase-retrieved high-energy in-line phase contrast projection at 120 kVp/2.5 mm Al filter. The arrows denote the objects that can be observed.

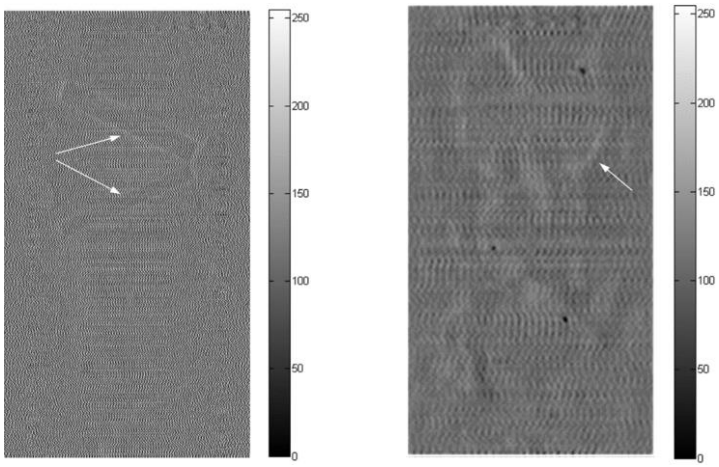

(a) (b)

Figure 28: In-plane chicken breast phantom images acquired with conventional tomosynthesis imaging under 40 kVp: (a) the front plane containing 1.56 and 1.12 mm fibrils, (b) the middle plane containing 2.00, 1.00, 0.75 and 0.50 mm masses. The fibrils with diameters of 0.89, 0.75 and 0.54 mm on the rear plane cannot be observed in the images acquired by using conventional tomosynthesis. The arrows denote the objects that can be observed.

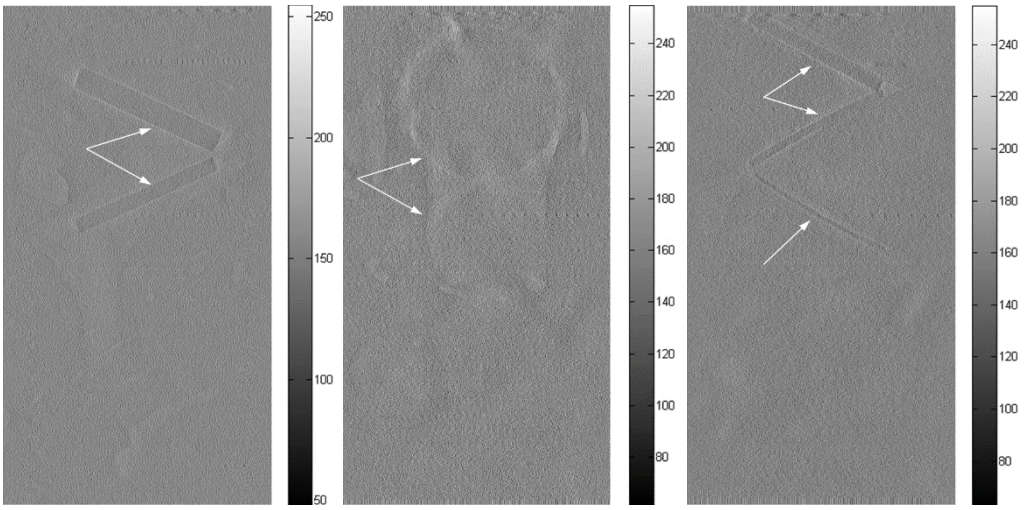

(a) (b) (c)

Figure 29: In-plane chicken breast phantom images acquired with in-line phase contrast tomosynthesis imaging under 120 kVp/2.5 mm Al filter: (a) the front plane containing 1.56 and 1.12 mm fibrils, (b) the middle plane containing 2.00, 1.00, 0.75 and 0.50 mm masses, and (c) the rear plane containing 0.89, 0.75 and 0.54 mm fibrils. The arrows denote the objects that can be observed.

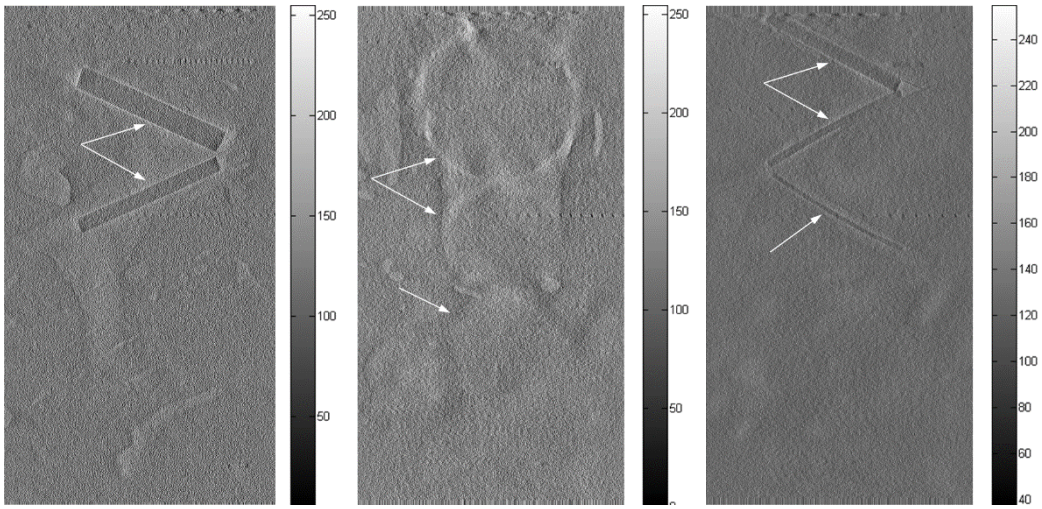

(a) (b) (c)

Figure 30: In-plane chicken breast phantom images acquired with in-line phase contrast tomosynthesis with phase retrieval method under 120 kVp/2.5 mm Al filter: (a) the front plane containing 1.56 and 1.12 mm fibrils, (b) the middle plane containing 2.00, 1.00, 0.75 and 0.50 mm masses, and (c) the rear plane containing 0.89, 0.75 and 0.54 mm fibrils. The arrows denote the objects that can be observed.

In this study of the biologically relevant phantom, the projection images and the reconstructed in-plane slices of the inserted structures in the chicken breast acquired by the different comparison methods are shown in Figures 27-30. As with the phenomenon in the images presented in the previous sections, the overlapping issue causes observers to be unable to distinguish the locations of the fibrils and masses on the projections shown in Figure 27. However, the tomosynthesis-reconstructed slices shown in Figures 28-30 indicate that the superimposed structures were eliminated, allowing observers to distinguish the structures and embedded objects at different planes within the phantom.

As shown in Figure 28, the conventional tomosynthesis images demonstrate poor contrast of the targets. One important difference between the ACR mammographic accreditation phantom and our chicken breast phantom should be noted. In the ACR phantom, the fibril and mass targets are embedded in a 7-mm thick wax plate (900 kg/m^3 in density), but the fibril and mass targets in our phantom are embedded in chicken breast (1121 kg/m^3 in density), which is much larger in mass density than the wax. Hence we expect that the intrinsic radiological contrast between the targets and chicken breast will be much lower than that between the targets and the wax in the ACR phantom, thus making it more difficult to clearly depict the targets.

Comparing the slices on different planes shown in Figure 28-30, the following observations can be made: (1) Although the fibrils on the front plane can be distinguished by the three presented methods, the image quality was dramatically increased by introducing the PAD retrieval method; (2) In the in-plane images of the middle plane, the

application of the PAD method not only increased the number of distinguishable masses, but also increased the image contrast; and (3) The fibrils with diameters of 0.89, 0.75 and 0.54 mm were not observable in the 40 kVp tomosynthesis reconstructions, but the images of these fibrils were observable by utilizing high-energy in-line phase contrast tomosynthesis, and the imaging quality was further enhanced by introducing the PAD method. Overall, the image quality of the in-plane slices was increased by employing the in-line phase contrast mechanism and the PAD phase retrieval method.

4.5.3 Contrast-to-noise Ratio Calculations

CNR of Bubble Wrap Images

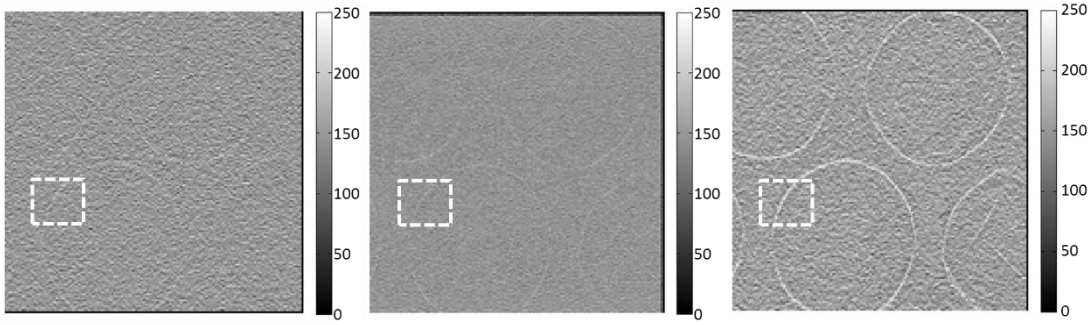

(a) (b) (c)

Figure 31: (a) Conventional tomosynthesis in-plane image of the bubble wrap phantom, (b) high-energy in-line phase contrast tomosynthesis in-plane image of the bubble wrap phantom image without phase retrieval, and (c) with phase retrieval. All three slices are at -5.5 mm from the center plane. The regions of interest selected to calculate CNR are denoted by the white squares.

In Figures 31 (a), (b) and (c), the in-plane images of the bubble wrap phantom were acquired by conventional tomosynthesis and high-energy in-line phase contrast tomosynthesis without and with phase retrieval, respectively. These slices of the bubble wrap phantom acquired through different methods were located the same distance from

the rotation center at -5.5 mm. From the in-plane images, the edges or the boundaries of the bubbles can be observed and easily distinguished in the image acquired with high-energy in-line phase contrast tomosynthesis through the usage of phase retrieval preprocessing on the angular projections. The edges and contours of the bubbles cannot be distinguished easily and clearly in the conventional tomosynthesis image. The relative CNR values were calculated by employing the following formula: [82]

$$CNR = \frac{I_S - I_B}{\sqrt{\frac{\sigma_S^2 + \sigma_B^2}{2}}} \tag{38}$$

where I_S, I_B, σ_S and σ_B represent the average intensity value of the bubble edge in the region of interest (ROI), the average intensity value of the background near the object, the standard deviation of the object intensities, and the standard deviation of the background intensities, respectively. The average intensity value of the bubble edge in the ROI was calculated by averaging the maximum value of 16 randomly-chosen intensity profile plots along the horizontal orientation. The background was a randomly-chosen 16-pixel-by-16-pixel no-object area within the ROI. The CNR values calculated based on the in-plane images of the 5-layer bubble wrap phantom are shown in Table 2.

Table 2. CNR by Different Imaging Methods for Bubble Wrap Imaging

Method	Noise	CNR
Conventional Tomosynthesis	22.51	1.61
High-energy In-line Phase Contrast Tomosynthesis without Phase Retrieval	11.33	4.98
High-energy In-line Phase Contrast Tomosynthesis with Phase Retrieval	6.61	12.34

The data in Table 2 indicates that the CNR of the bubble edge can be improved by approximately a factor of 2 by employing phase retrieval, as compared with high-energy in-line phase contrast tomosynthesis without using phase retrieval. Compared with the conventional tomosynthesis method, the CNR of the bubble edge can be improved by a factor of more than 6 when using high-energy in-line phase contrast tomosynthesis with phase retrieval. The discrepancy in the noise values among the tomosynthesis, phase contrast and PAD phase contrast methods can be attributed to the following reasons: 1) In in-line phase contrast imaging, the large air gap between the object and detector reduces scattering; 2) For conventional tomosynthesis imaging, the detector receives more scattered x-ray photons from the object compared to in-line phase contrast, based on the modalities used in this study; and 3) The PAD method not only retrieves the phase map of a phantom, but simultaneously reduces imaging noise, as the PAD-phase retrieval is essentially a robust integration procedure.

CNR of Fishbone Images

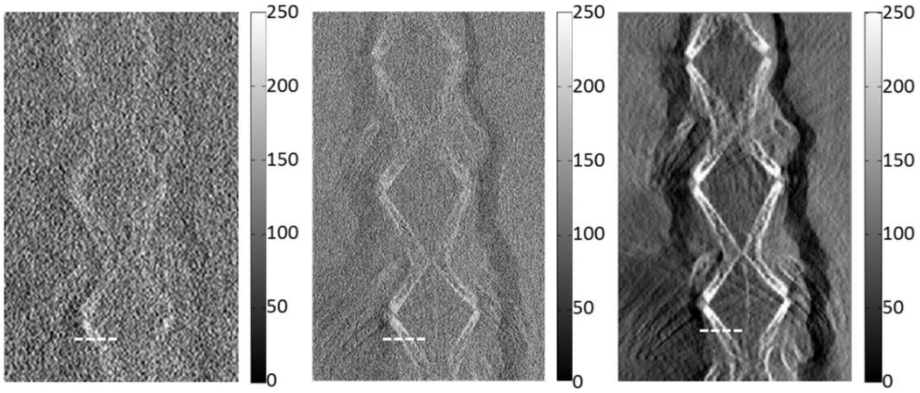

(a) (b) (c)

Figure 32: (a) Conventional tomosynthesis in-plane image of the fishbone phantom, and high-energy in-line phase contrast tomosynthesis in-plane images of the fishbone phantom (b) without phase retrieval, and (c) with phase retrieval at -7.5 mm. The regions of interest selected to plot intensity profiles are denoted by the dashed lines.

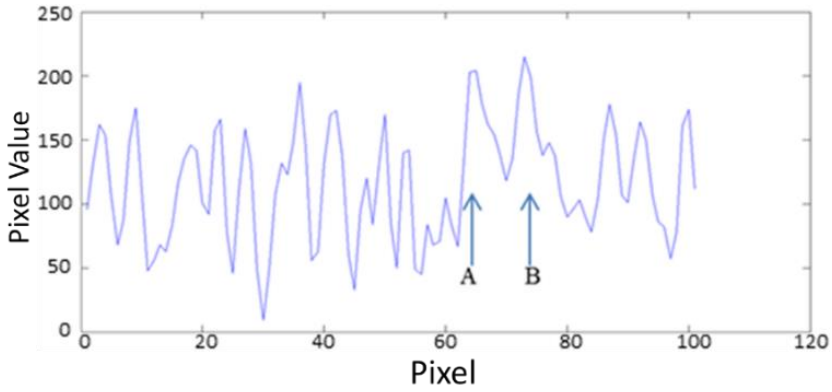

(a)

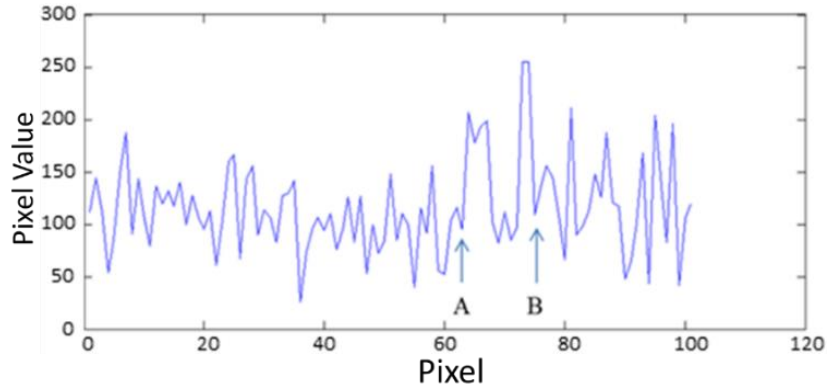

(b)

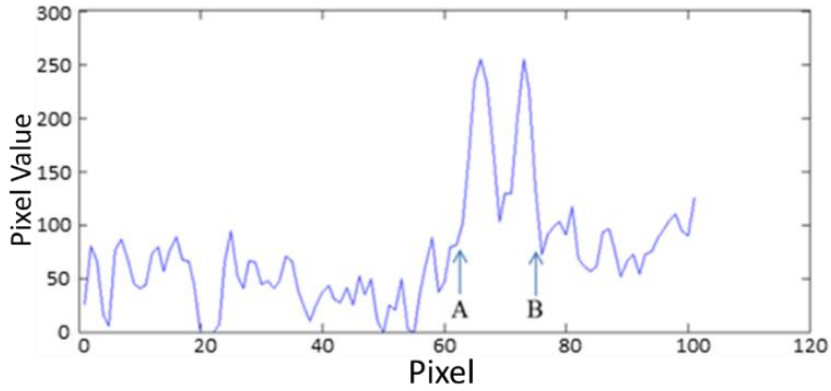

(c)

Figure 33: Plotted intensity profiles according to the illustrations in Figure 32 (a), (b) and (c), respectively. Letters A and B were used to denote the locations of the two bone structures.

In Figure 32, the in-plane images were acquired by conventional tomosynthesis and high-energy in-line phase contrast tomosynthesis without and with phase retrieval, respectively. These slices of the fishbone acquired through different methods were located the same distance (-7.5 mm) from the center of the phantom. For the in-plane images, the tiny structures of the selected area on the fishbone cannot be distinguished easily or clearly in the conventional tomosynthesis image. Despite the effect of the imaging magnification on spatial resolution, which further improves the ability of structure discrimination, the contrast in the image acquired through conventional tomosynthesis is still poor. It should be noted that the phase contrast effects with the tomosynthesis are diminished, as a short sample-detector distance was employed for conventional tomosynthesis, which did not provide the exiting phase-shifted x-rays with a sufficient propagation distance to interfere with each other to form phase contrast fringes. On the other hand, the details of the objects are fairly easily observed in the image acquired through high-energy in-line phase contrast tomosynthesis before applying phase retrieval preprocessing. However, comparing the intensity profiles in Figure 33 indicates that applying phase retrieval to the original angular projection images can be effective in suppressing image noise, which is also because of the noise suppression associated with the robust PAD-based phase retrieval method. [83]

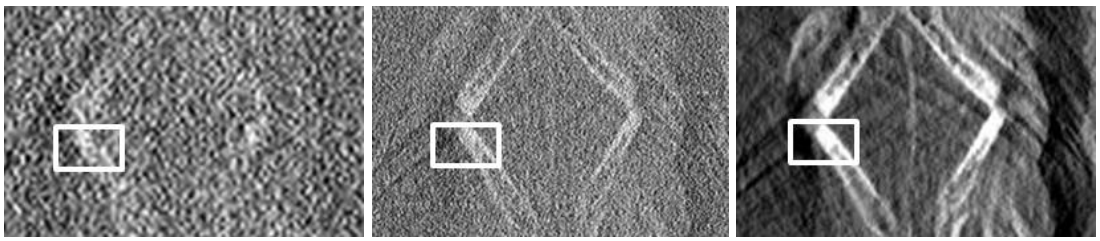

(a) (b) (c)

Figure 34: Regions of interest selected to calculate contrast to noise ratios for (a) Conventional tomosynthesis in-plane image of the fishbone phantom, and high-energy in-line phase contrast tomosynthesis in-plane images of the fishbone phantom (b) without phase retrieval, and (c) with phase retrieval.

Based on similar logic to that detailed previously and Equation (38), the average value of the fishbone in the ROI denoted by the white-line rectangle in Figure 34 was calculated by averaging values of an 8×8 area on the bone structure, while another 8×8 area adjacent to the bone structure was considered the image background. Calculated CNR values of the objects on the fishbone phantom images and the corresponding noise levels are provided in Table 3.

Table 3. CNR by Different Imaging Methods for Fishbone Imaging

Method	Noise	CNR
Conventional tomosynthesis	14.39	3.53
High-energy In-line Phase Contrast Tomosynthesis without Phase Retrieval	10.83	8.50
High-energy In-line Phase Contrast Tomosynthesis with Phase Retrieval	3.20	61.28

The data shown in Table 3 indicates that the CNR of the fishbone features can be improved by a factor of more than 7 by using phase retrieval with high-energy in-line phase contrast tomosynthesis, as compared to that without using phase retrieval. Compared with the conventional tomosynthesis method, the CNR can be improved by a factor of 17 by employing phase retrieval, and the noise values are at approximately the same level. The discrepancy in the noise values among the conventional tomosynthesis, phase contrast and PAD phase contrast can be attributed to the same reasons discussed in the bubble wrap phantom results.

4.5.4 Superimposed Structures Removal

Figures 25 (a)-(c), Figures 26 (a)-(c) and Figures 27(a)-(c) show the radiography projection image and in-line phase contrast projections acquired without and with PAD phase retrieval for the bubble wrap phantom, the fishbone phantoms and the chicken breast phantom, respectively. Comparing the different methods, the phase retrieved projection images in Figure 25 (c), Figure 26 (c) and Figure 27 (c) demonstrate improved image quality, as observers can easily detect the edges of the bubbles, sharp boundaries of the fishbone and some of the inserted structures inside the chicken breast, but structure overlapping still cannot be avoided. On the contrary, as shown in Figure 25 (d)-(e), Figure 26 (d)-(e) and Figures 28-30, the tomosynthesis mechanism facilitates the reconstruction of the in-plane images, which allows observers to distinguish the characteristics of the object for different layers.

4.6. Discussion

In order to compare the two techniques under their respective optimal configurations, the acquisition conditions were very different for the in-line phase contrast tomosynthesis versus conventional tomosynthesis. The experimental results therefore have limitations on the applicability. For example, the demonstrated performance of in-line phase contrast tomosynthesis was obtained under specific exposure conditions (120 kVp x-ray beam with filtration, a specific magnification factor, specific phantoms to accentuate certain features, etc.).

Although a biologically relevant chicken breast phantom was investigated in this study, the measurements may still suffer from several limitations. The chicken breast phantom was a laboratory-fabricated phantom and the material was not evenly cut, so the thickness of the chicken was not even. This unevenness of the structure may cause inhomogeneous areas on the images. Since the chicken was not frozen and was not compressed firmly, small movements caused by gravity during the measurements may result in artifacts and errors. Therefore, further investigations are needed with gold-standard phantoms to provide more comprehensive performance comparisons between in-line phase contrast tomosynthesis and conventional tomosynthesis imaging techniques.

The initial results demonstrate the feasibility of in-line phase contrast tomosynthesis to enhance image contrast noise ratios with comparable radiation doses. The high exposure levels used in this work resulted from the specific phantoms employed in the experiments. The first phantom employed in our study is a 5-layer bubble wrap embedded in 30-mm

acrylic plates. The imaging targets are the rims of each of the bubbles. The bubble rims present very low radiological contrast in the projections. Hence a high exposure (5322 mR) was used with the conventional tomosynthesis technique. As shown in Figure 10 (a) and (d), even with such a high exposure, the rims are just barely visible in the images acquired with the tomosynthesis technique. This being so, for a performance comparison, the experiment with the in-line phase contrast tomosynthesis technique employed a comparable exposure. In the similar low-contrast imaging task presented for the 60-mm thick chicken breast phantom, the imaging targets are the embedded fibrils and masses, which were extracted from an ACR mammography phantom. However, as discussed previously, the intrinsic radiological contrast between the targets and chicken breast is much lower than that between the targets and the wax plate in the ACR phantom. This makes it necessary to use a high-exposure in the conventional tomosynthesis technique. In the fish bone phantom studied, the fish bones were embedded in a 110-mm thick beeswax block, and the large size of this phantom resulted in a high-exposure employed for the conventional tomosynthesis technique. Relating the results of this work to breast imaging, we note that the intrinsic radiological contrast of breast tissues will be much higher than that for the targets in our bubble phantom and chicken breast phantom. Therefore, we expect that a much lower entrance exposure level can be used with the tomosynthesis and phase techniques for breast imaging. In fact, recently we compared images of a 4.5 cm thick contrast-detail phantom acquired on a phase imaging setting with images acquired on a commercial flat panel digital mammography unit. The phase contrast images were acquired at 120 kVp and 4.5 mAs, with a geometric magnification factor of 2.46. Conventional digital mammography images were acquired at 28 kVp, 54

mAs. For the same radiation dose, both the observer study and signal-to-noise ratio comparisons indicated large improvement by the phase retrieved image as compared to the clinical system. [21] The exact radiation dose comparisons will be quantified in a future study, which will calculate the absorbed dose values corresponding to the comparison methods instead of applying estimations through the entrance exposure values.

In addition, several remarks are due for the applicability of the PAD based phase retrieval method. As mentioned in Section 2.3, the most applicable selection of x-ray photon energy for PAD ranges from 60 keV to 500 keV. Experimentally, obtaining x-ray photons with energies from 60 keV to 120 keV implies that heavy filtration must be utilized to completely remove photons less than 60 keV with 120 kVp output. [15, 55] Thus, the exposure time is dramatically increased, due to very low x-ray photon flux when employing heavy prime beam filtration. Therefore, the goal of the prime beam filtration used in this research was to remove most of the x-ray photons under 30 keV, and to introduce the experimental exposure condition in order to approximately satisfy the application condition of the PAD retrieval method. Due to the use of polychromatic x-rays, it was necessary to approximate the values utilized in Equation (32) for the average wavelength λ and the Klein-Nishina total cross-section σ_{KN} as those corresponding to a 60.5 keV x-ray, which is the estimated average photon energy for a 120 kVp x-ray beam.

Also mentioned in Section 2.3, the x-ray attenuation by soft-tissue-like materials made up of low-Z ($Z < 10$) elements is dominated by incoherent x-ray scattering, due to the use

of high-energy x rays as described above. Thus the principle of phase-attenuation duality applies. For the components of high-Z elements, phase-attenuation duality (PAD) does not hold. As a result, the retrieved phase values of high-Z components include errors, but the retrieved phase values for the low-Z components are accurate, since the PAD equation is a differential equation and its solution is unique in its locality. Our previous experiment using a 60 keV synchrotron beam found that the presence of Aluminum (Z = 13) in a phantom results in an approximate 36% discrepancy in the reconstructed electron density for the aluminum component in the phantom. As detailed in Section 4.5.1, the effective atomic number Z_{eff} of fishbone is about 13, thus the same level of 36% difference from the theoretical phase values can be expected. Contrary to CT, tomosynthesis is essentially a limited angle tomography, which itself cannot provide exact reconstruction by its nature. Further investigation is needed on the quantitative aspects of phase retrieval-based tomosynthesis.

As for the effects of the different magnification factors in phase tomosynthesis versus conventional tomosynthesis, note that the phantom features in the comparisons are of 0.4 mm or larger in size, so they could all be resolved by the detector in both the conventional and phase imaging configurations, as long as sufficient contrast-noise ratios exist. Hence the magnification factor used is not the deciding factor, although larger magnification with phase imaging causes potential blurring from the focal-spot, while no such blur occurs with the conventional tomosynthesis configuration.

To address the effects of the detector performance on the comparison, note that the detector DQE decreases with increasing photon energy, since the quantum efficiency of a detector decreases with increasing photon energy, [84] as does the attenuation contrast between different tissue/materials. Consequently the use of the high-kVp beam is intrinsically disadvantageous to phase imaging in this comparison study. The phase contrast itself decreases with increasing photon energy as well. However, in order to reduce exposure times with the current-limiting microfocus tube while also allowing the use of the low kVp beam for conventional imaging, the high-kVp beam is necessary for phase imaging. In addition, high-kVp imaging is especially relevant for imaging thick body parts, due to the higher penetration ability. Our work in fact provides for the first time a study on the performance of high-kVp phase tomosynthesis. Despite the disadvantages with high-kVp imaging detailed above, however, this research demonstrated that high-energy in-line phase contrast imaging at a reduced radiation dose provides comparable image quality to low-energy conventional non-phase-contrast imaging. In addition, a significant contrast-noise-ratio enhancement with PAD phase retrieval as compared to conventional tomosynthesis was demonstrated.

4.7. Chapter Conclusion

In this research, the major objectives were to demonstrate a high-energy in-line phase contrast tomosynthesis imaging system and investigate the capabilities of edge enhancement, contrast improvement and noise suppression through employing the PAD method onto angular projection images.

The quantitative calculations of in-plane MTF and NPS successfully characterized the high-energy in-line phase contrast tomosynthesis system. The phantom studies demonstrated that this imaging prototype can successfully remove the structure overlapping in phantom projections, obtain delineated interfaces and achieve enhancement in contrast-to-noise ratios after applying the PAD-based phase retrieval to the angular projections. To our knowledge, this is the first time that the PAD-phase retrieval methods have been applied to tomosynthesis imaging.

Chapter 5. Prime Beam Optimizations toward Applications of PAD Phase Retrieval

5.1 Introduction

In characterization studies of the high-energy in-line phase contrast tomosynthesis imaging method detailed in Chapter 4, the angular projections of the objects were acquired under in-line phase contrast radiography mode with 120 kVp prime beam exposure filtered by 2.5 mm Al. The projections were then processed by phase-attenuation duality (PAD) phase retrieval before tomosynthesis reconstruction. Comparison of the resulting in-plane images of the phantom with conventional tomosynthesis images indicated that the contrast along boundaries of both microcalcifications and mass targets within the phantoms were increased. However, the PAD phase retrieval method employed in the study suffered an inaccuracy due to the energy composition of the prime beam x-ray, which is required to be higher than 60 keV. [13, 58] Aiming to solving this issue, an x-ray prime beam filtration method combining different common-use filters with different thicknesses will be proposed and investigated in this chapter to obtain an optimized x-ray composition/spectrum.

The comparison methods employed to evaluate the effects of the prime x-ray beam composition were the modulation transfer function (MTF), the noise power spectrum (NPS) and the detective quantum efficiency (DQE) of a high-energy in-line phase contrast radiography prototype operated under different commonly-used prime beam filtrations.

5.2 Prototype Specifications

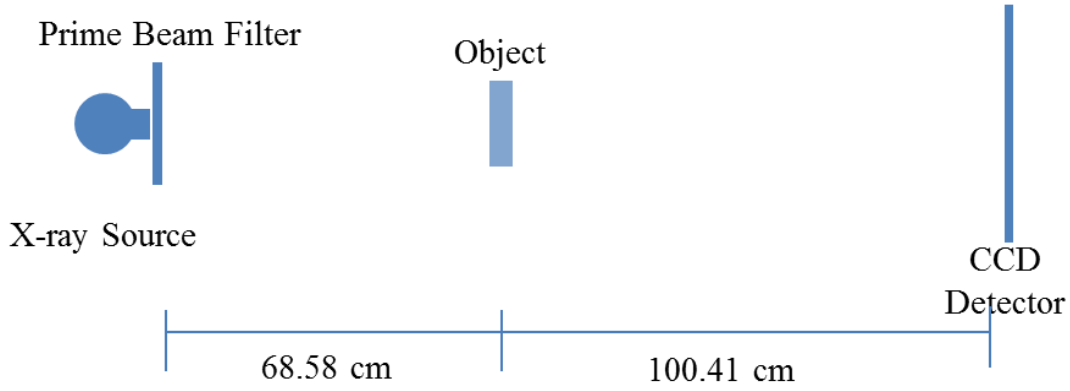

Figure 35: The experimental prototype of the high-energy in-line phase contrast system.

This research employed a microfocus x-ray source (Model L8121-03, Hamamatsu Photonics), and the x-ray tube was operated at a voltage of 100, 110 or 120 kVp and a tube current of 500 μA. The detector acquiring the projections was a CCD detector coupled with a CsI:Tl structured scintillator (66 mm×66 mm, Imagestar 9000, Photonic Science Ltd.), providing 21.6 μm of sampling pixel pitch. The geometry of the experimental prototype system is shown in Figure 35. The objects were mounted on a stage placed 68.58 cm away from the x-ray source, and the source-to-image distance (SID) value was 169.0 cm. The parameters were selected to deliver optimal phase shift effects according to the principles of in-line phase contrast imaging, as well as to reduce the loss of x-ray photons during propagation through the air gap. [53, 57, 61]

The experimental arrangement of the different combinations of x-ray tube settings and filtrations are listed in Tables 4 and 5. All the measurements were conducted under a unified averaged glandular dose value of 1.295 mGy. Corresponding exposure times of each mode will be detailed in the following section.

Table 4. X-ray tube settings and beam filtration for the investigation of different kVp

Tube Voltage (kVp)	Tube Current (μA)	Prime Beam Filtration
100 110 120	500	2.5 mm Al

Table 5. X-ray tube setting and beam filtrations for the investigation of different filter

Tube Voltage (kVp)	Tube Current (μA)	Prime Beam Filtration
120	500	None 0.01 mm Mo 0.03 mm Mo 0.06 mm Mo 0.025 mm Rh 0.05 mm Rh 2.5 mm Al Combo*

* Combo filter was made of 2.3 mm Cu, 0.8 mm Pb and 1.0 mm Al

5.3 Determination of the Exposure Time

The exposure time (T) of each mode was determined by the object entrance exposure (X_{ESE}) and the entrance exposure rate (R_X):

$$T = \frac{X_{ESE}}{R_X} \tag{39}$$

where the entrance exposure rate was directly measured by a dose meter with an ion chamber, and the object entrance exposure (X_{ESE}) values can be determined by the ratio of the average glandular dose (D_g) and the normalized average glandular dose coefficient (D_{gN}) as follows:

$$X_{ESE} = \frac{D_g}{D_{gN}} \tag{40}$$

where D_g has been selected as a unified dose value of 1.295 mGy, and D_{gN} was determined by x-ray spectrum of each filtration and tube setting combination and assuming an object equivalent to a 5 cm thick compressed human breast with 50 % glandular and 50 % adipose. [21, 85-88]

Therefore, the exposure times, along with other parameters, for each mode are shown in Tables 6 and 7, corresponding to the investigations for different kVp values and different filtration values, respectively.

Table 6. Experiment parameters for the investigation of different kVps

Tube Voltage (kVp)	Tube Current (μA)	Prime Beam Filtration (mm)	D_g (mGy)	D_{gN} (mrad/R)	X_{ESE} (mR)	R_X (mR/s)	Exposure Time(s)
100				5.28	245.27	15.77	15.56
110	500	Al 2.5	1.295	5.62	230.43	18.76	12.28
120				6.52	198.62	22.02	9.02

Table 7. Experiment parameters for the investigation of different filters

Tube Voltage (kVp)	Tube Current (μA)	Prime Beam Filtration (mm)	D_g (mGy)	D_{gN} (mrad/R)	X_{ESE} (mR)	R_X (mR/s)	Exposure Time(s)
120	500	None	1.295	4.88	265.39	84.78	3.13
		Mo 0.01		5.27	245.73	51.50	4.77
		Mo 0.03		5.97	216.92	31.57	6.87
		Mo 0.06		6.63	195.21	19.51	10.01
		Rh 0.025		6.07	213.34	31.55	6.76
		Rh 0.05		6.70	193.28	19.52	9.90
		Combo*		8.25	156.97	0.67	234.16

* Combo filter was made of 2.3 mm Cu, 0.8 mm Pb and 1.0 mm Al

5.4 Objective Characterizations

5.4.1 MTF Measurements and Calculation

Experimental determination of the MTF for the high-energy in-line phase contrast prototype was performed by the presampling MTF method with a slanted edge. [67, 69, 74, 75] The sharp edge was an acrylic edge and was mounted at the center of the stage and well aligned with the x-ray source and the detector. The projection of the edge was acquired for the total exposure time detailed in Section 5.3 Tables 6 and 7 for the corresponding mode. The image shown in Figure 36 was used to illustrate the edge as an example for calculating the MTF. Then, the corresponding edge spread function (ESF), illustrated as an example in Figure 37, was calculated through averaging the horizontal profile intensities along the maximum-changing line. The 1D ESF curve was smoothed by interpolation. Consequently, the 1D line spread function (LSF) can be obtained using the differential relationship between the LSF and ESF, as detailed by Equation (34) in Section 4.3.

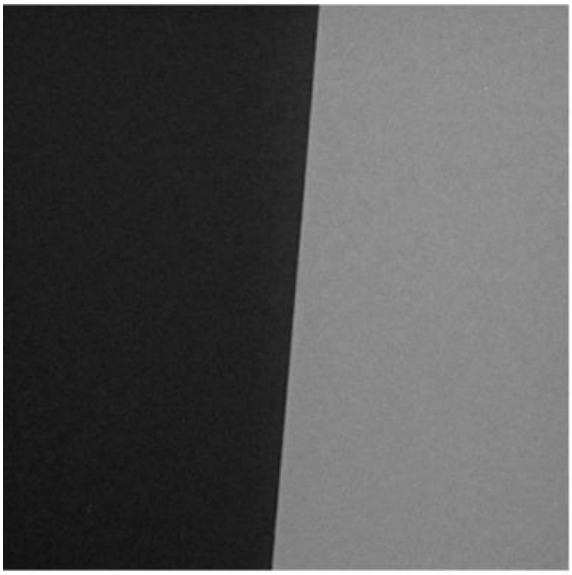

Figure 36: The high-energy in-line phase contrast projection image of the acrylic edge phantom.

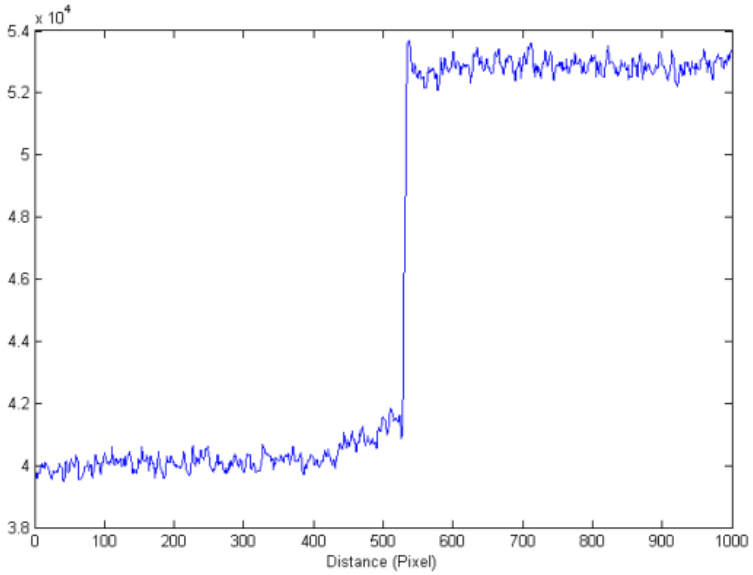

Figure 37: ESF, the average horizontal intensity profile plot of the edge.

Finally, the MTF curve can be calculated by the Fourier transform of the LSF, as detailed by Equations (33) and (34) in Section 4.3.

5.4.2 NPS Measurements and Calculation

In the NPS calculation of the high-energy in-line phase-contrast prototype, the images for each experimental settings were acquired under a total exposure time detailed in Section 5.3 Table 6 and Table 7 for the correspondent mode. The 11 projections of each mode were then used to calculate the noise-only images, the difference between two projections, as follows:

$$\text{Noise Image}_n = I_n - I_{n+1} \quad (n = 1, 2, \ldots \ldots 11). \tag{35}$$

As defined in the literature, the 2D NPS is determined by [12, 16]:

$$\text{NPS}(f_x, f_y) = \frac{\Delta x \cdot \Delta y}{N_x \cdot N_y} \langle |\text{FT}\{\text{Noise Image}_n\}|_m^2 \rangle \quad (m = 1,2, \ldots 10), \tag{41}$$

where x and y denote the directions indicated in Figure 14 in Section 4.3.2, Δx and Δy are the pixel dimensions in corresponding dimensions, and $N_x \times N_y$ is the number of pixels.

5.4.3 DQE Measurement

Detective quantum efficiency (DQE) is widely used for quantitatively evaluating the performance of x-ray imaging systems. It integrates the concept of signal-to-noise ratio (SNR), noise power spectrum (NPS) and spatial resolution (MTF). Therefore it has become a standard to describe the performance of an x-ray imaging system in research environments.

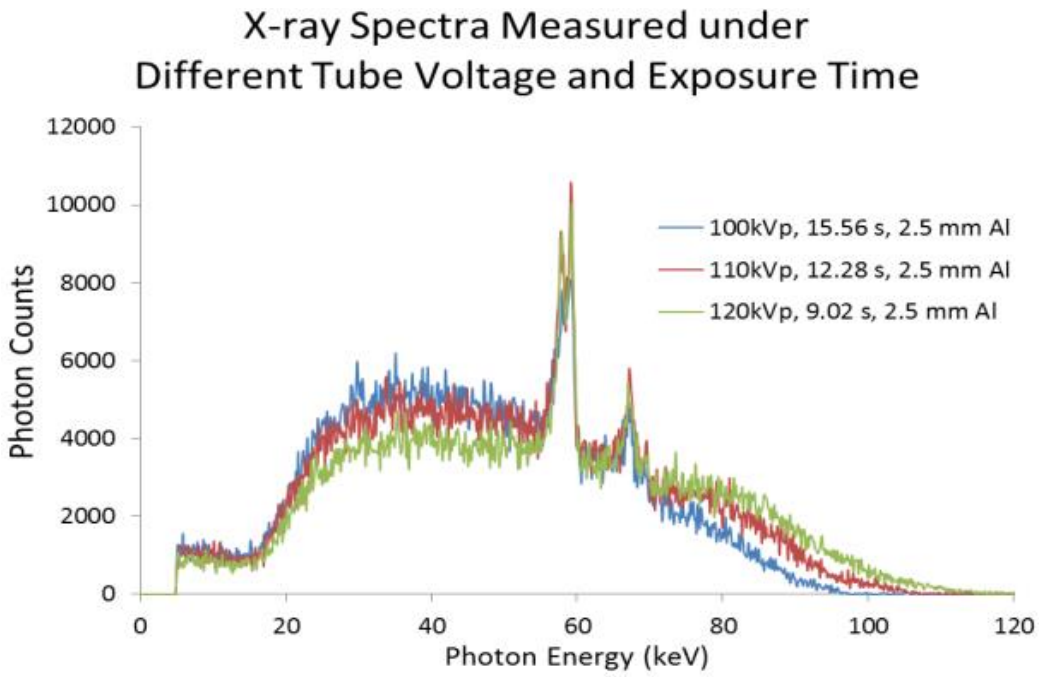

Figure 38: Spectra measured under 2.5 mm Al prime beam filtration, different tube voltage and corresponding exposure time.

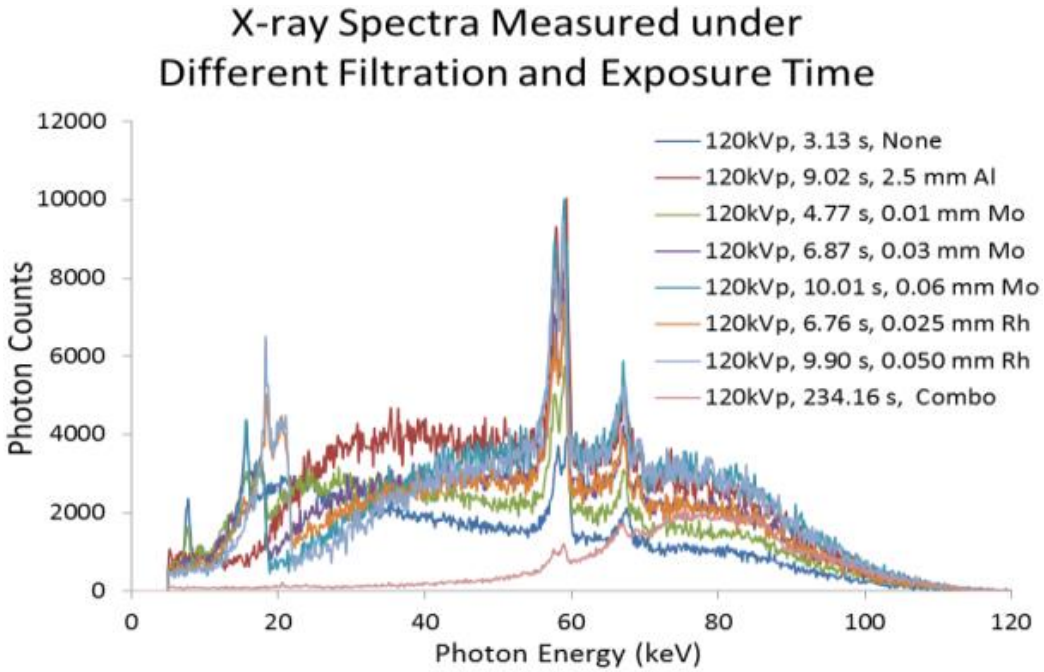

Figure 39: Spectra measured under 120 kVp tube voltage, different prime beam filtration and corresponding exposure time.

In conceptual terms, the DQE can be described as the square of the SNR transfer of an imaging system from the signal output to the input: [12-16]

$$\mathrm{DQE} = \frac{\mathrm{SNR}_{\mathrm{OUT}}^2}{\mathrm{SNR}_{\mathrm{IN}}^2}. \tag{42}$$

$\mathrm{SNR}_{\mathrm{OUT}}^2$ can be defined as

$$\mathrm{SNR}_{\mathrm{OUT}}^2 = \frac{\mathrm{MTF}(f)^2}{\mathrm{NPS}(f)}, \tag{43}$$

in which $\mathrm{MTF}(f)^2$ is the modulation transfer function. $\mathrm{SNR}_{\mathrm{IN}}$ equals $\sqrt{\mathrm{N}}$, the square root of the incident number of quanta per unit area according to the Poisson distribution of x-ray photons. Thus, the equation fully describing the DQE is as follows [67, 69, 72, 74, 75]

$$\mathrm{DQE}(f) = \frac{\mathrm{LAS}^2 \cdot \mathrm{MTF}(f)^2}{\mathrm{NPS}(f) \cdot N}, \tag{44}$$

where LAS stands for the large area signal, which is the mean output pixel value; MTF(*f*) and NPS(*f*) are functions of the spatial frequency; and *N* is the number of photons per unit area, which is determined by:

$$N = X_{\mathrm{ESE}} \cdot \frac{\Phi}{X}, \tag{45}$$

which involves multiplication of the radiation exposure X_{ESE} by the photon fluence per unit exposure $\frac{\Phi}{X}$. X_{ESE} is determined through directly measuring the x-ray exposure under the different modes detailed in Section 7.2, and $\frac{\Phi}{X}$ is calculated from the x-ray spectra shown in Figure 38 and 39. [67, 75] The number of photons per unit area, *N*, and the percentage of x-ray photons with energy > 60 keV can be determined from the measured spectra, and the results are shown in Tables 8 and 9.

Table 8. Number of photons per unit area and percentages of the composition of x-ray energy in different tube voltage modes

Prime Beam Filtration	Tube Voltage (kVp)	X_{ESE} (mR)	Exposure Time(s)	N (mm^{-2})	% of Photon w/ Energy >60 keV
2.5 mm Al	100	245.39	15.56	1.70×10^{7}	24.09
	110	230.61	12.28	1.72×10^{7}	30.66
	120	198.53	9.02	1.76×10^{7}	36.93

Table 9. Number of photons per unit area and percentages of the composition of x-ray energy in different filtration modes

Tube Voltage (kVp)	Prime Beam Filtration	X_{ESE} (mR)	Exposure Time(s)	N (mm^{-2})	% of Photon w/ Energy >60 keV
120	None	265.42	3.13	1.27×10^{7}	26.94
	0.01 mm Mo	245.54	4.77	1.38×10^{7}	30.66
	0.03 mm Mo	216.82	6.88	1.50×10^{7}	36.58
	0.06 mm Mo	195.21	10.01	1.66×10^{7}	43.85
	0.025 mm Rh	213.19	6.76	1.49×10^{7}	36.55
	0.050 mm Rh	193.20	9.91	1.63×10^{7}	43.58
	2.5 mm Al	198.53	9.03	1.76×10^{7}	36.93
	Combo*	156.89	234.28	2.04×10^{7}	82.24

* Combo filter was made of 2.3 mm Cu, 0.8 mm Pb and 1.0 mm Al

5.5 Low-energy Removal Filter

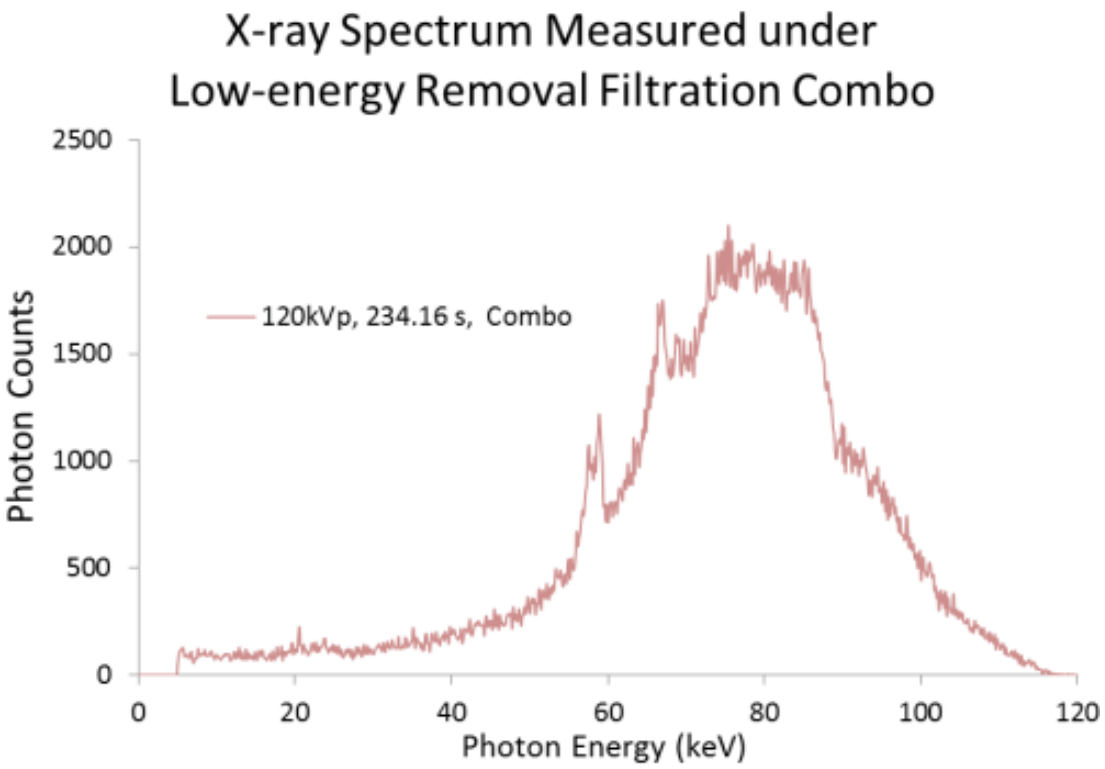

Figure 40: Spectrum of the low-energy removal filtration combo measured under 120 kVp tube voltage and 234.16 s. (Combo filter was made of 2.3 mm Cu, 0.8 mm Pb and 1.0 mm Al)

In this research, the low-energy removal filter combination made of 2.3 mm Cu, 0.8 mm Pb and 1.0 mm Al was employed. The spectrum of the prime beam after filtration is presented in Figure 40, and the percentage of x-ray photons with energy >60 keV is shown in Table 9. The 82.24% photons with energy higher than 60 keV indicated a dramatic increase as compared to the other filtrations.

5.6 Results and Discussion

5.6.1 MTF Curves

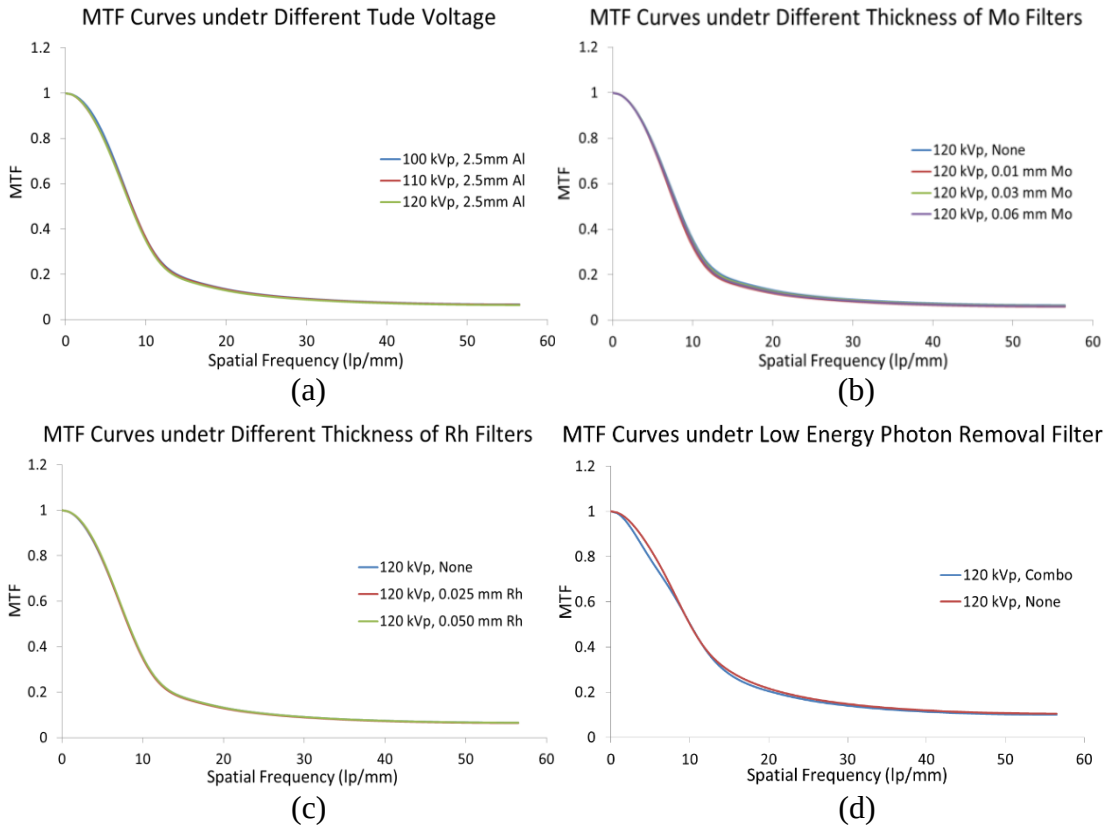

Figure 41: MTF curves measured under the 1.295 mGy average glandular doses: (a) MTFs of different tube voltages, (b) MTFs of Mo filters with different thicknesses, (c) MTFs of Rh filters with different thicknesses, and (d) MTF of the low energy removal filter compared with MTF without filtration.

The MTF curves measured and calculated by each of the modes are provided in Figure 41. The comparisons were conducted based on different tube voltages and different thicknesses of the filtration materials. The similarity between the curves in Figure 41 indicates the ability to maintain the frequency response of the system with increasing tube voltage and filtration thickness.

5.6.2 NPS Curves

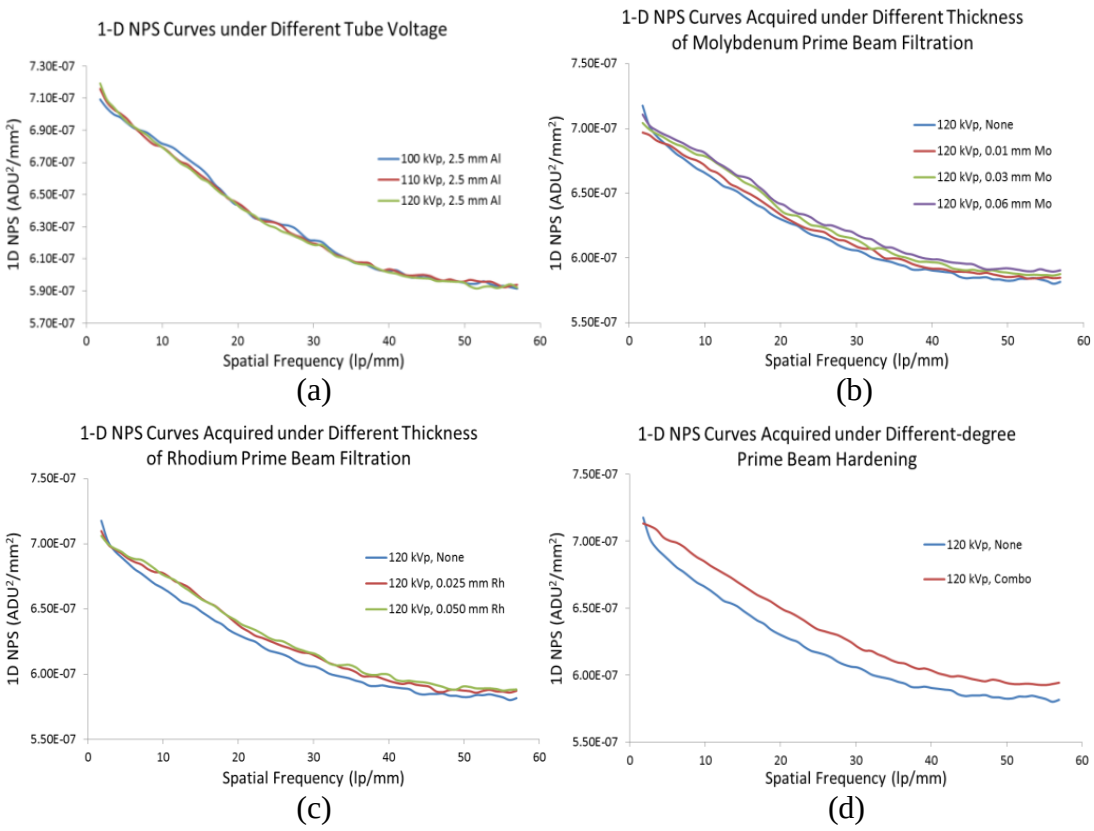

Figure 42: NPS curves measured under the 1.295 mGy average glandular doses: (a) MTFs of different tube voltages, (b) MTFs of Mo filters with different thicknesses, (c) MTFs of Rh filters with different thicknesses, and (d) MTF of low energy removal filter compared with MTF without filtration.

The NPS curves measured and calculated by each of the modes are provided in Figure 42. Based on the same logic used for the MTF curves, the comparisons were also conducted based on different tube voltages and different thicknesses of the filtration materials. The similarity between the curves in Figure 42(a) indicates the ability to maintain the noise power response of the system with increasing tube voltage. The divergent behaviors occurring in Figure 42(b), (c) and (d) indicate that the NPS value increases through hardening the prime beam filtration as well as thickening the filtration for the same filter material.

5.6.3 DQE Curves

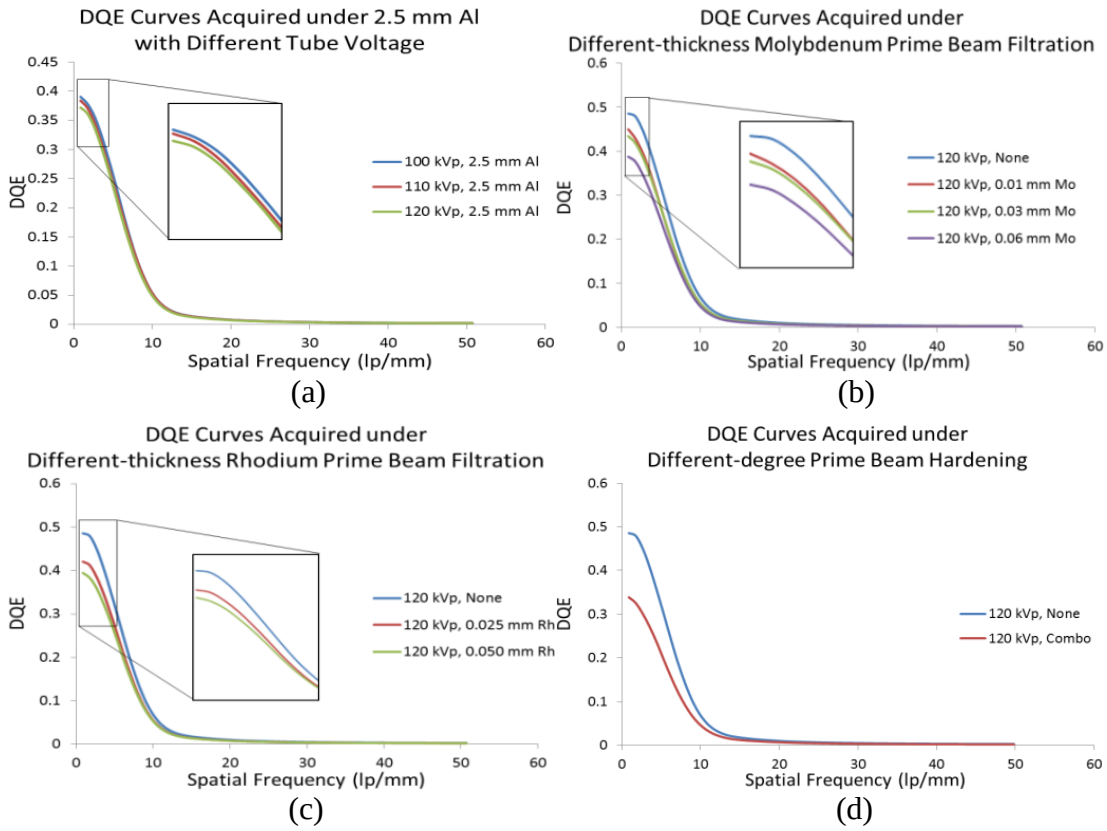

Figure 43: DQE curves measured under an average glandular dose of 1.295 mGy with: (a) different tube voltages, (b) Mo filters with different thicknesses, (c) Rh filters with different thicknesses, and (d) low energy removal filter compared with DQE without filtration.

The DQE curves calculated with the previous results for each mode are provided in Figure 43. The comparisons were also conducted based on different tube voltages and different thicknesses of the filtration materials. The divergent behaviors occurring at spatial frequencies < 10 lp/mm indicate that the DQE value decreases with increased tube voltage as well as increased filtration for the same filter material. The behaviors of the DQE curves acquired with a unified radiation dose obeyed the relationship among the MTF,

NPS, LAS and N regulated by Equations (42)-(44). In other words, the unchanged MTFs, increased NPS, increased number of photons per unit area (N) and relatively unchanged LAS in different modes influenced the resultant DQE behaviors. The LASs calculated in different filtration modes are shown in Table 10. The results demonstrate that the low-energy-removal filter decreases the overall DQE, but this filtration combination successfully removed a large percentage of the x-ray photons with energies lower than 60 keV. This helped to optimize the application conditions of the phase-attenuation duality phase retrieval method by minimizing the error introduced by large amounts of low-energy photons.

Table 10. Large area signal (LAS) calculated for different filtration modes

Filter Materials	Al			None	Mo			Rh		Combo*
Tube Voltage (kVp)	100	110	120							
Filter Materials	Al			-	Mo			Rh		-
Thickness (mm)	2.5			-	0.01	0.03	0.06	0.025	0.050	-
LAS	5.4	5.4	5.4	5.3	5.2	5.3	5.3	5.3	5.3	5.5

* Combo filter was made of 2.3 mm Cu, 0.8 mm Pb and 1.0 mm Al

In addition, by observing the percentages of high-energy photons from Table 8 and Table 9, we found that higher numbers of high-energy photons in the exposure may result in lower DQE values. However, studies of the effects on the DQE by the energy composition of x-ray exposures under a unified radiation dose are beyond the scope of this research.

5.7 Chapter Conclusion

In this chapter, the effects of the prime x-ray beam compositions on the modulation transfer function, the noise power spectrum and the detective quantum efficiency of a high-energy in-line phase contrast prototype delivering unified radiation dose have been experimentally evaluated. The results indicate that under a unified radiation dose, which was 1.295 mGy in this study, the MTF was preserved under different exposure conditions, since it only describes the spatial resolution response of an imaging system regardless how much radiation dose is delivered. In addition, the NPS increases with increased beam hardening and the overall DQE decreases with an increasing number of high-energy x-ray photons in the exposure under the same filter material mode.

The low-energy removal filter first demonstrated the ability in removing low energy photons, and the MTF and DQE measured under the combo filter indicated that the low-energy-removal filter was able to perform as the prime beam filtration with adequate efficiency and spatial resolution response under a low-radiation-dose condition. However, in this study, as the filters not only block low-energy x-ray photons but also filter a considerable amount of high-energy photons, the resultant photon rate of the exposure was extremely low compared with the exposure under no filtration or lighter filtration with the Al, Mo and Rh filters. This was due to the limitation of the micro focus spot of the solid-target x-ray tube, and may result in extremely long imaging acquisition times in phantom or tissue studies. [89] Therefore, these issues have to be solved in the future before phase sensitive tomosynthesis can be translated to clinical applications.

Chapter 6. Using Copolymer-shell Microbubble as Contrast Agent for High-energy X-ray In-line Phase Contrast Imaging: A Comparison Study

Since the high-energy in-line phase contrast tomosynthesis is a technique of the combination high-energy in-line phase contrast and digital tomosynthesis, the angular projections acquired with the high-energy in-line phase contrast technique perform an important part in the determination of the imaging quality of the whole technique while the digital tomosynthesis provides the quasi-3D reconstruction. Thus, preliminary demonstrations performed with the high-energy in-line phase contrast projection imaging technique is convincing before processing with tomosynthesis reconstructions and is time saving for investigating new imaging approaches.

In this chapter, the preliminary study investigating polymer-shell microbubbles as phase contrast agent for high-energy in-line phase contrast tomosynthesis was done by the projection imaging method.

6.1 Introduction

X-ray mammography, a 2-D projection imaging technique, has been widely-used as a method for breast cancer screening, but the imaging contrast of the current mammography technique relies on the small attenuation differences between normal tissues and tumors. When x-rays pass through an object, they also undergo phase shifts. The changes of the x-ray wave field can be expressed by the complex x-ray transmittance, recalling Equation (26):

$$T(x,y) = A(x,y)e^{-i\phi(x,y)} \tag{26}$$

where $A(x,y) = e^{-\int \frac{\mu(x,y,z)}{2} \mathrm{d}z}$ and $\phi(x,y) = -\frac{2\pi}{\lambda} \int \delta(x,y,z) \mathrm{d}z$, in which $A(\mathrm{x},\mathrm{y})$ is amplitude, $\phi(x,y)$ is phase shift, μ denotes the attenuation coefficient and δ denotes refractive index decrement, as detailed in Section 2.2. Several x-ray imaging techniques based on phase contrast have been investigated. [10-12] In-line phase contrast x-ray imaging is one of these methods. The clinical feasibility of 2-D phase contrast mammography based on the in-line principle has been widely reported, and its potential to improve signal-to-noise ratio (SNR) and reduce exposure time as well as radiation dose has been demonstrated in phantom studies. [21]

In order to further improve the imaging quality and maximize the benefits of the phase contrast mechanism, concepts of tissue engineering were proposed to introduce the application of microbubbles into phase contrast related imaging techniques. Microbubbles have been widely used as an ultrasonic contrast agent. Based on the morphology of microbubbles, they can be also considered as a population of lens scattering x-ray photons providing a sequence of multi-refraction. Considering the interaction between high-energy x-ray photons and matter, Compton scattering dominates when the microbubbles are made of materials with low atomic numbers, Z < 10. The phase shifts due to the Compton scatterings among different types of scattering sources/structures are characterized by the refractive index decrement, $\delta_{\mathrm{Compton}}$, which can be described by:

$$\delta_{\mathrm{Compton}} = \frac{\lambda^2 r_{\mathrm{e}}}{2\pi} \cdot \frac{N_{\mathrm{A}} \rho}{A}, \tag{46}$$

where λ is the wavelength, r_{e}=2.8179402894×10^{-15} m is the classical electron radius, N_{A} is Avogadro's number ($\approx 6.022 \times 10^{23}$ mol^{-1}), ρ is the mass density, A is the atomic

mass ([g/mole]), and $\frac{N_A \rho}{A}$ denotes the number of electrons per unit volume. [52] Therefore, based on the unique mass density and atomic mass provided by the components of microbubbles, distributions of microbubbles have the potential to modify the local interaction between x-ray photons and the sample, and thus introduce additional phase shifts near the location of the microbubbles by changing the regional electron density within a finite space. This phase contrast information can be combined with the intrinsic attenuation contrast information to improve the imaging quality by employing phase retrieval techniques.

In the literature, microbubbles as an x-ray phase contrast imaging contrast agent have been demonstrated by using analyzer-based [22] and propagation-based [23] synchrotron x-ray phase contrast, synchrotron free space propagation phase contrast methods [24-25] and the Talbot-Lau interferometry phase contrast method. [26-27] 3D computed tomography imaging of microbubbles was also demonstrated by Tang *et al*. in 2013 through a differential phase contrast system accompanied with object rotation. [29] A recent study done by Millard, *et al*. indicated that microbubble contrast agents provide the potential to perform dynamic imaging with analyzer-based synchrotron x-ray phase contrast. [28] However, in previous studies, the radiation dose delivered to tissues/samples has not been regulated, the impacts of the microbubble shell materials toward imaging contrast has not been discussed, and the experimental demonstrations have not been compared with conventional x-ray imaging methods.

In this study, we experimentally demonstrate an imaging method employing a high-energy in-line phase contrast system with the administration of microbubbles as an x-ray scattering agent under a limited radiation dose to the tissue. Considering the clinical conditions under which the microbubbles may be distributed around the tumor via capillary blood supplies and self-targeting mechanisms, the tumor areas with microbubble distributions may have imaging contrast with non-microbubble distributed regions due to the attenuation contrast and phase contrast information. Therefore, this imaging contrast can be estimated by calculating the contrast-to-noise ratio (CNR) when considering the water-only images as the non-microbubble distributed area, e.g. the pure backgrounds. For comparison studies, the tissue simulating phantom injected with the same level of microbubble concentrations will be imaged by low-energy contact-mode conventional projections.

6.2 Methods and Materials

6.2.1. Experimental Configurations

In this study, a micro focus x-ray source (Model L8121-03, Hamamatsu Photonics) able to generate x-ray photons ranging from 40 kVp to 150 kVp with an adjustable tube current was employed. The nominal focal spot sizes of 7 μm, 20 μm, and 50 μm can be selected and/or determined by the desired output power. The high-energy in-line phase contrast images were acquired with 120 kVp tube voltage, 500 μA tube current. As a comparison, the low-energy contact-mode imaging prototype was operated with 40 kVp tube voltage and 500 μA tube current. A prime beam filter made of 2.5 mm Al was utilized to harden the prime beam for both phase contrast mode and contact mode. [89] The image detection

mechanism was a CCD detector coupled with a CsI:Tl scintillator (66 mm×66 mm, Imagestar 9000, Photonic Science Ltd.), providing 21.6 μm of sampling pixel pitch.

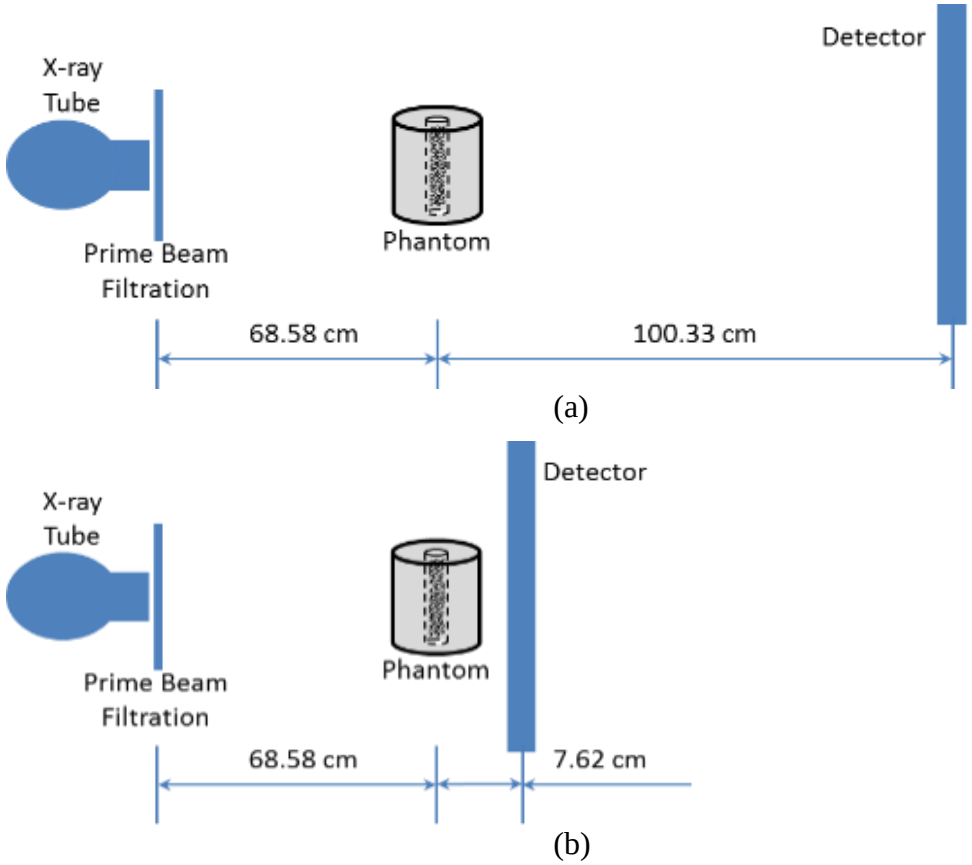

Figure 44: (a) The configuration of the high-energy in-line phase contrast imaging prototype, and (b) the configuration of low-energy contact-mode imaging prototype.

As shown in Figure 44, the test object was placed on a stage with a 68.58 cm source-to-object distance (SOD) for both imaging prototypes. In the high-energy in-line phase contrast imaging prototype shown in Figure 44(a), a source-to-image distance (SID) value of 168.91 cm was selected to deliver optimal phase shift effects according to the principles of in-line phase contrast imaging, as well as to reduce the loss of x-ray photons during propagation through the air gap. [53, 57, 61] For comparison purposes, the low-energy contact-mode imaging experiments were conducted with 76.20 cm SID as shown in Figure 44(b). The measurements were conducted under an average glandular dose of

2.590 mGy, which was calculated based on a 50/50 breast tissue composition i.e. that this is the tissue composition value used by research/clinical environments to simulate the average breast and that it stands for 50% glandular and 50% adipose (fatty) material. This dose regulation was also used to determine the exposure time of each imaging mode. The resultant high-energy in-line phase contrast images were processed by the phase-attenuation duality (PAD) retrieval method to optimize the imaging quality for phase contrast images. [21, 53, 57, 61, 89]

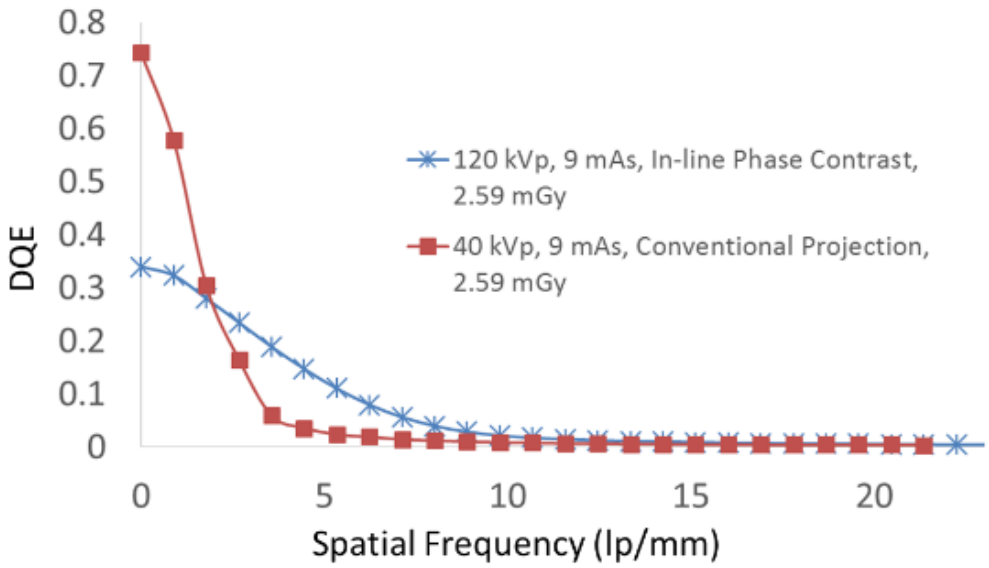

Figure 45: DQE comparison curves measured for the low-energy conventional projection method and the high-energy in-line phase contrast method.

Since the two imaging methods utilized in this study were operated under different x-ray tube voltages, the x-ray photons comprised of different energy compositions. Thus, the detective quantum efficiencies (DQE) were quantitatively measured by following the methods detailed in [16] and shown in Figure 45, in which the $DQE(0)$ of the low-energy conventional projection method and the high-energy in-line phase contrast were 0.743 and 0.340, respectively.

6.2.2 Phantom Design

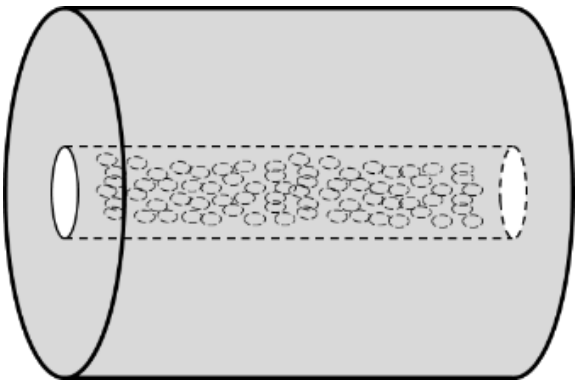

Figure 46: The schematic of the phantom simulating a 40 mm thick compressed breast.

As demonstrated in Figure 46, a 40 mm diameter acrylic rod was employed to simulate a 4 cm breast tissue. A 4 mm diameter hole was drilled along the central line of the acrylic rod to construct a cylindrical cavity allowing the injection of microbubble suspensions with different concentrations.

The microbubbles employed in this study were copolymer-shell microspheres (Expancel 461 DU 20 by AkzoNobel, Sweden) infilled with isobutene (C_4H_{10}) gas. The copolymer shell was made of $(C_5H_8O_2 \cdot C_3H_3N \cdot C_2H_2Cl_2)_n$ (poly acrylonitrile-co-vinylidene chloride-co-methyl, CAS No.: 25214-39-5). The microbubble diameters range from 6 μm to 9 μm. Before administration, 5 cm^3 of Expancel microspheres were suspended into 20 mL water at room temperature to obtain an original suspension with 20% volume concentration. The 20% suspension was further dissolved by adding water to acquire different relative concentrations. The volume concentrations administrated in this research were 5.0%, 2.0%, 1.0%, 0.5 %, 0.2 %, 0.1 % and 0 % (the water only control study).

6.2.3. Determination of the Exposure Time

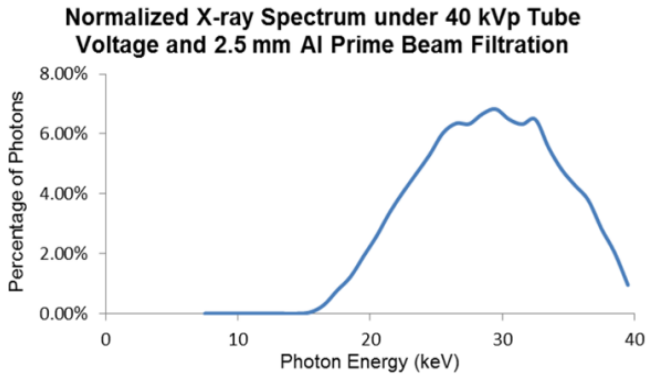

(a)

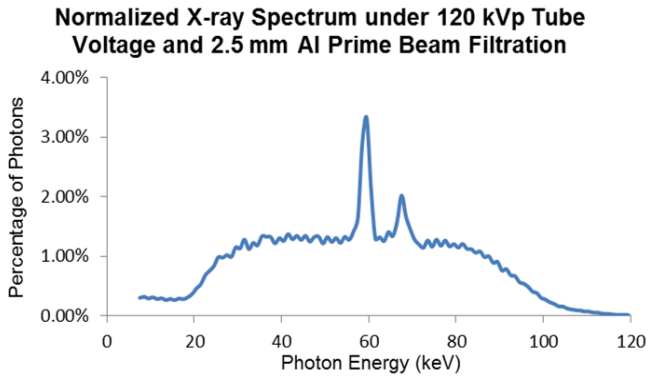

(b)

Figure 47: Normalized x-ray source output spectrum obtained under (a) 40 kVp and (b) 120 kVp. A 2.5 mm Al prime beam filter was applied for both tube voltage settings.

In this study, the average glandular dose has been selected as a unified value for both high-energy in-line phase contrast imaging mode and low-energy contact mode. The dose calculation was based on the normalized x-ray output spectra for both imaging modes shown in Figure 47. The exposure time, *T*, of each imaging mode was determined by following the same logic detailed in Section 5.3. The resultant exposure time for each mode is shown in Table 11, corresponding to the investigations under the two different tube voltages.

Table 11. Experiment parameters for the investigation of different kVp.

Tube Voltage (kVp)	Tube Current (μA)	Prime Beam Filtration	D_g (mGy)	D_{gN} (mrad/R)	X_{ESE} (mR)	R_X (mR/s)	Exposure Time(s)
40	500	2.5 mm Al	2.590	5.88	440.48	2.13	206.80
120				5.79	447.32	24.80	18.04

6.3 Results

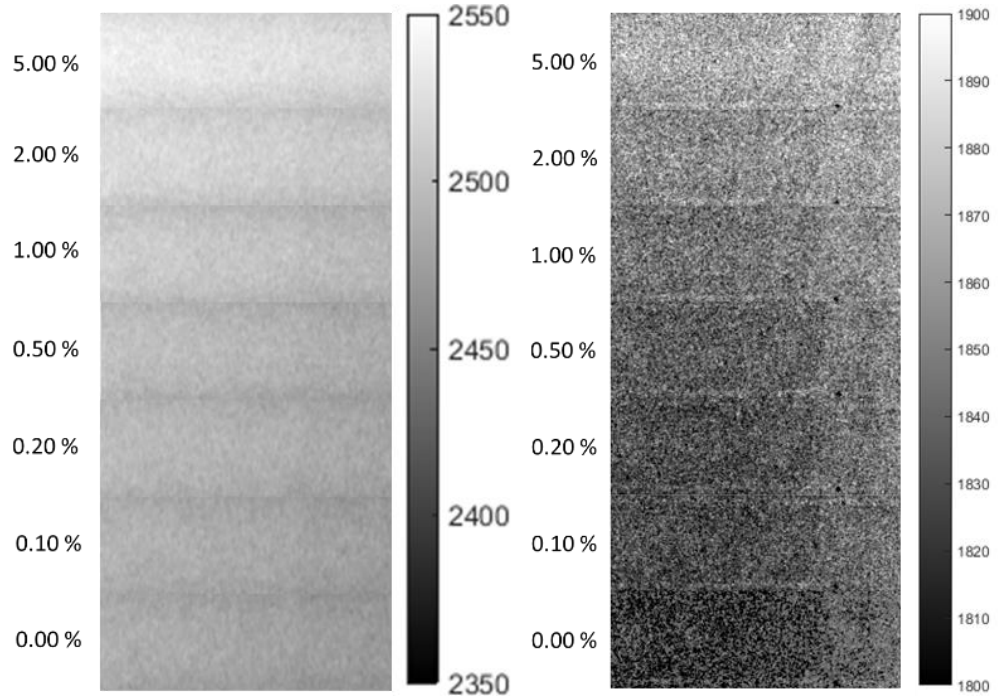

(a) (b)

Figure 48: (a) Low-energy conventional projection images, and (b) high-energy in–line phase contrast images of the regions infilled with different concentrations of microbubble suspensions.

Figure 48 presents the images of the phantom areas injected with microbubble suspensions of different concentrations (including the water-only area) acquired by low-energy conventional projections and PAD retrieved high-energy in-line phase contrast projections. The measured area intensities, noise levels and calculated CNRs

corresponding with each microbubble concentration and imaging method combination are listed in Tables 12 and 13.

The images acquired using both imaging methods demonstrate gradual intensity changes from low to high microbubble concentration. The PAD retrieved high-energy in-line phase contrast images in Figure 48 (b) displayed obvious contrast between the water-only image and the microbubble suspension images.

Table 12. I_S, σ_S, and CNR values of the low-energy contact-mode images.

Concentration (V/V)	Signal (I_S)	σ_S	CNR
5.0%	2529.30	0.28	169.42
2.0%	2514.90	0.43	120.44
1.0%	2504.33	0.35	84.44
0.5%	2493.87	0.37	48.86
0.2%	2489.63	0.29	34.42
0.1%	2483.20	0.41	12.53
0.0%	2479.52	0.29	(0)

* Noise level of water-only image is considered as the pure background noise

Table 13. I_S, σ_S, and CNR values of the high-energy in-line phase contrast images.

Concentration (V/V)	Signal (I_S)	σ_S	CNR
5.0%	1886.56	0.45	85.27
2.0%	1881.09	0.52	68.69
1.0%	1876.16	0.49	53.74
0.5%	1871.95	0.43	40.96
0.2%	1868.79	0.39	31.37
0.1%	1864.62	0.41	18.73
0.0%	1858.44	0.33	(0)

* Noise level of water-only image is considered as the pure background noise

By calculating the signal intensities for the images and considering the water-only images as the background for each imaging method, the contrast-to-noise ratios of the microbubble images were determined and plotted as a function of microbubble volume concentration. The resultant curves in Figure 49 illustrate that the microbubble distributions provide the ability to improve the area CNR. In addition, the overall CNRs of microbubble concentrations imaged by the low-energy conventional projections are better than those acquired by PAD retrieved high-energy in-line phase contrast. However, for the low microbubble concentrations (0.1%, 0.2% and 0.5%), the CNR curves of both imaging methods are similar. Finally, the CNR values of both imaging methods exhibit an increasing trend as the microbubble suspensions become denser.

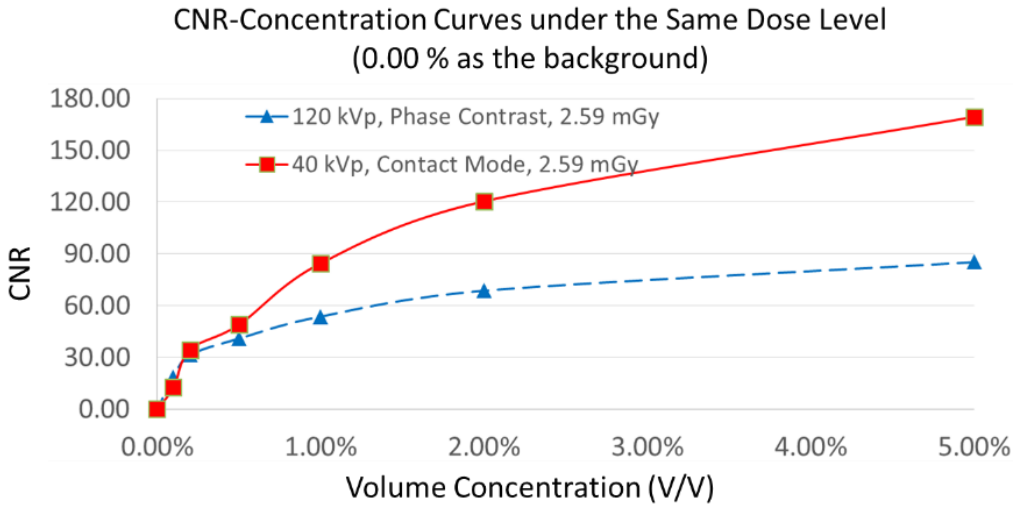

Figure 49: Comparison of CNR to volume concentration curves between low-energy conventional contact-mode method and high-energy in-line phase contrast under a same dose delivery.

6.4 Discussion

The resultant curves indicate that the CNRs of the images acquired in conventional low-energy mode are up to 1.99 times that of the high-energy in-line phase contrast images. This may mainly be due to the system properties. As detailed in Section II, the $DQE(0)$ for the low-energy contact mode value was 2.2 times higher than that of the high-energy in-line phase contrast mode. Thus, for approximately the same entrance exposure level, the difference between the signal intensity and the background was higher in the conventional contact mode than the phase contrast mode by a factor of 2.2.

In addition, the mass densities of the copolymer material, gas infill material and water are 1.6 g/cm^3, 2.51×10^{-3} g/cm^3 and 1.00 g/cm^3, respectively. When estimating the absorption attenuation coefficients (μ) by multiplying mass densities (ρ) with mass attenuation coefficients (μ/ρ), the absorption attenuation coefficient curves as functions of the x-ray energy are shown in Figure 50. Considering the copolymer shell and the gas infill together, the volume ratio of these two components was 4:1. Thus, the overall absorption attenuation of the microbubble would be dominated by the copolymer shell and significantly greater than water for x-ray photon energies ranging from 5 keV to 120 keV. Therefore, the regional absorption attenuation coefficients of the microbubble suspensions would increase as the population of microbubbles per volume increases until becoming saturated. The difference of attenuation coefficients between water and microbubble concentrations was more significant for the low-energy portion from 5 to 40 keV than for the high-energy portion from 40 to 120 keV. Thus, based on the same radiation dose delivery and similar entrance exposure level, the high-energy photons

employed in high-energy in-line mode provided fewer contributions to the imaging contrast than in low-energy contact mode. Therefore, combining all of these absorption attenuation coefficient impacts with system DQEs toward the signal intensities of microbubble suspensions, the behavior of the CNR-concentration curves can be explained, and the imaging contrasts of high-concentration microbubble suspensions (>0.5 %) were dominated by the attenuation contrast and constrained by the intrinsic characteristics of the corresponding system used.

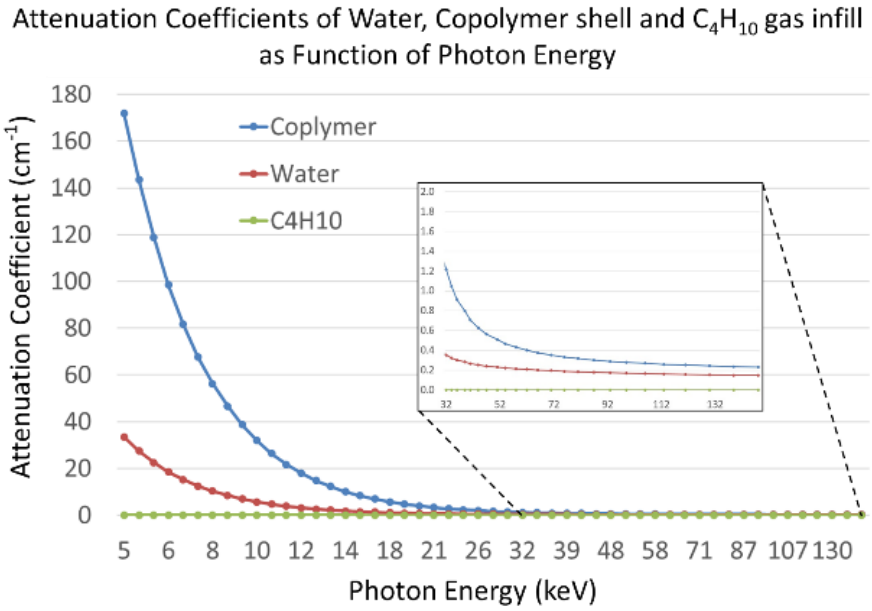

Figure 50: Attenuation coefficient of water, copolymer and C_4H_{10} gas infill calculated by multiplying the densities (1000 mg/cm^3 for water, 1600 mg/cm^3 for the copolymer, and 2.51 mg/ cm^3 for C_4H_{10} gas) with mass attenuation coefficient data for each compound acquired from the NIST database.

For the low-concentration zone from 0.1 to 0.5%, the effects of microbubble concentration changes on the attenuation coefficient values are not significant, since the population per volume of the microbubble is very low. Thus the impact of the high attenuation from the copolymer becomes less significant than in the high concentration

distributions. Considering the microbubble was made of copolymer shell (10.64 g/mole in effective atomic mass and 1.6 g/cm^3 in density) and isobutene gas infill (4.152 g/mole in effective atomic mass and 2.51×10^{-3} g/cm^3 in density), the estimated average electron density of the microbubble can be different from water (6.005 g/mole in effective atomic mass and 1.00 g/cm^3 in density). This difference of electron densities may induce more phase shift for microbubble-distributed areas than for the water-only area. As mentioned in Section 6.1, $\phi(x,y) = -\frac{2\pi}{\lambda}\int \delta(x,y,z)\mathrm{d}z$, this rapid change of phase between microbubble-distributed and water-only areas may further induce more phase image intensity changes based on the relationship of $I(x,z) = 1 + \frac{\lambda z}{2\pi}\Delta\phi(x)$, [17-19] where $I(x,z)$ represents the pure phase image intensity and Δ is the Laplacian operator. Thus, by retrieving the phase shifts resulting from the electron density discrepancies, the imaging qualities of microbubble images acquired by high-energy in-line phase contrast can be preserved even when the microbubble concentration is as low as 0.1 %, but is still constrained by the quantum efficiency of the imaging system.

As detailed in Ref. [89-90], the application of the PAD phase retrieval method may also suffer from imperfections due to the composition of the x-ray photon energies. The optimal PAD application conditions may be achieved experimentally using heavy filtrations to remove x-ray photons with energy under 60 keV. [89, 91] Thus, the 2.5 mm Al prime beam filtration was used in this study to remove most of the x-ray photons under 30 keV, as well as to introduce the technical trade-off condition to approximately satisfy the application condition of the PAD retrieval method.

6.5 Chapter Conclusion

In this study, area CNRs were measured from images of a custom designed tissue simulating phantom using different concentrations of microbubble suspensions for a comparison of high-energy in-line phase contrast with low-energy conventional imaging at the same radiation dose of 2.59 mGy. In addition, the impacts of microbubble shell materials on the imaging qualities of in-line phase contrast were investigated. To the best of our knowledge, this is the first study of its kind.

The comparison of CNR-Concentration curves for both imaging methods demonstrated that CNR values monotonically increase with the microbubble concentration. In addition, the overall CNRs for low-energy conventional mode are higher than that of high-energy in-line phase contrast mode, with the exception of the low-concentration zone where the CNR values of both imaging methods are comparable. As detailed in the discussion section, although the difference factor of electron densities existing between water and microbubbles is still within the same scale of magnitude, the PAD phase retrieval preserved the imaging contrast of high-energy in-line phase contrast mode, especially for low concentration values. However, the absorption attenuation of the copolymer shells still plays an important role in generating imaging contrast. Therefore, if the benefits of applying microbubbles as an x-ray phase contrast agent can be observed, the selection of the appropriate microbubble must be optimized. It may follow the criteria of minimizing the impacts of microbubble shell materials and gas infill on absorption attenuation coefficient, and maximizing the difference factor of electron densities among microbubbles, blood and surrounding tissues. In future studies, the use of microbubbles

as a contrast agent for in-line phase contrast imaging will be further investigated by utilizing optimized microbubble products and 3D imaging techniques to demonstrate the potential in improving imaging qualities at a regulated or reduced dose delivery.

Chapter 7. Preliminary Phantom Study of Imaging Microbubbles Distributions by Using a High-energy In-line Phase Contrast Tomosynthesis Prototype

7.1 Introduction

An in-line phase contrast tomosynthesis prototype operating with a high tube voltage of 120 kVp was demonstrated by combining the in-line phase contrast technique and digital tomosynthesis to further improve the imaging quality. The phantom studies introduced in Section 4.5 demonstrated that this imaging system is capable to successfully remove the structure overlapping in phantom projections, delineate interfaces, and achieve enhancement in contrast-to-noise ratios after applying the phase-attenuation duality (PAD) based phase retrieval to the angular projections. [90]

In order to further improve the imaging quality and specificity and maximize the advantage of the phase contrast mechanism, either by itself or combined with 3D imaging techniques, concepts of tissue engineering were proposed to introduce the application of microbubbles into phase contrast related imaging techniques. Microbubbles, which have been widely used as an ultrasonic contrast agent, can be considered as a population of x-ray lens scattering x-ray photons providing a sequence of multi-refraction. Previous studies in x-ray phase related imaging have demonstrated the ability of microbubbles to provide additional phase shift information around tissue and/or along the contours among tissues in x-ray phase contrast imaging, as well as enhancement to the x-ray phase shift during the propagation to the microbubble location. [22-29]

This study experimentally demonstrates an imaging method employing high-energy in-line phase contrast tomosynthesis with the administration of microbubbles as an x-ray scattering agent under a limited radiation dose delivery, which has not been investigated in the past. The high-energy in-line phase contrast tomosynthesis prototype was optimized by employing the low-energy removal filter described in Chapter 5. The imaging qualities of the breast tissue simulating phantom after administration of microbubbles in different concentrations were estimated by calculating the contrast-to-noise ratios (CNRs) of the regions of interest (ROIs).

7.2 Prototype Configuration

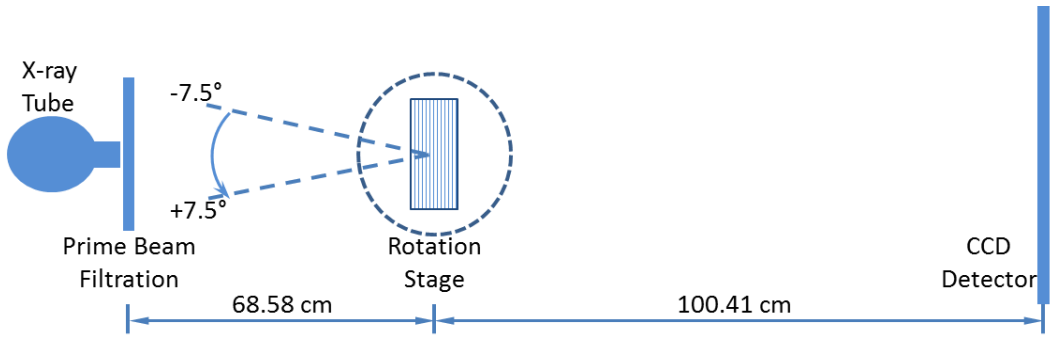

Figure 51: The experimental prototype of the high-energy in-line phase contrast tomosynthesis system employed for imaging microbubble concentrations.

This study employed the Hamamatsu microfocus x-ray source detailed in Section 3.4.1. The in-line phase contrast angular images were acquired with 120 kVp tube voltage, 500 µA tube current and 50 µm focal spot size. A prime beam filter made of 2.3 mm Cu, 0.8 mm Pb and 1.0 mm Al was utilized to harden the prime beam and the resultant x-ray photon composition was 82.2% of photons with energy higher than 60 keV. [89] The image detection system was the CCD detector detailed in Section 3.4.2, providing 21.6

μm of sampling pixel pitch. The OptoSigma rotation stage was utilized to provide the tomosynthesis mechanism.

As illustrated in Figure 51, the test objects were placed at the center of the rotation stage and rotated with respect to the rotation center from -7.5° to +7.5° with 1.5° increments to achieve 11 angular scans. This experimental setting is equivalent to the traditional isocentric motion mode, in which both the x-ray source and detector rotate around a fixed pivot point synchronously. The source-to-object distance (SOD) and the source-to-image distance (SID) values of 68.58 and 100.41 cm, respectively, were selected to deliver optimal phase-shift effects according to the principles of in-line phase contrast imaging, as well as to reduce the loss of x-ray photons during propagation through the air gap. [53, 57, 61] The 11 angular images were acquired under a total average glandular dose of 2.590 mGy, which is approximately double the mammography dose level on a 40 mm thick 50/50 compressed "average" breast. Thus, the exposure time of each projection was 43s, which was determined through the same method as detailed in Section 5.3.

After angular projections of the test objects were acquired by the system, the series of angular projections were processed by the modified Feldkamp–Davis–Kress (FDK) backprojection algorithm detailed in Section 3.5.

7.3 Phantom Design

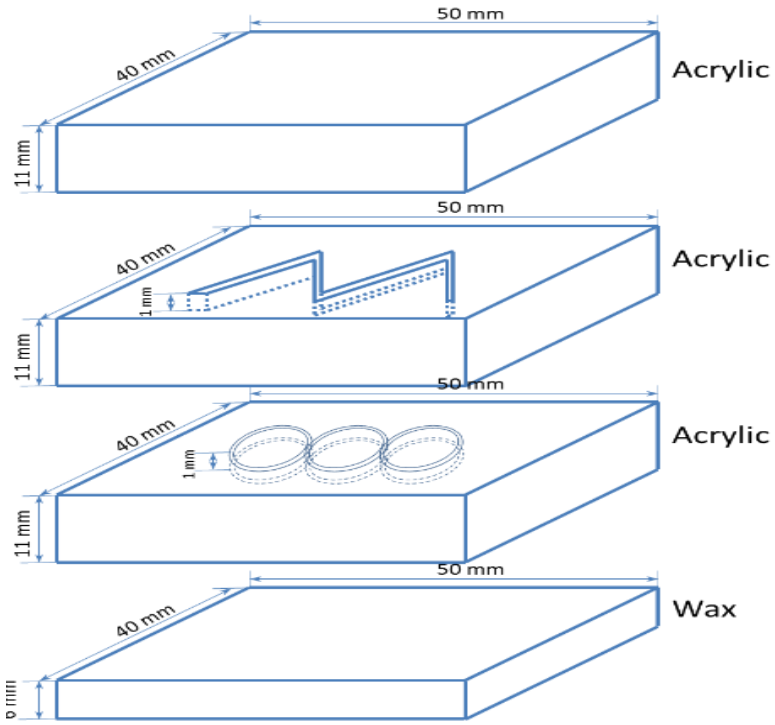

Figure 52: The schematic of the four-layer phantom simulating a 40 mm thick compressed breast. The phantom consists of three 50×40×11 mm^3 acrylic slabs and one 50×40×6 mm^3 beeswax board. There are two patterns with 1 mm depth engraved on the middle two layers. The widths of the patterns range from 0.2 mm to 1.0 mm.

As depicted in Figure 52, the phantom utilized in this research consists of three 50×40×11 mm^3 acrylic boards and one 50×40×6 mm^3 beeswax board to build up the four-layer breast simulation phantom. This phantom can be considered equivalent to a 40 mm thick compressed human breast. There were two patterns with 1 mm depth engraved on the middle two layers. The widths of the patterns ranged from 0.2 mm to 1.0 mm. After the engraving processes were completed on the middle two layers, the four layers were glued together. The engraved lines and the circles were designed to simulate the blood vessels inside and around the breast tissues. The microbubble suspension was injected into the two sealed structures through holes drilled on the sides of the corresponding layers. There

were two holes on each structured layer to perform communicating vessel effect and to ensure the tiny structure could be filled up with microbubble suspension.

The microbubbles suspension employed in this research was OPTISON microbubbles produced by GE Healthcare. Before administration, the microbubbles must be re-suspended by gentle rotation between two hands at room temperature until the appearance of the microbubble suspension in the vial becomes similar to milk. Each OPTISON mL contains 5.0×10^8 to 8.0×10^8 microbubbles dissolved in 0.9% aqueous sodium chloride (NaCl) as the suspension medium. Therefore, the microbubble suspension can be further dissolved by adding 0.9% aqueous sodium chloride to acquire different relative concentrations compared with the origin. The relative concentrations administrated in this research were 100%, 50%, 20% and 0% (control study, 0.9% aqueous sodium chloride), which correspond to the volume concentrations of 0.8 %, 0.4 %, 0.16 % and 0 %.

7.4 Results and Discussion

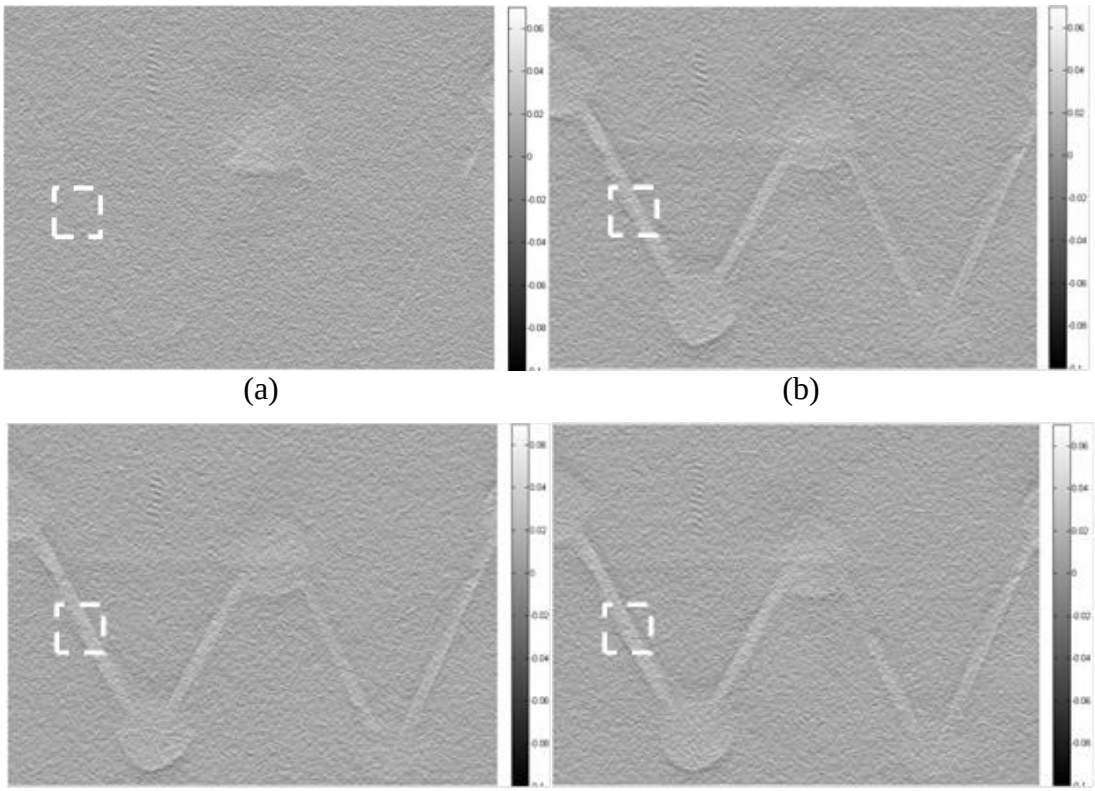

Figure 53: The in-plane images of the fiber features reconstructed from the phase contrast angular projections under different concentration of microbubble suspensions, (a) 0 %, (b) 0.16 %, (c) 0.4 %, and (d) 0.8 %, respectively. The slice thickness was 0.10 mm for each concentration mode.

From the imaging results obtained for each microbubble concentration, in-plane images at depths corresponding to the fiber layers in the phantom are shown in the Figure 53. The dashed-line squares denote the selected areas for calculation of the relative contrast-to-noise ratios. The relative CNR values were calculated by employing Equation (38):

$$\mathrm{CNR} = \frac{I_S - I_B}{\sigma} \tag{38}$$

where I_S, I_B, and σ represent the average intensity value of the area filled with microbubble suspension in the ROI, the average intensity value of the background where there are no features, and the noise, respectively. The individual parameter and overall

CNR values calculated for each concentration are shown in Table 14. The CNR values calculated based on the in-plane images corresponding to the fiber structures versus the microbubble concentrations are shown in Figure 54.

Table 14. I_S, I_B, σ, and CNR values calculated from the images.

Concentration	0% (Saline)	0.16%	0.40%	0.80%
Signal (I_S)	14.62	16.10	21.15	22.94
Background (I_B)	10.82	10.44	10.44	10.35
Noise (σ)	1.37	1.40	1.40	1.42
CNR	2.77	4.03	7.66	8.86

The results shown in Figure 53 demonstrated that the layers of superimposed structures were distinguishable from one another, and this is credited to the capability of tomosynthesis to reduce structure overlapping. Since the imaging slices were reconstructed from the in-line phase contrast angular projections, the reconstructed imaging values originated from combined effects of both phase shift and attenuation values recorded by the projections. Thus, these effects also perform a monotonically increasing relationship with the tomosynthesis reconstructed imaging values. The relationship was demonstrated in this study and shown in the Table 1. The average pixel values of the acrylic background were relatively unchanged due to the phase shifts, and the attenuations were relatively stationary during the constant-dose exposures regardless of the microbubble suspension concentration. Due to the increased combined effects of phase shift and attenuation introduced by increasing the microbubble concentration, the average pixel values in the injection location of the microbubble suspensions monotonically increased with the microbubble concentration. Also, the CNR curve shown in Figure 54 behaves in agreement with this relationship. Therefore, in the future,

such a curve can potentially be utilized to quantitatively characterize the concentration of microbubbles in blood vessels after isolating the phase shift effects by processing tomosynthesis reconstructions onto the phase maps of the phase contrast projections.

The unevenly-distributed microbubbles within the tiny structures may cause high uncertainties in locating the microbubbles and processing quantitative calculations. This experimental imperfection was probably due to the miss-injection as well as the nature of microbubble suspensions that cause microbubbles to become unevenly distributed during a long exposure. The focal spot size of the x-ray used in this study was 50 microns, which is larger than the diameters of the microbubble, thus the in-line phase contrast effects were not fully realized and did not make much contribution in increasing the imaging qualities.

To solve the problems observed in this study, a smaller x-ray focal spot size may be employed in future experimental studies. However, the smallest focal spot setting induces much longer exposure times than used in this study. Therefore, rotation of the phantom during image acquisitions or the use of a circulation mechanism for the microbubble suspensions will have to be employed to maintain evenly-distributed microbubble suspensions while processing long exposures.

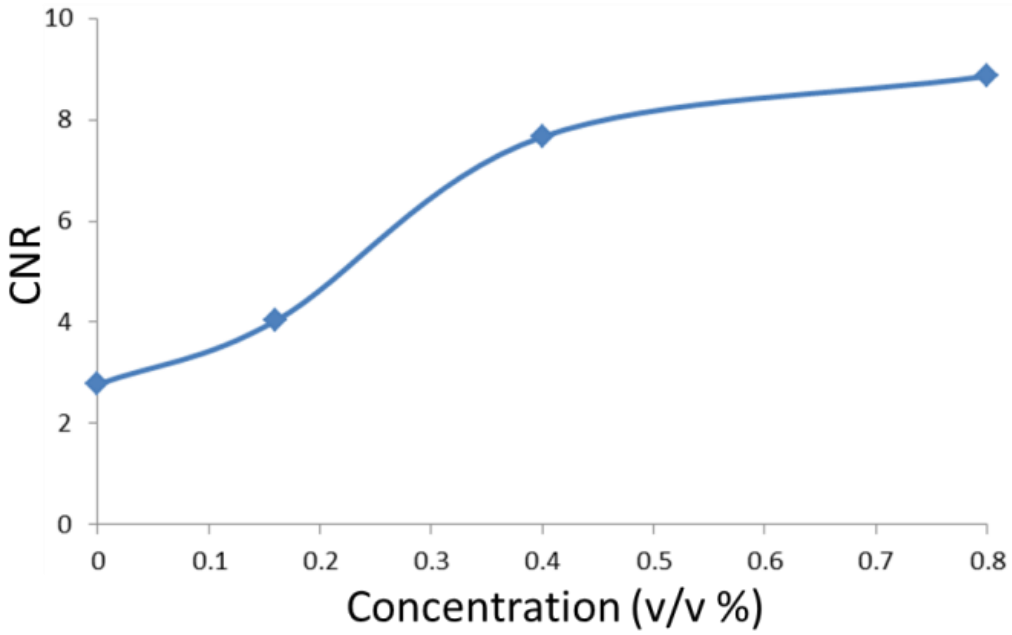

Figure 54: The relationship between the concentrations of microbubble suspensions and the calculated CNRs of the corresponding concentrations.

7.5 Chapter Conclusion

In this study, the monotonically increasing relationship between the concentration of microbubbles and the imaging CNRs was demonstrated and investigated. A breast simulating phantom was injected with microbubbles and tomosynthesis reconstructions were produced from in-line phase contrast projections that were acquired under a unified dose delivery of double the conventional mammography dose. The results demonstrated significant differences between microbubbles injected images and a non-microbubble saline injected image. In addition, the x-ray exposure with removal of a large percentage of the low energy photons demonstrated adequate contrast in imaging a soft tissue simulating phantom. These results supported the feasibility of using the low energy removing filter as the prime beam filter, which would result in the dominance of x-ray

photons with energies higher than 60 keV. For future studies, this provides an experimental solution to satisfy the PAD application condition. [13, 58] However, the long exposure time and relatively high radiation dose are still challenges in need of solutions. Future studies will investigate the isolated phase shift effects as well as conduct a more comprehensive comparison study with conventional breast tomosynthesis.

Chapter 8. Edge Enhancement Provided by Distributing Microbubbles on the Interface between Tissue and Surrounding Blood Vessels: A Phantom Study

8.1 Introduction

Since a clinical microbubble-based contrast agent was first investigated using x-ray diffraction enhanced imaging in 2010, [22] applications of microbubbles and/or microspheres as x-ray phase contrast agents have attracted extensive research attention. Recent research progress toward the application of microbubbles as an x-ray phase contrast agent have demonstrated the imaging of microbubbles/microbubble suspensions using analyzer-based and propagation-based synchrotron x-ray phase contrast, [23] synchrotron free space propagation phase contrast methods [24,25] and the Talbot-Lau interferometry phase contrast method. [26, 27] In 3D and quasi-3D imaging, computed tomography imaging of microbubbles was also demonstrated through a differential phase contrast system accompanied with object rotation, [29] and quantitative in-line phase contrast tomosynthesis imaging of microbubble suspensions was experimentally demonstrated by combining high-energy in-line phase contrast method with the tomosynthesis technique, as detailed in the previous chapter. [91] In addition, microbubble contrast agents can also provide the potential to perform dynamic imaging with analyzer-based synchrotron x-ray phase contrast. [28]

A single microbubble generally consists of a shell and gas infills. To our scope of knowledge, the materials of the shell may be made of polymers, proteins, lipid, etc., and sudden changes of physical density and electron density related to the materials of microbubbles introduce significant phase contrast for x-rays at the interfaces between

gas-filled bubbles and tissue when a group of microbubbles are distributed along the interfaces. [22-28] For example, distributing microbubbles around certain malignant tumor cells can be potentially performed using a ligand-targeted technique, which has already been introduced and developed in the research field of ligand-targeted cancer therapeutics and imaging agents. [92] By transferring microbubbles, such as OPTISON and BRACCO, from their original clinical use into ligand-targeted imaging agents, the high-density ligand on the surfaces of microbubbles may dramatically increase the probabilities of microbubbles to become trapped by the receptors on the endothelium of blood vessels surrounding the malignant cells. [93, 94] Therefore, using ligand-targeted microbubbles to perform x-ray phase contrast imaging has the potential to increase the imaging accuracy and specificity, and the phase contrast induced edge enhancement provided by the distribution of microbubbles on the interface between vascular and tissue may be observed.

In this study, we employed a custom designed phantom with a simple vascular structure inside to demonstrate how edge-enhancement in in-line phase contrast projection and tomosynthesis imaging can be provided by distributing microbubbles on the surface between the vascular structure and the tissue. Since the distribution of microbubbles along the interface is directly related to the concentration of microbubble suspension injected into the phantom, different concentrations of microbubble suspensions will be utilized. The comparison studies will be conducted for 2D and 3D conventional low-energy contact mode, low-energy in-line phase contrast mode and high-energy in-line phase contrast mode under the same radiation dose delivery.

8.2 Methods and Materials

8.2.1 Imaging Systems

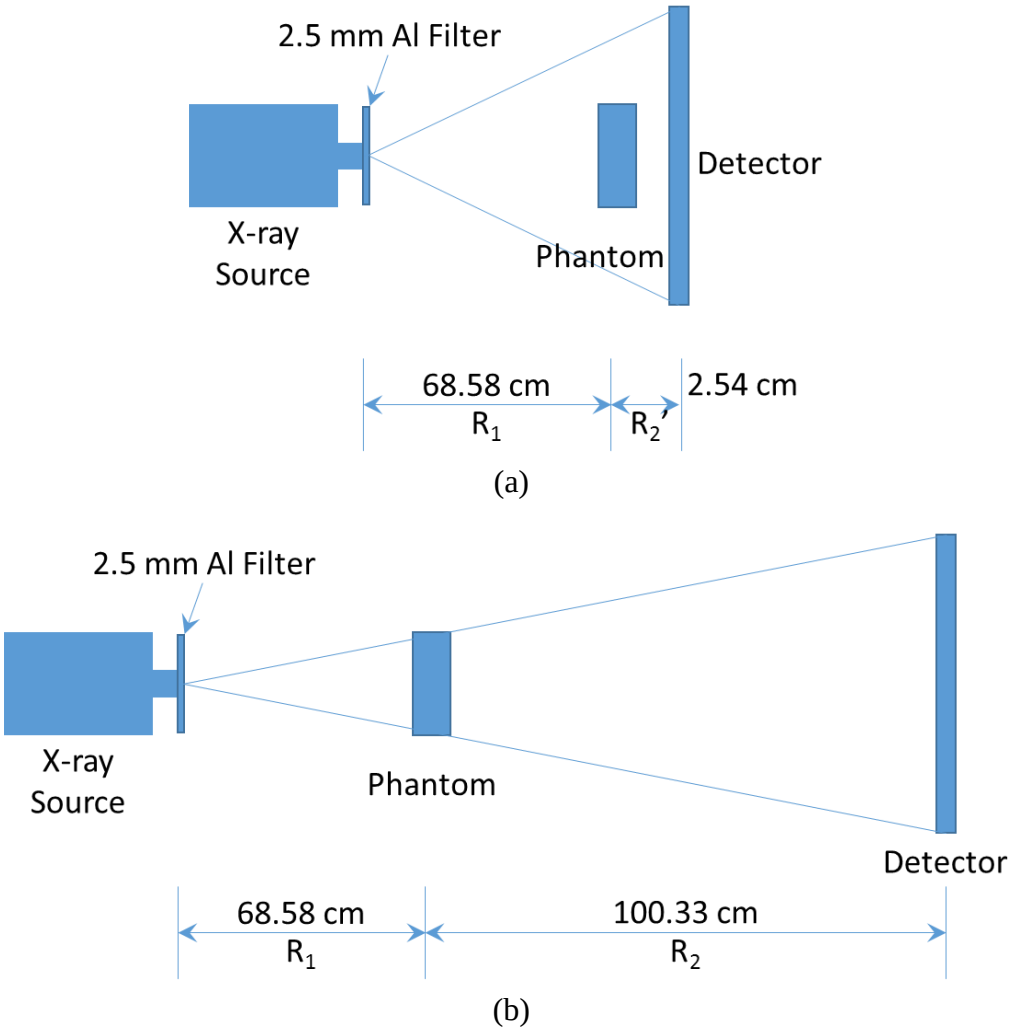

Figure 55: The imaging system configurations employed for (a) conventional low-energy contact mode and (b) in-line phase contrast modes. The phantom will be rotated according to the acquisition parameters to perform the tomosynthesis mechanism.

Table 15. X-ray tube voltages and currents for different imaging modes

	Low-energy Contact Mode	Low-energy In-line Phase Contrast	High-energy In-line Phase Contrast
Tube Energy (kVp)	40	40	120
Tube Current (mA)		0.5	

As shown in Figure 55, the phantom was placed on a stage. The source-to-object distance (SOD), R_1, was 68.58 cm for both the contact mode and the in-line phase contrast mode. The object-to-image distance (OID), R_2, for the in-line phase contrast mode was determined to be 168.91 cm to deliver optimal phase shift effects according to the principles of in-line phase contrast imaging, as well as to reduce the loss of x-ray photons during propagation through the air gap, [53, 57, 61, 90]. The value of R_2 utilized for contact mode imaging was 2.54 cm. In this study, a micro focus x-ray source (Model L8121-03, Hamamatsu Photonics) able to generate x-ray photons ranging from 40 kVp to 150 kVp with an adjustable tube current was employed. The nominal focal spot sizes of 7 μm, 20 μm, and 50 μm can be selected and/or determined by the desired output power. The selections of x-ray tube voltages and currents for different imaging modes used in this study are detailed in Table 15. A prime beam filter of 2.5 mm Al was utilized to harden the prime beam for both phase contrast mode and contact mode. [89] The image detection system was a CCD detector coupled with a CsI:Tl scintillator (66 mm×66 mm, Imagestar 9000, Photonic Science Ltd.), providing 21.6 μm of sampling pixel pitch. The measurements were conducted with an average glandular dose value of 2.590 mGy, which was calculated based on a 50/50 breast tissue composition. This dose regulation was also used to determine the exposure time of each imaging mode by employing the same method detailed in Ref. [89]. The resultant exposure time for each imaging mode is

shown in Table 16, corresponding to the investigations under different tube voltages, respectively.

Table 16. Experiment parameters for the investigation of different kVp.

Tube Voltage (kVp)	Tube Current (mA)	Prime Beam Filtration	D_g (mGy)	D_{gN} (mrad/R)	X_{ESE} (mR)	R_X (mR/s)	Exposure Time(s)
40	0.5	2.5 mm Al	2.590	5.88	440.48	2.13	206.80
120				5.79	447.32	24.80	18.04

D_g: average glandular dose, D_{gN}: normalized average glandular dose coefficient, X_{ESE}: object entrance exposure, R_X: entrance exposure rate.

For image acquisition in each projection mode, three projections were acquired and averaged into one image. For image acquisition in tomosynthesis imaging mode, 11 angular projections were taken from -7.5° to +7.5° in 2° increments while the object was being rotated. Thus, in tomosynthesis imaging mode, the exposure time for each angular projection was the total exposure time of the corresponding kVp divided by 11 projections. After angular projections of the test objects were acquired for tomosynthesis imaging mode, the series of angular projections were processed by the modified Feldkamp–Davis–Kress (FDK) backprojection algorithm detailed in the Section 3.5 to obtain reconstructed tomosynthesis in-plane images.

8.2.2 Phantom Design

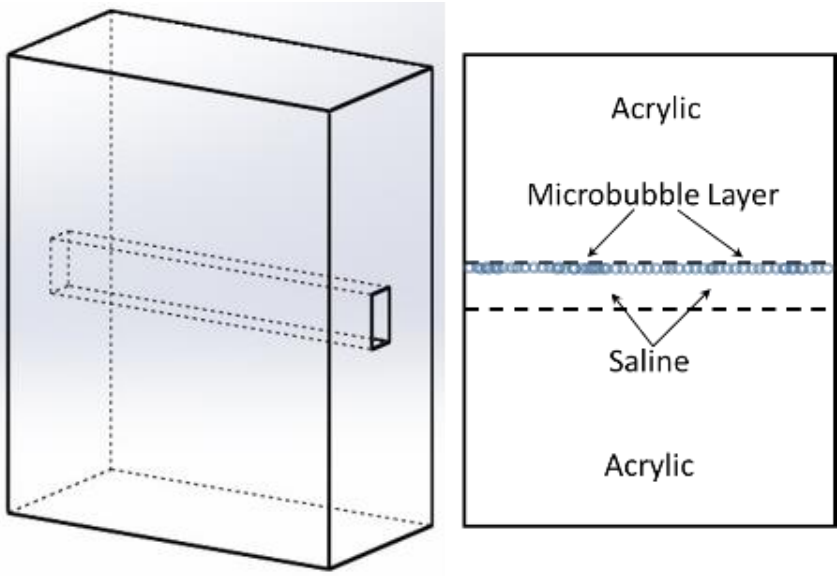

Figure 56: Schematic of the tissue-vascular simulation phantom

The schematic of the phantom is provided in Figure 56. A 40 mm-thick acrylic slab was employed to simulate a 4 cm compressed breast tissue. A rectangular cavity was fabricated inside the acrylic slab to facilitate injection of the microbubble suspensions with different concentrations. The microbubbles employed in this study were OPTISON microbubbles produced by GE Healthcare. Before administration of the microbubbles, the microbubbles must be re-suspended by gentle rotation between two hands at room temperature until appearance of the microbubble suspension in the vial becomes similar to milk. Each OPTISON mL contains 5.0×10^8 to 8.0×10^8 microbubbles dissolved in 0.9% aqueous sodium chloride (NaCl) as suspension. Therefore, the suspension can be further dissolved by adding 0.9% aqueous sodium chloride to acquire different relative concentrations compared with the origin. The relative concentrations administrated in this research were 50 %, 25 %, 12.5 %, 6.25 % and 0% (control study, 0.9% aqueous sodium

chloride only), which correspond to the volume concentration (V/V %) of 0.40 %, 0.20 %, 0.10 %, 0.05 % and 0.00 %. Before acquiring images of the phantom, the microbubble suspensions were injected into the acrylic phantom and waited for 5 minutes to allow the microbubbles to become distributed at the interface between the acrylic and the cavity.

8.2.3 Edge-enhancement-to-noise ratio

The edge-enhancement-to-noise ratio (EE/N) was employed to quantify the edge features between the water infilled tube and the tissue-simulating acrylic slab, and was determined by Equation (37):

$$\frac{EE}{N} = \frac{\text{Max}-\text{Min}}{\sqrt{\frac{\sigma_{\text{L}}^2+\sigma_{\text{R}}^2}{2}}} \tag{37}$$

where Max, Min, σ_{L} and σ_{R} denote the maximum intensity value of the edge, the minimum intensity value of the edge, the standard deviation of the left-side background, and the standard deviation of the right-side background, respectively. In this study, the backgrounds of the edge were defined as regions of 51 pixels adjacent to the left and right of the edge. The averaged horizontal profile intensities along the maximum-value lines were plotted for calculating EE/N.

8.3 Results

8.3.1 Projection Imaging Results

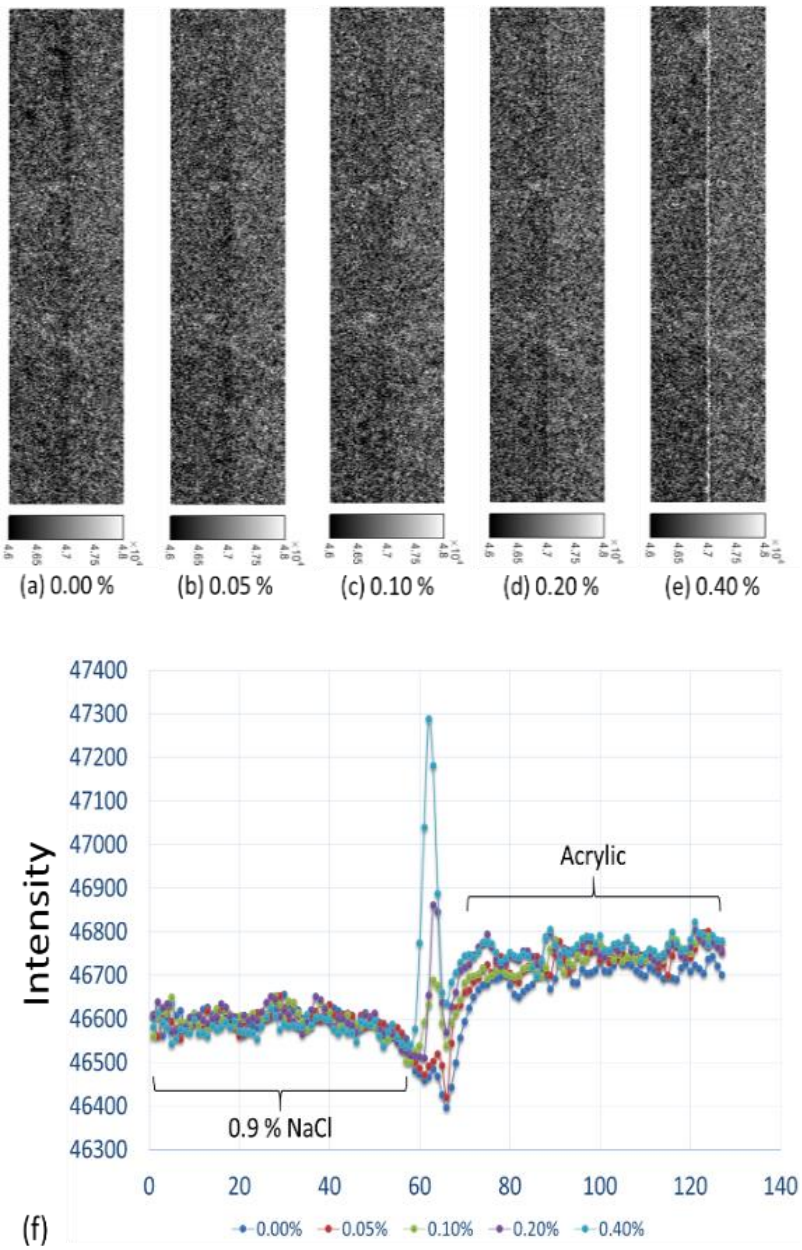

Figure 57: (a)-(e) Conventional contact-mode projection images acquired under 40 kVp x-ray tube voltage for administration of 0.00 % to 0.40 % microbubble suspensions. (f) Averaged intensity profiles of conventional contact-mode projection along the boundary between salt water and acrylic under different concentration administrations of microbubbles.

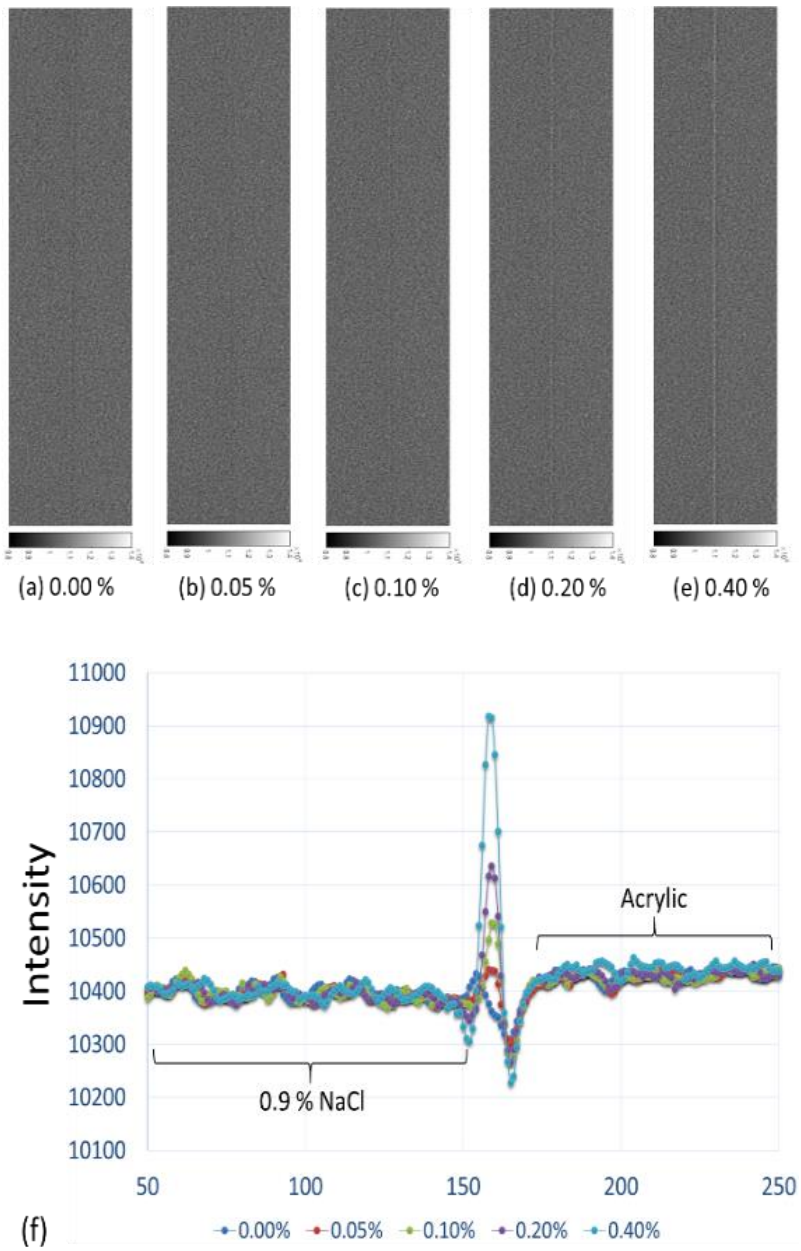

Figure 58: (a)-(e) In-line phase contrast projection images acquired under 40 kVp x-ray tube voltage for administration of 0.00 % to 0.40 % microbubble suspensions. (f) Averaged intensity profiles of low-energy in-line phase contrast projection along the boundary between salt water and acrylic under different concentrations of microbubble administration.

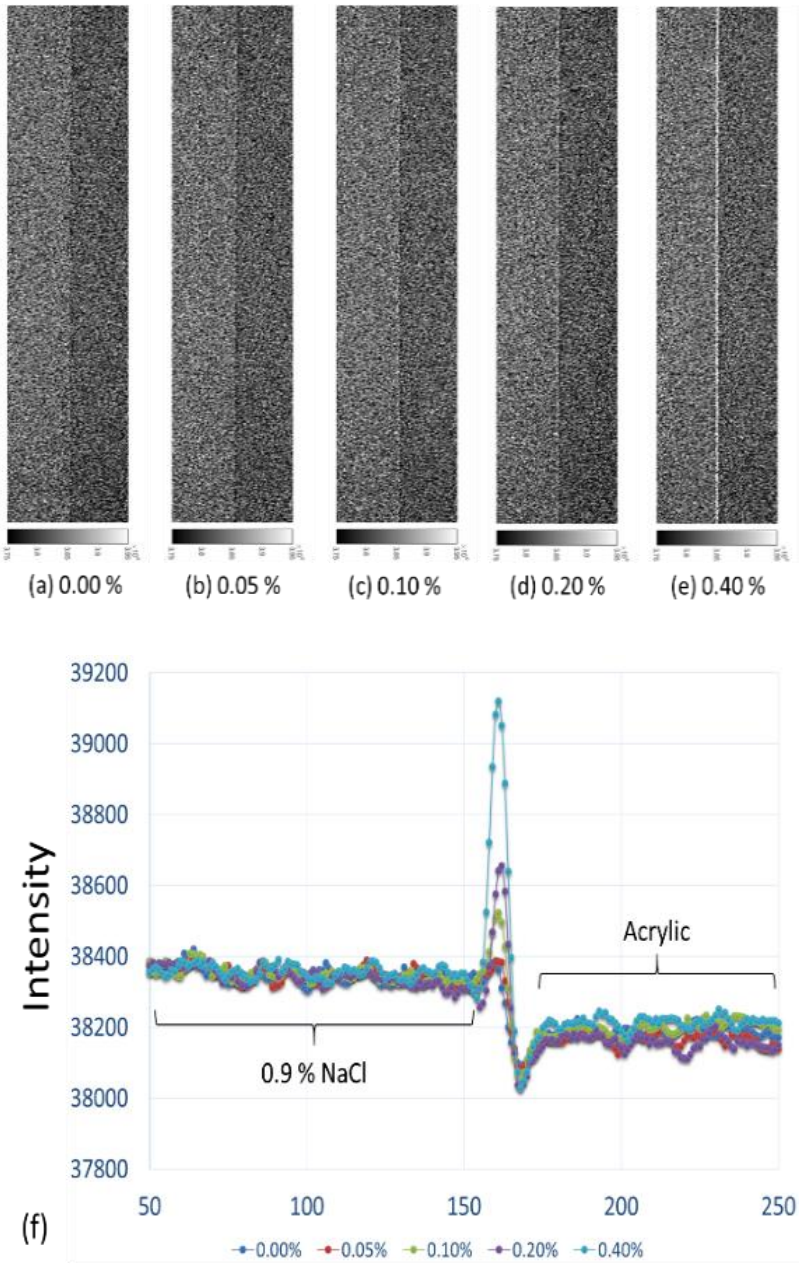

Figure 59: (a)-(e) In-line phase contrast projection images acquired under 120 kVp x-ray tube voltage for administration of 0.00 % to 0.40 % microbubble suspensions. (f) Averaged intensity profiles of high-energy in-line phase contrast projection along the boundary between salt water and acrylic under different concentrations of microbubble administration.

The images acquired using low-energy contact-mode, low-energy in-line phase contrast and high-energy in-line phase contrast projections after distributing different concentrations of microbubbles along the interface between the salt water and the acrylic slab are shown in Figure 57(a)-(e) through Figure 59(a)-(e). Each image was acquired under 2.59 mGy radiation dose criteria. Figure 57(f) through Figure 59(f) illustrate the averaged intensity profiles plotted along the microbubble-distributed interfaces according to the images shown in (a)-(e).

8.3.2 Tomosynthesis Imaging Results

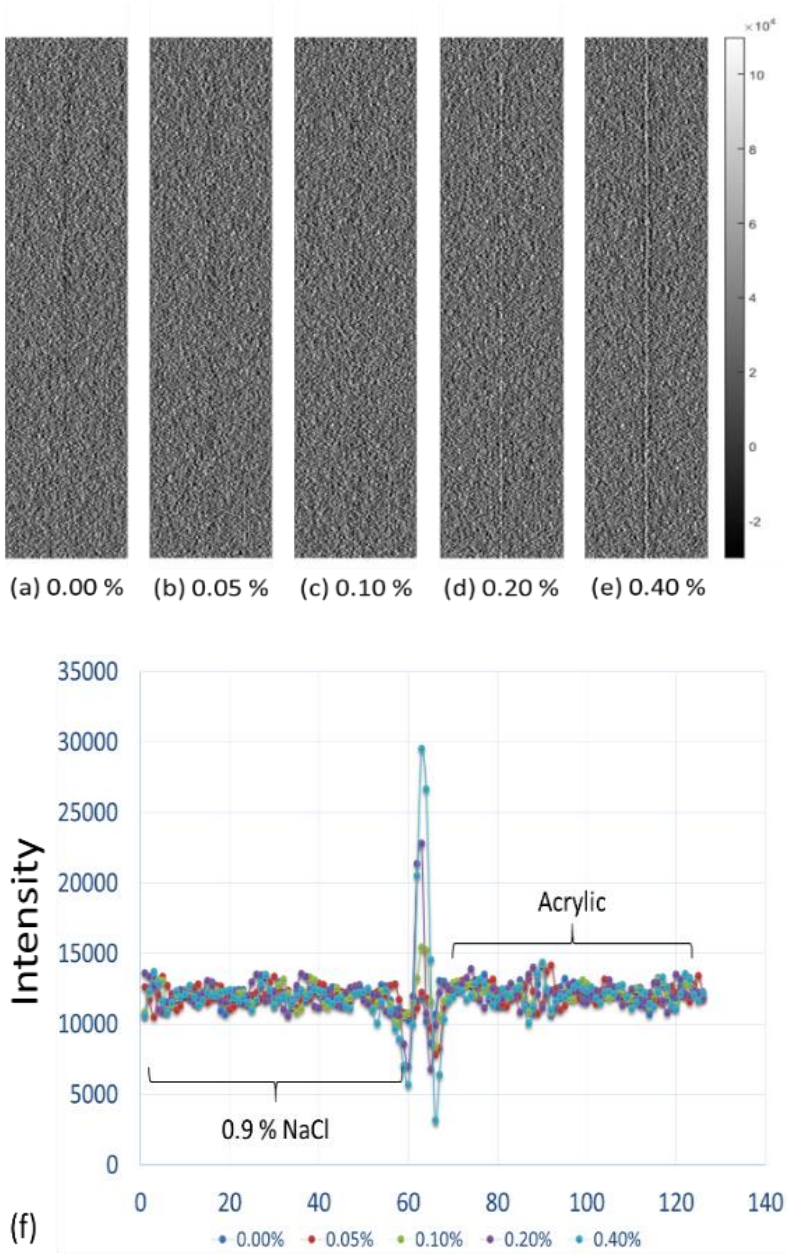

Figure 60: (a)-(e) Conventional contact-mode tomosynthesis in-plane images acquired under 40 kVp x-ray tube voltage for administration of 0.00 % to 0.40 % microbubble suspensions. (f) Averaged in-plane intensity profiles of low-energy conventional contact-mode tomosynthesis along the boundary between salt water and acrylic under different concentrations of microbubble administration.

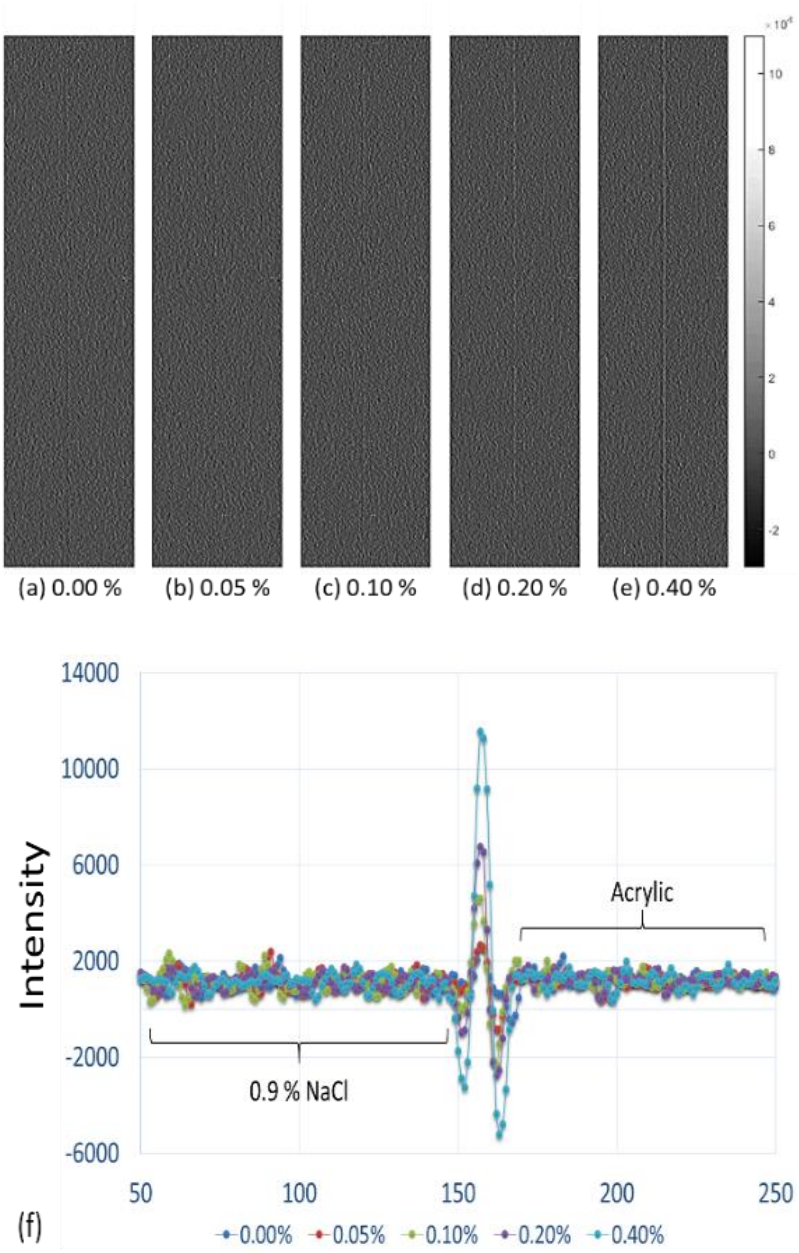

Figure 61: (a)-(e) In-line phase contrast tomosynthesis in-plane images acquired under 40 kVp x-ray tube voltage for administration of 0.00 % to 0.40 % microbubble suspensions. (f) Averaged in-plane intensity profiles of low-energy in-line phase contrast tomosynthesis along the boundary between salt water and acrylic under different concentrations of microbubble administration.

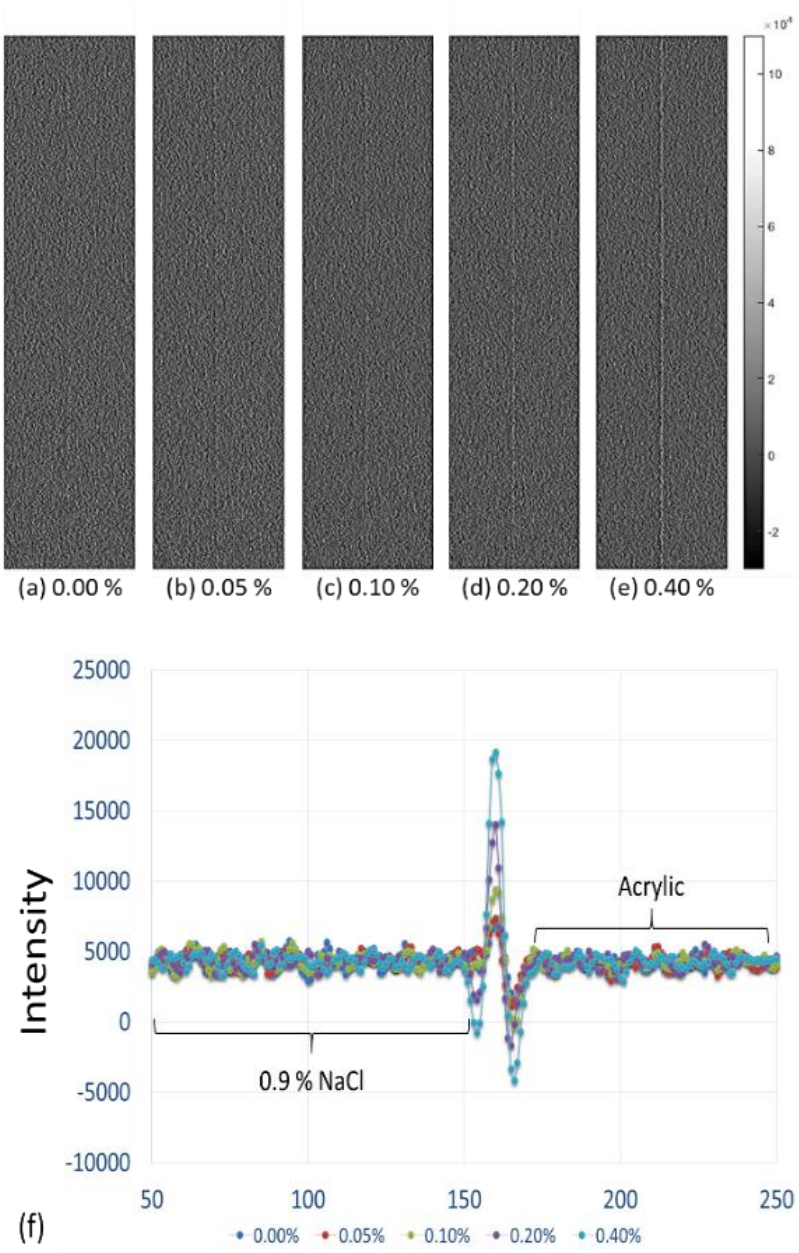

Figure 62: (a)-(e) In-line phase contrast tomosynthesis in-plane images acquired under 120 kVp x-ray tube voltage for administration of 0.00 % to 0.40 % microbubble suspensions. (f) Averaged in-plane intensity profiles of high-energy in-line phase contrast tomosynthesis along the boundary between salt water and acrylic under different concentrations of microbubble administration.

The in-plane images of distributing different concentrations of microbubbles along the interface between the salt water and the acrylic slab acquired by using low-energy contact-mode, low-energy in-line phase contrast and high-energy in-line phase contrast tomosynthesis are shown in Figure 60(a)-(e) through Figure 62(a)-(e). Each image was acquired under 2.59 mGy radiation dose criteria, and the in-plane slices were 2.0 mm in thickness for each imaging mode. Figure 60(f) through Figure 62(f) illustrate the averaged intensity profiles plotted along the microbubble-distributed interfaces according to the images shown in (a)-(e).

8.3.3 Edge-enhancement-to-noise Ratios

Table 17. Edge intensity, noise and EE/N of low-energy contact mode projection

Concentration	0.00%	0.05%	0.10%	0.20%	0.40%
Max-Min	87.35	99.32	150.91	291.95	652.40
Noise(R)	23.45	23.72	26.92	19.71	23.14
Noise(L)	19.37	20.75	20.91	21.80	17.01
EE/N	4.06	4.46	6.26	14.05	32.12

Table 18. Edge intensity, noise and EE/N of low-energy in-line phase contrast projection

Concentration	0.00%	0.05%	0.10%	0.20%	0.40%
Max-Min	123.33	140.48	263.65	369.40	689.90
Noise(R)	9.25	9.97	7.82	9.38	12.03
Noise(L)	12.39	12.36	13.21	10.79	11.14
EE/N	11.28	12.51	24.30	36.54	59.52

Table 19. Edge intensity, noise and EE/N of high-energy in-line phase contrast projection

Concentration	0.00%	0.05%	0.10%	0.20%	0.40%
Max-Min	295.78	305.50	472.34	624.34	1091.75
Noise(L)	13.08	13.18	13.18	15.25	16.66
Noise(H)	18.68	14.54	12.86	14.13	16.32
EE/N	18.35	22.02	36.28	42.48	66.21

Table 20. Edge intensity, noise and EE/N of low-energy contact mode tomosynthesis

Concentration	0.00%	0.05%	0.10%	0.20%	0.40%
Max-Min	3248.48	4375.21	7059.86	15978.83	26383.67
Noise(R)	747.41	682.46	633.64	742.54	764.62
Noise(L)	679.49	594.67	641.70	726.06	596.82
EE/N	4.55	6.84	11.07	21.76	38.47

Table 21. Edge intensity, noise and EE/N of low-energy in-line phase contrast tomosynthesis

Concentration	0.00%	0.05%	0.10%	0.20%	0.40%
Max-Min	3218.28	3534.93	6928.40	9528.35	16780.11
Noise(R)	326.71	279.85	270.87	285.23	337.84
Noise(L)	329.53	382.84	415.12	271.28	323.75
EE/N	9.81	10.54	19.77	34.23	50.72

Table 22. Edge intensity, noise and EE/N of high-energy in-line phase contrast tomosynthesis

Concentration	0.00%	0.05%	0.10%	0.20%	0.40%
Max-Min	5986.63	6152.68	9802.03	15688.65	23316.13
Noise(R)	438.86	488.60	384.21	444.89	476.35
Noise(L)	697.20	488.29	474.05	357.23	414.26
EE/N	10.28	12.60	22.72	38.89	52.23

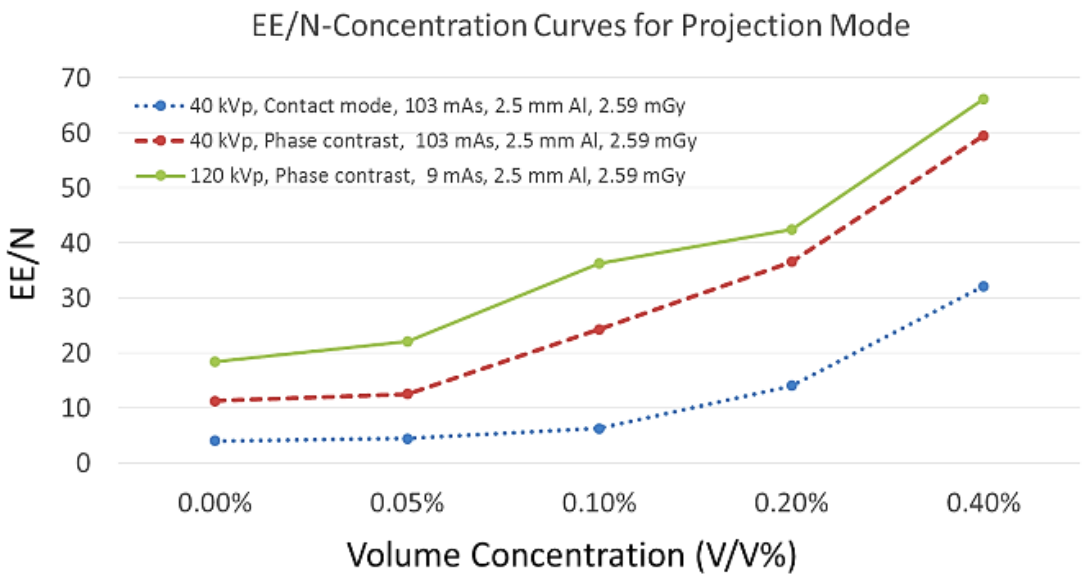

(a)

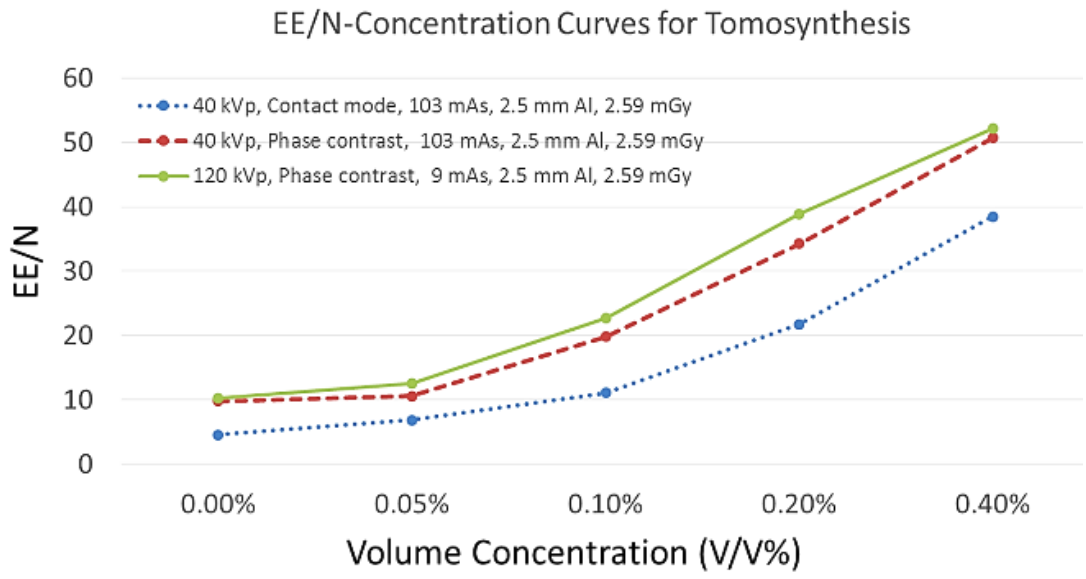

(b)

Figure 63: (a) Comparison of EE/N-Concentration curves for projection mode; and (b) comparison of edge-enhancement-to-noise ratio curves for tomosynthesis mode.

By employing Equation (1) and the method detailed in Section 8.2.3, edge-enhancement-to-noise ratios for each combination of imaging mode and microbubble distribution were calculated according to the intensity profiles shown in Figure 57 (f) through Figure 62(f). The resultant data are listed in Tables 17 through 22, and plotted as functions of volume concentration in Figure 63 (a) and (b) for projection mode and tomosynthesis, respectively.

8.4 Discussion

In this study, the imaging tasks were conducted by comparing imaging results among different tube energies and total mAs values regarding to different imaging modalities for both conventional contact mode and in-line phase contrast mode. The edge-enhancement-to-noise ratio was determined by the intensities of the edge and the background noise level. Based on the theory of noise power spectrum with system magnification, [66] under the same settings of kVp, mAs and filtration, the noise level in in-line phase contrast mode would be reduced by a factor of the square of system magnification, as compared with contact mode. The unified radiation dose delivered to the phantom in high-energy contact-mode phase contrast system and high-energy in-line phase contrast system also means the same mAs under a unified kVp and filtration. Although the detective quantum efficiency can be theoretically preserved in an in-line phase contrast mode system, the detected x-ray photons would still be reduced following the inverse square law due to the long object-to-detector distance. Thus, the intensities of the microbubble distributed edge and the tissue simulated backgrounds performed lower in the low-energy phase contrast mode than in contact mode. Despite this, the contrasts of the edge, differences between

maximum and minimum values of the intensities, were preserved in both projection and tomosynthesis in-line phase contrast mode due to the additional contribution of phase contrast. For high-energy in-line phase contrast mode at 120 kVp, the detective quantum efficiency would theoretically be much lower than low-energy mode, but the photon flux would be 9 times that of 40 kVp mode. Thus, not only can the overall imaging intensity be preserved, but also the contrasts of the microbubble distributed edges, especially when the concentration was extremely low. These phenomena were also supported by observation of the images.

Observing the images acquired under different imaging modes with delivery of a unified radiation dose, the edge features provided by distributing microbubbles at the interface between two tissue simulating structures were dramatically enhanced, as compared with images without microbubbles. This edge enhancement was improved as a function of the microbubble concentration. The images also indicate that the high-energy in-line phase contrast technique in both projection mode and tomosynthesis mode holds the highest potential to detect edge features for low-concentration microbubble distributions. These observations are also supported by the curves of edge-enhancement-to-noise ratios shown in Figure 9(a) and 9(b) for projection mode and tomosynthesis, respectively.

The conventional low-energy contact mode images represented the absorption attenuation images, and failed to provide the edge features for concentrations under 0.20%. The low-energy in-line phase contrast mode images provided a little progress toward making the edge features visible for the 0.1% concentration, thus the system magnification provided

a very limited contribution toward the edge feature improvement. However, the high-energy in-line phase contrast mode images provided highest visibility for low-concentration microbubble distributions, and rendered the 0.1% and 0.05% edges visible in projection mode and tomosynthesis mode, respectively. These phenomena may result from the high-energy photons providing sufficient compensation for the image quality degradation due to the low detective quantum efficiency through additional phase contrast and high photon flux. [61, 89, 90]

However, this study only addressed a task using a tissue simulating phantom containing a simple structure. The total numbers of microbubbles distributed on the interface have not been precisely estimated for each concentration of suspensions. Thus questions toward the number of layer of microbubbles aggregated on the interface and the multilayers issues may potentially weaken the significance of this study. However, the encouraging imaging results of the microbubble injections with concentrations less than 0.10 % acquired by the high-energy in-line phase contrast mode still provide motivation for translating phantom studies into more biology-related explorations in the future.

8.5. Chapter Conclusion

In this study, images of a custom designed tissue simulating phantom with injections of different-concentration microbubble suspensions were quantitatively acquired using low-energy conventional contact and in-line phase contrast modes, as well as high-energy in-line phase contrast projection and tomosynthesis imaging methods. The radiation dose delivered to the phantom was 2.59 mGy for all imaging modes. The phantom design and

the handling of microbubble suspensions successfully simulated a clinical condition in which the ligand-targeted microbubbles are self-aggregated on the endothelium of blood vessels surrounding malignant cells.

As this study was designed for estimating the edge enhancement provided by distributing microbubbles along the interface between two different tissues, the edge-enhancement-to-noise ratio were measured from the resultant images. The images indicated that distributing microbubbles on the interface between two different tissues holds the potential to improve the edge and/or boundary features. The quantitative edge-enhancement-to-noise ratio results illustrated a monotonically increasing relationship between the microbubble concentration and the edge-enhancement-to-noise ratio. Although a number of limitations may apply to this tissue-simulating phantom study, the imaging results of low-concentration microbubble suspensions under low radiation dose delivery still provide the motivation for future studies.

Chapter 9. Conclusion

9.1 Summary

The research presented in this dissertation demonstrates the capabilities of a high-energy in-line phase contrast tomosynthesis prototype toward clinical applications. This technique combines the capabilities of the in-line phase contrast technique and the tomosynthesis technique, based on the theories and principles detailed in Chapter 2. The imaging prototype developed in Chapter 3 is one of the main original contributions of this dissertation to the research community. The characterization works presented in Chapter 4 have been highlighted as the first imaging results of this imaging modality, and the custom-designed phantom imaging results successfully showed that phase-attenuation duality phase retrieval method is able to provide robust capability in improving the quality of tomosynthesis in-plane images, as well as biology-related phantom images.

In order to solve the imperfection of the application of phase-attenuation duality phase retrieval method, Chapter 5 provided a solution towards x-ray prime beam energy optimization. The quantitative measurements of the projection-mode imaging prototype illustrated that the combo filter designed has the capability to handle the imaging tasks for high-energy in-line phase contrast tomosynthesis, but the engineering trade-off exists with an expense of an extremely long image acquisition time.

Applications of microbubbles as phase contrast agents have demonstrated high-potential capabilities in quantitative imaging to improve the imaging qualities and specifications. Therefore, Chapter 6 presented a preliminary demonstration of quantitative imaging of

microbubbles as a phase contrast agent using projection mode imaging, which involved use of the prototype system without the tomosynthesis mechanism. The chapter also discussed how the materials of the bubble shells and gas infills could impact the imaging capability and resultant image quality. The content of Chapter 6 also provides a guideline in selecting the types of microbubbles to utilize as phase contrast agents for in-line phase contrast mode imaging modalities for future studies.

In Chapter 7, a type of microbubbles satisfying the criteria detailed in Chapter 6 was quantitatively imaged using the high-energy in-line phase contrast tomosynthesis prototype with x-ray beam optimization for phase retrieval and application of phase-attenuation duality phase retrieval. The imaging results and the dose delivery level provides motivation for future studies toward dose reduction and reduction of acquisition time.

Chapter 8 provided a completely different angle of view in utilizing microbubbles as phase contrast agents for quantitative imaging in high-energy in-line phase contrast tomosynthesis. The microbubbles were distributed on the interface between two tissue simulating materials rather than evenly suspended in a solution. This method simulated a clinical condition when the ligand-targeted microbubbles are self-aggregated on the endothelium of blood vessels surrounding malignant cells, and the comparison results provide the motivation for translating phantom studies into more biology-related explorations in the future.

9.2 Future Research Direction

The demonstrations and investigations presented in this dissertation motivate future research in not only the application and optimization of the newly developed imaging prototype itself, but also when it is utilized with auxiliary approaches in improving x-ray image detectability and specificity.

First, the characterization study of the newly developed high-energy in-line phase contrast tomosynthesis prototype provided only one prototype of the phase contrast based 3D imaging modalities in which the x-ray exposure was provided by a micro focus x-ray source and which utilized object or gantry rotation. As detailed in Chapters 1 and 2, peer researchers in the field of conventional tomosynthesis have already investigated the imaging blur and artifacts resulting from continuous-motion tomosynthesis. The weak point of step-by-step mode tomosynthesis centers on the relatively long acquisition period, since the mechanics require an additional time to stop and stabilize after every step motion. Future studies are needed to translate the source-object motion/rotation into a stationary prototype employing stationary x-ray nanotube arrays. In this case, the step-by-step or continuous motion of the x-ray source or the object can be replaced by stationary nanotubes on which nano x-ray sources at different locations are lightened by timing sequence, so that the image acquisition time can be dramatically reduced, as well as improve the accuracy of the image registration on the detector.

Another existing constraint for shortening the image acquisition period is the relatively low power of solid-target micro focus x-ray tubes. The solid target micro focus x-ray

tubes operate at tens to several hundred micro amperes, which is much lower than the operating tube current for commercial radiography systems and conventional tomosynthesis machines. Thus, in order to translate high-energy in-line phase contrast tomosynthesis into clinical applications with comparable or shorter image acquisition times as compared to current x-ray imaging modalities, future studies are needed to investigate high intensity micro focus x-ray tubes, such as a liquid metal jet x-ray tube and/or a high intensity nanotubes array.

In addition, the imaging prototype presented in this dissertation is operated under high-energy x-rays, and the prime beam spectrum has been optimized by removing a large percentage of the low-energy photons to ensure that the interaction between the high-energy x-ray photons and the soft tissues is dominated by Compton scattering. In this case, other types of interactions such as photoelectric absorption and Rayleigh scattering can be ignored. Since Compton scattering between high-energy x-ray photons and soft tissues is determined by the electron density of the tissue materials, which is relatively identical, this high-energy in-line phase contrast based imaging method can be further translated into a 3D quantitative imaging technique to perform biometric identification when the phase retrieval method is performed.

To further introduce energy-differentiated phase contrast imaging methods, dual-energy in-line phase contrast performed with a photon-counting detector can be proposed in the future. The ability of this imaging technique has been demonstrated to provide two or more energy-differentiated images simultaneously in conventional x-ray imaging by

setting energy threshold values. Therefore, introducing the photon-counting technique into the phase contrast tomosynthesis prototype presented in this dissertation has the potential to further improve x-ray imaging efficiency, solve and/or eliminate the x-ray energy related technical defects, and benefit the applications of phase retrieved images acquired under different x-ray energy intervals.

In addition, more biology-related studies are needed to focus the high-energy in-line phase contrast tomosynthesis technique on clinical breast imaging and chest imaging. In the future, studies toward the applications of the technique developed in this dissertation can be extended to imaging other types of organs/tissues with more complicated structures, such as liver, pancreas, kidney, etc.

For the application of microbubbles as phase contrast agents, the studies presented in this dissertation have elucidated extensive capabilities for future studies. The comparison studies have illustrated the ability of high-energy in-line phase contrast approaches to enhance the detectability, thus it motivates research toward radiation dose reduction in the future. Since the microbubble is comprised of low-Z element materials, its differentiability by interacting with low-energy and high-energy x-ray photons may have the potential to improve image quality by employing a dual-energy or multi-energy in-line phase contrast technique in the future. In addition, the potential of microbubbles to provide a clearer boundary between normal tissues and tumors motivates future studies toward investigating the use of microbubble 3D imaging methods to benefit computer aided diagnosis techniques. As with the imaging prototype itself, more biology-related

studies on the microbubbles as x-ray phase contrast agents are needed in the future to facilitate the translation of this imaging method into clinical applications.

Bibliography

[1] Siegel RL, Miller KD, Jemal A. Cancer statistics, 2016. CA: a cancer journal for clinicians. 2016 Jan 1;66(1):7-30.

[2] Karellas A, Vedantham S. Breast cancer imaging: a perspective for the next decade. Medical physics. 2008 Nov 1;35(11):4878-97.

[3] Gold RH. The evolution of mammography. Radiologic Clinics of North America. 1992 Jan;30(1):1-9.

[4] Bushberg JT, Boone JM. The essential physics of medical imaging. Lippincott Williams & Wilkins; 2011 Dec 20.

[5] Gennaro G, Hendrick RE, Ruppel P, Chersevani R, Di Maggio C, La Grassa M, Pescarini L, Polico I, Proietti A, Baldan E, Bezzon E. Performance comparison of single-view digital breast tomosynthesis plus single-view digital mammography with two-view digital mammography. European radiology. 2013 Mar 1;23(3):664-72.

[6] Gennaro G, Toledano A, Di Maggio C, Baldan E, Bezzon E, La Grassa M, Pescarini L, Polico I, Proietti A, Toffoli A, Muzzio PC. Digital breast tomosynthesis versus digital mammography: a clinical performance study. European radiology. 2010 Jul 1;20(7):1545-53.

[7] Haas BM, Kalra V, Geisel J, Raghu M, Durand M, Philpotts LE. Comparison of tomosynthesis plus digital mammography and digital mammography alone for breast cancer screening. Radiology. 2013 Dec;269(3):694-700.

[8] Sechopoulos I. A review of breast tomosynthesis. Part I. The image acquisition process. Medical physics. 2013 Jan 1;40(1):014301.

[9] Yaffe MJ, Mainprize JG. Digital tomosynthesis: technique. Radiologic Clinics of North America. 2014 May 31;52(3):489-97.

[10] Castelli E, Tonutti M, Arfelli F, Longo R, Quaia E, Rigon L, Sanabor D, Zanconati F, Dreossi D, Abrami A, Quai E. Mammography with synchrotron radiation: first clinical experience with phase-detection technique. Radiology. 2011 Jun;259(3):684-94.

[11] Tanaka J, Nagashima M, Kido K, Hoshino Y, Kiyohara J, Makifuchi C, Nishino S, Nagatsuka S, Momose A. Cadaveric and in vivo human joint imaging based on differential phase contrast by X-ray Talbot-Lau interferometry. Zeitschrift für Medizinische Physik. 2013 Sep 30;23(3):222-7.

[12] Zanette I, Zhou T, Burvall A, Lundström U, Larsson DH, Zdora M, Thibault P, Pfeiffer F, Hertz HM. Speckle-based x-ray phase-contrast and dark-field imaging with a laboratory source. Physical review letters. 2014 Jun 26;112(25):253903.

[13] Wu X, Yan A. Phase retrieval from one single phase contrast x-ray image. Optics express. 2009 Jun 22;17(13):11187-96.

[14] Liu H, Zhang D, Wu X. Development of a dual detector phase x-ray imaging system: design considerations. InImage Analysis and Interpretation, 2008. SSIAI 2008. IEEE Southwest Symposium on 2008 Mar 24 (pp. 193-196). IEEE.

[15] Liu H, Ren Y, Guo H, Xue Y, Xie H, Xiao T, Wu X. Phase retrieval for hard X-ray computed tomography of samples with hybrid compositions. Chinese Optics Letters. 2012 Dec 1;10(12):121101-.

[16] Hammonds JC, Price RR, Donnelly EF, Pickens DR. Phase-contrast digital tomosynthesis. Medical physics. 2011 May 1;38(5):2353-8.

[17] Huang ZF, Kang KJ, Zhang L, Chen ZQ, Ding F, Wang ZT, Fang QG. Differential phase-contrast imaging experimental system under the incoherent condition with conventional x-ray tubes. Nuclear Science, IEEE Transactions on. 2009 Jun;56(3):1438-43.

[18] Hammonds JC, Price RR, Pickens DR, Donnelly EF. In-line phase shift tomosynthesis. Medical physics. 2013 Aug 1;40(8):081911.

[19] Stutman D, Beck TJ, Carrino JA, Bingham CO. Talbot phase-contrast x-ray imaging for the small joints of the hand. Physics in medicine and biology. 2011 Aug 12;56(17):5697.

[20] Blonder B, Carlo F, Moore J, Rivers M, Enquist BJ. X-ray imaging of leaf venation networks. New Phytologist. 2012 Dec 1;196(4):1274-82.

[21] Wong MD, Yan A, Ghani M, Li Y, Fajardo L, Wu X, Liu H. Dose and detectability improvements with high energy phase sensitive x-ray imaging in comparison to low energy conventional imaging. Physics in medicine and biology. 2014 Apr 15;59(9):N37.

[22] Arfelli F, Rigon L, Menk RH. Microbubbles as x-ray scattering contrast agents using analyzer-based imaging. Physics in medicine and biology. 2010 Feb 24;55(6):1643.

[23] Xi Y, Tang R, Wang Y, Zhao J. Microbubbles as contrast agent for in-line x-ray phase-contrast imaging. Applied Physics Letters. 2011 Jul 4;99(1):011101.

[24] Tang R, Xi Y, Chai WM, Wang Y, Guan Y, Yang GY, Xie H, Chen KM. Microbubble-based synchrotron radiation phase contrast imaging: basic study and

angiography applications. Physics in medicine and biology. 2011 May 23;56(12):3503.

[25] Millard TP, Endrizzi M, Rigon L, Arfelli F, Menk RH, Owen J, Stride E, Olivo A. Quantification of microbubble concentration through x-ray phase contrast imaging. Applied Physics Letters. 2013 Sep 9;103(11):114105.

[26] Velroyen A, Bech M, Malecki A, Tapfer A, Yaroshenko A, Ingrisch M, Cyran CC, Auweter SD, Nikolaou K, Reiser M, Pfeiffer F. Microbubbles as a scattering contrast agent for grating-based x-ray dark-field imaging. Physics in medicine and biology. 2013 Feb 1;58(4):N37.

[27] Malecki A, Potdevin G, Pfeiffer F. Quantitative wave-optical numerical analysis of the dark-field signal in grating-based x-ray interferometry. EPL (Europhysics Letters). 2012 Aug 17;99(4):48001.

[28] Millard TP, Endrizzi M, Everdell N, Rigon L, Arfelli F, Menk RH, Stride E, Olivo A. Evaluation of microbubble contrast agents for dynamic imaging with x-ray phase contrast. Scientific reports. 2015 Jul 29;5.

[29] Tang X, Yang Y. X-ray differential phase contrast and dark-field computed tomography and radiography with microbubbles as contrast agent. InBiomedical Imaging (ISBI), 2013 IEEE 10th International Symposium on 2013 Apr 7 (pp. 1248-1251). IEEE.

[30] Niklason LT, Christian BT, Niklason LE, Kopans DB, Castleberry DE, Opsahl-Ong BH, Landberg CE, Slanetz PJ, Giardino AA, Moore R, Albagli D. Digital tomosynthesis in breast imaging. Radiology. 1997 Nov;205(2):399-406.

[31] Cheung LK, Jing Z, Bogdanovich S, Golden K, Robinson S, Beliaevskaia E, Parikh S. Image performance of a new amorphous selenium flat panel x-ray detector designed for digital breast tomosynthesis. InMedical Imaging 2005 Apr 20 (pp. 1282-1290). International Society for Optics and Photonics.

[32] Ren B, Ruth C, Wu T, Zhang Y, Smith A, Niklason L, Williams C, Ingal E, Polischuk B, Jing Z. A new generation FFDM/tomosynthesis fusion system with selenium detector. InSPIE Medical Imaging 2010 Mar 4 (pp. 76220B-76220B). International Society for Optics and Photonics.

[33] See GEHC-Brochure: Mammography SenoClaire 3D Breast Tomosynthesis

[34] Naday S, Bullard EF, Gunn S, Brodrick JE, O'Tuairisg EO, McArthur A, Amin H, Williams MB, Judy PG, Konstantinidis A. Optimised breast tomosynthesis with a novel CMOS flat panel detector. InDigital Mammography 2010 Jun 16 (pp. 428-435). Springer Berlin Heidelberg.

[35] Patel T, Klanian K, Gong Z, Williams MB. Detective quantum efficiency of a CsI-CMOS x-ray detector for breast tomosynthesis operating in high dynamic range and high sensitivity modes. InBreast Imaging 2012 Jul 8 (pp. 80-87). Springer Berlin Heidelberg.

[36] Sprenger F, Calderon-Colon X, Cheng Y, Englestad K, Lu J, Maltz J, Paidi A, Qian X, Spronk D, Sultana S, Yang G. Distributed source x-ray tube technology for tomosynthesis imaging. InSPIE Medical Imaging 2010 Mar 4 (pp. 76225M-76225M). International Society for Optics and Photonics.

[37] Sprenger F, Calderon X, Gidcumb E, Lu J, Qian X, Spronk D, Tucker A, Yang G, Zhou O. Stationary digital breast tomosynthesis with distributed field emission x-

ray tube. InSPIE Medical Imaging 2011 Mar 3 (pp. 79615I-79615I). International Society for Optics and Photonics.

[38] Tucker A, Qian X, Gidcumb E, Spronk D, Sprenger F, Kuo J, Ng S, Lu J, Zhou O. Optimizing configuration parameters of a stationary digital breast tomosynthesis system based on carbon nanotube x-ray sources. InSPIE Medical Imaging 2012 Feb 23 (pp. 831307-831307). International Society for Optics and Photonics.

[39] Qian X, Tucker A, Gidcumb E, Shan J, Yang G, Calderon-Colon X, Sultana S, Lu J, Zhou O, Spronk D, Sprenger F. High resolution stationary digital breast tomosynthesis using distributed carbon nanotube x-ray source array. Medical physics. 2012 Apr 1;39(4):2090-9.

[40] Tucker AW, Lee YZ, Kuzmiak CM, Calliste J, Lu J, Zhou O. Increased microcalcification visibility in lumpectomy specimens using a stationary digital breast tomosynthesis system. InSPIE Medical Imaging 2014 Mar 19 (pp. 903316-903316). International Society for Optics and Photonics.

[41] Tucker AW, Lu J, Zhou O. Dependency of image quality on system configuration parameters in a stationary digital breast tomosynthesis system. Medical physics. 2013 Mar 1;40(3):031917.

[42] Shan J, Tucker AW, Lee YZ, Heath MD, Wang X, Foos DH, Lu J, Zhou O. Stationary chest tomosynthesis using a carbon nanotube x-ray source array: a feasibility study. Physics in medicine and biology. 2014 Dec 5;60(1):81.

[43] Schmitzberger FF, Fallenberg EM, Lawaczeck R, Hemmendorff M, Moa E, Danielsson M, Bick U, Diekmann S, Pöllinger A, Engelken FJ, Diekmann F.

Development of low-dose photon-counting contrast-enhanced tomosynthesis with spectral imaging. Radiology. 2011 May;259(2):558-64.

[44] Dahlman N, Fredenberg E, Åslund M, Lundqvist M, Diekmann F, Danielsson M. Evaluation of photon-counting spectral breast tomosynthesis. InSPIE Medical Imaging 2011 Mar 3 (pp. 796114-796114). International Society for Optics and Photonics.

[45] Wallis MG, Moa E, Zanca F, Leifland K, Danielsson M. Two-view and single-view tomosynthesis versus full-field digital mammography: high-resolution X-ray imaging observer study. Radiology. 2012 Mar;262(3):788-96.

[46] Xu J, Zbijewski W, Gang G, Stayman JW, Taguchi K, Lundqvist M, Fredenberg E, Carrino JA, Siewerdsen JH. Cascaded systems analysis of photon counting detectors. Medical physics. 2014 Oct 1;41(10):101907.

[47] Haerer W, Lauritsch G, Zellerhoff M, inventors; Siemens Aktiengesellschaft, assignee. Method for reconstructing a three-dimensional image of an object scanned in the context of a tomosynthesis, and apparatus for tomosynthesis. United States patent US 6,442,288. 2002 Aug 27

[48] Mertelmeier T, Orman J, Haerer W, Dudam MK. Optimizing filtered backprojection reconstruction for a breast tomosynthesis prototype device. InMedical Imaging 2006 Mar 2 (pp. 61420F-61420F). International Society for Optics and Photonics.

[49] Baker JA, Lo JY. Breast tomosynthesis: state-of-the-art and review of the literature. Academic radiology. 2011 Oct 31;18(10):1298-310.

[50] Fitzgerald R. Phase-sensitive x-ray imaging. Phys. Today. 2000 Jul 1;53(7):23-6.

[51] Takeda T, Momose A, Hirano K, Haraoka S, Watanabe T, Itai Y. Human Carcinoma: Early Experience with Phase-Contrast X-ray CT with Synchrotron Radiation—Comparative Specimen Study with Optical Microscopy 1. Radiology. 2000 Jan;214(1):298-301.

[52] Kiss MZ, Sayers DE, Zhong Z. Measurement of image contrast using diffraction enhanced imaging. Physics in medicine and biology. 2003 Jan 16;48(3):325.

[53] Wu X, Liu H. Clinical implementation of x-ray phase-contrast imaging: Theoretical foundations and design considerations. Medical physics. 2003 Aug 1;30(8):2169-79.

[54] Pogany A, Gao D, Wilkins SW. Contrast and resolution in imaging with a microfocus x-ray source. Review of Scientific Instruments. 1997 Jul 1;68(7):2774-82.

[55] Donnelly EF, Price RR, Pickens DR. Quantification of the effect of system and object parameters on edge enhancement in phase-contrast radiography. Medical physics. 2003 Nov 1;30(11):2888-96.

[56] Wu X, Liu H, Yan A. System design considerations for an x-ray phase-contrast imaging system based on in-line holography. InPhotonics Asia 2004 2005 Jan 18 (pp. 130-140). International Society for Optics and Photonics.

[57] Wu X, Liu H. A general theoretical formalism for X-ray phase contrast imaging. Journal of X-ray Science and Technology. 2003 Jan 1;11(1):33-42.

[58] Wu X, Liu H, Yan A. X-ray phase-attenuation duality and phase retrieval. Optics letters. 2005 Feb 15;30(4):379-81.

[59] Zhang L, Jin M, Huang Z, Xiao Y, Yin H, Wang Z, Xiao T. Phase-contrast tomosynthetic experiment on biological samples with synchrotron radiation. InNuclear Science Symposium Conference Record (NSS/MIC), 2010 IEEE 2010 Oct 30 (pp. 1619-1621). IEEE.

[60] Helfen L, Baumbach T, Cloetens P, Baruchel J. Phase-contrast and holographic computed laminography. Applied Physics Letters. 2009 Mar 9;94(10):104103.

[61] Wu X, Liu H. An experimental method of determining relative phase-contrast factor for x-ray imaging systems. Medical physics. 2004 May 1;31(5):997-1002.

[62] Feldkamp LA, Davis LC, Kress JW. Practical cone-beam algorithm. JOSA A. 1984 Jun 1;1(6):612-9.

[63] Rougee A, Picard CL, Trousset YL, Ponchut C. Geometrical calibration for 3D x-ray imaging. InMedical Imaging 1993 1993 Jun 30 (pp. 161-169). International Society for Optics and Photonics.

[64] Godfrey DJ, Yin FF, Oldham M, Yoo S, Willett C. Digital tomosynthesis with an on-board kilovoltage imaging device. International Journal of Radiation Oncology* Biology* Physics. 2006 May 1;65(1):8-15.

[65] Chen Z, Calhoun VD, Chang S. Compensating the intensity fall-off effect in cone-beam tomography by an empirical weight formula. Applied optics. 2008 Nov 10;47(32):6033-9.

[66] Yan A, Wu X, Liu H. Performance analysis of the attenuation-partition based iterative phase retrieval algorithm for in-line phase-contrast imaging. Optics express. 2010 Jul 19;18(15):16074-89.

[67] Zhang D, Rong J, Chu R, Chen WR, Liu H. DQE measurements in magnification X-ray imaging. Journal of X-Ray Science and Technology. 2006 Jan 1;14(2):141-50.

[68] Wells JR, Dobbins III JT. Estimation of the two-dimensional presampled modulation transfer function of digital radiography devices using one-dimensional test objects. Medical physics. 2012 Oct 1;39(10):6148-60.

[69] Donovan M, Zhang D, Liu H. Step by step analysis toward optimal MTF algorithm using an edge test device. Journal of X-ray science and technology. 2009 Jan 1;17(1):1-5.

[70] Siewerdsen JH, Cunningham IA, Jaffray DA. A framework for noise-power spectrum analysis of multidimensional images. Medical physics. 2002 Nov 1;29(11):2655-71.

[71] Zhao B, Zhou J, Hu YH, Mertelmeier T, Ludwig J, Zhao W. Experimental validation of a three-dimensional linear system model for breast tomosynthesis. Medical physics. 2009 Jan 1;36(1):240-51.

[72] Wong M, Wu X, Liu H. Preliminary investigation on the effect of x-ray beam hardening on detective quantum efficiency and radiation dose. InImage Analysis & Interpretation (SSIAI), 2010 IEEE Southwest Symposium on 2010 May 23 (pp. 17-20). IEEE.

[73] Zhang D, Donovan M, Fajardo LL, Archer A, Wu X, Liu H. Preliminary feasibility study of an in-line phase contrast x-ray imaging prototype. Biomedical Engineering, IEEE Transactions on. 2008 Sep;55(9):2249-57.

[74] Zhao B, Zhao W. Imaging performance of an amorphous selenium digital mammography detector in a breast tomosynthesis system. Medical physics. 2008 May 1;35(5):1978-87.

[75] Mainprize JG, Bloomquist AK, Kempston MP, Yaffe MJ. Resolution at oblique incidence angles of a flat panel imager for breast tomosynthesis. Medical physics. 2006 Sep 1;33(9):3159-64.

[76] Wang X, Mainprize JG, Wu G, Yaffe MJ. Task-based evaluation of image quality of filtered back projection for breast tomosynthesis. InDigital Mammography 2010 Jun 16 (pp. 106-113). Springer Berlin Heidelberg.

[77] Marshall N, Jacobs J, Cockmartin L, Bosmans H. Technical evaluation of a digital breast tomosynthesis system. InDigital Mammography 2010 Jun 16 (pp. 350-356). Springer Berlin Heidelberg.

[78] Ludwig J, Mertelmeier T, Kunze H, Härer W. A novel approach for filtered backprojection in tomosynthesis based on filter kernels determined by iterative reconstruction techniques. InDigital Mammography 2008 Jul 20 (pp. 612-620). Springer Berlin Heidelberg.

[79] Hubbell JH, Seltzer SM. Tables of X-ray mass attenuation coefficients and mass energy-absorption coefficients (version 1.4). National Institute of Standards and Technology, Gaithersburg, MD. 2004 Sep 16.

[80] Vidal RM, do Nascimento Souza D. A model for the characterization and selection of beeswaxes for use as base substitute tissue in photon teletherapy. Materials Sciences and Applications. 2012 Apr 18;3(04):218.

[81] Mery D, Lillo I, Loebel H, Riffo V, Soto A, Cipriano A, Aguilera JM. Automated fish bone detection using X-ray imaging. Journal of Food Engineering. 2011 Aug 31;105(3):485-92.

[82] Doyle P, Martin CJ, Gentle D. Application of contrast-to-noise ratio in optimizing beam quality for digital chest radiography: comparison of experimental measurements and theoretical simulations. Physics in medicine and biology. 2006 May 24;51(11):2953.

[83] Wu X, Liu H, Yan A. Robustness of a phase-retrieval approach based on phase-attenuation duality. Journal of X-Ray Science and Technology. 2007 Jan 1;15(2):85-95.

[84] Marshall NW. Detective quantum efficiency measured as a function of energy for two full-field digital mammography systems. Physics in medicine and biology. 2009 Apr 21;54(9):2845.

[85] Hendrick R E et al 1994 Mammography Quality ControlManuals (Radiologist, Radiologic Technologist, Medical Physicist) (Reston, VA: American College of Radiology)

[86] Wu X. Breast dosimetry in screen-film mammography. Screen Film Mammography: Imaging Considerations and Medical Physics Responsibilities. 1991:159-75.

[87] Wu X, Barnes GT, Tucker DM. Spectral dependence of glandular tissue dose in screen-film mammography. Radiology. 1991 Apr;179(1):143-8.

[88] Wu X, Gingold EL, Barnes GT, Tucker DM. Normalized average glandular dose in molybdenum target-rhodium filter and rhodium target-rhodium filter mammography. Radiology. 1994 Oct;193(1):83-9.

[89] Wu D, Wong MD, Li Y, Chen WR, Wu X, Liu H. DQE characterization of a high-energy in-line phase contrast prototype under different kVp and beam filtration. InSPIE BiOS 2015 Mar 9 (pp. 932418-932418). International Society for Optics and Photonics.

[90] Wu D, Yan A, Li Y, Wong MD, Zheng B, Wu X, Liu H. Characterization of a high-energy in-line phase contrast tomosynthesis prototype. Medical physics. 2015 May 1;42(5):2404-20.

[91] Wu D, Ghani MU, Wong MD, Li Y, Yang K, Chen WR, Zheng B, Liu H. Quantitative imaging of the microbubble concentrations by using an in-line phase contrast tomosynthesis prototype: a preliminary phantom study. InSPIE Medical Imaging 2016 Mar 30 (pp. 97835L-97835L). International Society for Optics and Photonics.

[92] Srinivasarao M, Galliford CV, Low PS. Principles in the design of ligand-targeted cancer therapeutics and imaging agents. Nature Reviews Drug Discovery. 2015 Mar 1;14(3):203-19.

[93] Steinl DC, Kaufmann BA. Ultrasound imaging for risk assessment in atherosclerosis. International journal of molecular sciences. 2015 Apr 29;16(5):9749-69.

[94] Lindner JR. Molecular imaging of vascular phenotype in cardiovascular disease: new diagnostic opportunities on the horizon. Journal of the American Society of Echocardiography. 2010 Apr 30;23(4):343-50.